Electromechanical Manipulation of Transition Metal Dichalcogenides for Quantum Information Applications

Adina Ripin

A dissertation
submitted in partial fulfillment of the
requirements for the degree of

Doctor of Philosophy

University of Washington

2025

Reading Committee:

Mo Li, Chair

Xiaodong Xu

Ting Cao

Program Authorized to Offer Degree:
Physics

University of Washington

Abstract

Electromechanical Manipulation of Transition Metal Dichalcogenides for Quantum Information Applications

Adina Ripin

Chair of the Supervisory Committee:
Mo Li
Department of Physics, Department of Electrical and Computer Engineering

Two-dimensional semiconductors, particularly transition metal dichalcogenides (TMDs), have garnered significant attention in recent years due to their strong light–matter interactions and unique quantum properties, making them promising candidates for quantum information science. These properties are highly tunable using external electric and strain fields. In this thesis, we explore both static and dynamic approaches to tuning TMDs with these fields to develop quantum information devices.

In Chapter 1, we introduce the fundamental properties of TMDs and the mechanisms by which electric and strain fields modulate their behavior. We also review prior work in this area and lay the groundwork for our experiments by introducing surface acoustic waves (SAWs) as a method for dynamic field control.

Chapter 2 presents our work demonstrating long-range, directional transport of interlayer excitons in bilayer WSe_2 using SAWs. The excitons' intrinsic out-of-plane dipole moment allows them to be trapped in the dynamic potential wells created by the SAW electric field and carried along the propagation direction. We examine this transport across varying SAW powers and temperatures, and introduce an ITO capping layer that suppresses in-plane electric fields to prevent exciton dissociation.

In Chapter 3, we investigate quantum emitters in bilayer WSe_2 and demonstrate

energy tunability via out-of-plane electric fields applied through graphite gates, addressing the challenge of inhomogeneous emission energies. We also report the discovery of phonon sidebands arising from coupling between individual excitons and localized interlayer breathing mode phonons. We quantify this exciton–phonon coupling and explore its tunability with electric field, highlighting opportunities for encoding our quantum emitters with fundamental information from the 2D phonon modes.

Chapter 4 details our ongoing work using SAW resonators to dynamically manipulate excitonic states in bilayer WSe_2. This platform enables spatial modulation of excitonic properties through standing SAW fields and time-averaged tuning of exciton energies and linewidths. We also investigate the possibility of exciton trapping at SAW anti-nodes and discuss its potential for enhancing exciton–exciton interactions, which could open a path toward excitonic quantum simulations.

Finally, in Chapter 5, we synthesize the key results of each project, reflect on their implications, and outline future research directions that build on the integration of dynamic and static control in 2D material systems for scalable quantum technologies.

TABLE OF CONTENTS

LIST OF FIGURES

LIST OF TABLES

ABBREVIATIONS

SAW: Surface acoustic wave

IDT: Interdigital transducer

TMD: Transition metal dichalcogenide

SPE: Single photon emitter

QE: Quantum emitter

VNA: Vector network analyzer

PL: Photoluminescence

IX: Interlayer exciton

EBL: Electron-beam lithography

RT: Room temperature

DFT: Density functional theory

FWHM: Full-width half-maximum

QE: Quantum emitter

PES: Potential energy surface

BM: Breathing mode

RMSE: Root-mean-square error

SPADs: Single-photon avalanche photodetectors

TCSPC: Time-correlated single-photon counter

FTD: Finite time domain

AFM: Atomic force microscopy

VARIABLES

S11, S22, S21, S12: Components of the two port reflection matrix S

λ: Wavelength

f: Frequency

f_0: Design frequency of the SAW

ω: Angular frequency, $= 2\pi f$

k: Wavenumber, $= 2\pi/\lambda$

v_{SAW}: Velocity of the SAW

ϵ: Dielectric constant

K^2: Piezoelectric coupling coefficient

P_{SAW}, P_s: Acoustic power

P_P: Optical pump power

A: Cross-sectional area

ϕ: SAW amplitude

C: Capacitance

Y: Admittance

R: Resistance

L_p: Distance the SAW propagates into the reflector array

d: Distance between reflector arrays

L_c: Total cavity length, $= 2L_p + d$

Q_u: Unloaded (internal) quality factor

Q_l: Loaded (external) quality factor

j: Diffusive IX flux density

D: Temperature-dependent diffusion coefficient

$g^2(0)$: Second-order correlation measurement

V: Voltage

S: Dimensionless Huang-Rhys parameter

g_0: Single-phonon-IX coupling rate

$\overline{x}_{zpf}$: Zero-point amplitude of the Γ-point breathing mode

g^0: Zero-field coupling rate

γ_e: Exciton linewidth

γ_p: Breathing mode phonon decoherence rate

$A(t)$: Amplitude of the SAW wave relative to initial amplitude

τ_d: Exponential decay time of the stored energy

ACKNOWLEDGMENTS

I have learned so much in my time doing this Ph.D. study, and all of that is due to the incredible people who have taken the time to teach me. First and foremost, I would like to thank my advisor, Professor Mo Li. Mo is the best advisor I could possibly have asked for. He is patient but endlessly curious, and has taught me so much about ways to approach different research problems. He is encouraging, but also constantly challenges my ideas and assumptions in ways that have allowed me to grow and develop my own confidence and perspective. I have learned so much in his group and from the opportunities he has given me, from mentoring REU students to traveling to conferences. His passion for his research inspires me to be a better scientist.

So much of my learning has come from the people around me in Mo Li's group, and I would like to express my gratitude to all of the current and former members who have taught me so much. Dr. Ruoming Peng taught me the ropes when I first joined the group and helped me develop my base of knowledge, and Dr. Seokyheong Lee was always willing to help troubleshoot any problem, no matter how small. I need to express a special thanks to Dr. I-Tung Chen, who began around the same time as me and always was there to cheer me up with a laugh. I have learned so much from his dedication and kindness, and I couldn't have completed my Ph.D. without him. Ameya Velankar, Hannah Boyer, and Grace Pardini all have worked closely with me on many of these projects, and I thank them so much for their help and patience over the years. I would also like to thank Dr. Changming Wu, Dr. Bingzhao Li, Qixuan Lin, Haoqin Deng, Shucheng Fang, Yue Yu, and Mark Han.

I would like to thank my reading committee members, Ting Cao and Xiaodong Xu who are some of the foremost experts in their field, and yet still always find time to help and advise me, as well as my other supervisory committee members, David Masiello, Serena Eley, and Steve Sharpe, who are always willing to take time out of their busy schedules.

The work in this thesis is made possible by the wonderful facilities at the University of Washington, including MEM-C and WNF. I would like to thank all of the wonderful people who work there, as well as acknowledge funding from MEM-C, the UPWARDS program, and the NSF-GRFP. The biggest thing I have appreciated about my time here at UW is the collaborative spirit between different groups, and it has been a pleasure collaborating with all of the graduate students and postdocs who I have worked with during my time here, including MEM-C members Xiaowei Zhang, Srivatsa Chakravarthi, Minhao He, Jordan Fonseca, John Cenker, Will Holtzmann, Jack Barlow, Paul Nguyen, Eric Lester, and Ellis Thompson, as well as fellow UPWARDS fellows Mai Nguyen, Yueyao Fan, and Jane Keth.

I feel incredibly lucky to have the support of some amazing friends who have helped me throughout the years: Eliza Owen-Smith, Lou Lief, Nic Rothbacher, Sarah Walling-Bell, CJ Nave, Samantha Tetef, Niall Ridgley, and so many more. I would also like to thank the Seattle Mariners, and particularly Cal Raleigh, for years of entertainment and always getting a win when I needed it the most.

I would like to thank my family for a lifetime of support– my sister, Tillie, my parents, Trudy and Dave, and my grandparents, Marilyn, Barrie, Susan, and Ken. I would not be here today without all of their love and support. Finally, I would like to thank my partner, Jeremy Hartse, for all of his support, encouragement, and love.

DEDICATION

To my parents, Trudy and Dave, and my partner, Jeremy.

Chapter 1
INTRODUCTION

1.1 Two-dimensional excitonic materials

Two-dimensional materials are materials that are between a single atom to a few nanometers thick. The study of atomically thin materials took off after 2004, when Geim and Novoselov discovered graphene. This material consists of a single layer of carbon atoms, known as a monolayer, which they obtained by exfoliating a bulk crystal of graphite using scotch tape. For this work, they were awarded the Nobel Prize in Physics in 2010 [1]. Rapidly, scientists began studying graphene as well as many other materials that could be exfoliated down to the monolayer, developing techniques for stacking different thin layers of materials together with precise control. These 2D heterostructures are held together via van der Waals forces and allow scientists to study the unique physics that occurs in these ultra-confined systems [2].

1.1.1 Particles and quasiparticles in two dimensions

The study of graphene and other 2D materials made it clear that many concepts of solid-state physics needed to be adapted when considering 2D systems rather than traditional 3D crystals. The reduced dimensionality impacts the properties and behavior of virtually every particle and quasi-particle in the 2D system, including electrons, excitons, plasmons, phonons, magnons, skyrmions, and many more. An illustrative example is considering electron-electron interactions.

Consider two electrons in a vacuum. These two particles will interact via the Coulomb potential $V \propto e^2/r$, where e is the charge of an electron and r is the distance between them. This potential is a 3D field between the two particles that

repels them. This picture becomes more complicated when we consider many electrons confined to a 3D crystal lattice. In this confined space, the surrounding electrons move freely to shield the electric field, thus minimizing the electron-electron interaction by $e^{-r/l}/r$ where l is the screening length that depends on the density of electrons in the material [3, 4]. The behavior of this system can be interpreted as a quasiparticle, where an individual electron is dressed by a cloud of other electrons with overlapping wavefunctions. Therefore, electron-electron interactions are governed by weaker short-range forces that allow the electrons to effectively ignore each other [5].

In a 2D material, the electric field from the electrons still exists in three dimensions. However, the electrons themselves are not able to move along the z axis because they are strictly confined by the potential from the lattice ions, and therefore are unable to effectively screen the electric field that arises [3]. This tells us that 2D materials are inherently much more strongly correlated than their bulk counterparts.

These effects are even more extreme in 2D semiconductors. In bulk semiconductors critical for modern technology, quasiparticles called excitons are formed when an electron in the conduction band and a hole in the valence band bind together. When the excitons recombine, they emit a photon corresponding to the binding energy of the exciton. Excitons can be observed by detecting these emitted photons, called the photoluminescence (PL) spectrum.

In bulk semiconductors, these excitons are easily modeled as a hydrogen atom and considering the states close to the band edges is sufficient to predict exciton behavior [3]. In 2D, however, the lack of electron screening and resulting strong interactions yield a much more complex excitonic landscape, requiring the consideration of the entire band structure. This effect gives rise to many species of excitons, as well as bi-excitons, which are two excitons bound together, and trions, which are two electrons bound to a single hole.

Another key difference that arises in 2D materials is that collective states require much less energy to create compared to their bulk counterparts. For phonon modes, or

collective lattice vibrations in a bulk crystal, an atom is confined in three dimensions by its lattice neighbors. In two dimensions, the atom becomes free to move along the z axis, creating new phonon modes that are not seen in the bulk. Additionally, because phonon modes now require only excitation within a single layer of atoms rather than many layers, existing modes become significantly easier to excite [5].

1.1.2 2D materials for quantum information applications

These unique properties of 2D materials make them an interesting platform for quantum information science. For example, quantum dots in bulk materials require the creation of a 2D electron gas (2DEG) via gating to tightly confine electrons, whose spin is used as the degree of quantum information. 2D semiconductors eliminate the need for gating to confine the electrons to a 2D plane, although they still require gates to restrict the electron movement to a single point within the 2D material [6].

In bulk materials, atomic defects such as NV centers in diamond are promising for quantum information because the atomic transitions are very sharply defined, leading to the emission of nearly identical single photons. These identical single photons are a key requirement for photonic quantum computing. However, these atomic defects are often deep within a material, making it difficult to couple the photons in and out. 2D material-based single photon emitters (SPEs) bypass this difficulty. SPEs in 2D materials are created from defect-bound excitons or deep in-gap states created by external forces, and are of particular interest because of the potential to encode valley or spin information from the material into the single photon [6, 7].

2D materials also have unique topological properties that are very interesting for quantum information applications. In three dimensions, particles are either bosons or fermions. In two dimensions, there are also particles called anyons, which enable topologically protected quantum states that could be used for fault-tolerant quantum computing. The unique topological features of 2D materials are a quickly growing area of research, and recent breakthroughs, including the observation of the fractional

quantum anomalous Hall effect [6, 8].

1.2 Transition metal dichalcogenides

While graphene was the first widely studied 2D material, the lack of an electronic bandgap led to a search for 2D semiconductors. This led to the discovery of transition metal dichalcogenides (TMDs), which have an atomic composition of MX_2, where M is a transition metal atom such as molybdenum (Mo) or tungsten (W) and X is a chalcogen atom such as sulfur (S), selenium (Se), or tellurium (Te) [9]. 2D materials in this class are semiconductors with a direct bandgap, have strong mechanical flexibility, and are electrically tunable, all of which make them interesting for studies of fundamental physics as well as device integration.

1.2.1 Structure of transition metal dichalcogenides

TMDs have a hexagonal lattice and are typically either in a trigonal prismatic (2H) or an octahedral (1T) structural phase corresponding to the stacking order of the chalcogen-metal-chalcogen layers, as seen in the profile view of Fig. 1.1a [9].

The electronic properties of a crystal are determined by the electronic band structure, where local minima in the conduction band or local maxima in the valence band are known as valleys. Electrons in a crystal then have charge, spin, and valley as degrees of information. In hexagonal lattices, like those found in transition metal dichalcogenides (TMDs), the two valleys are found at the two inequivalent K and -K points corresponding to the corners of the hexagonal Brillouin zone, shown in Fig. 1.1a [9]. These valleys can be assigned a pseudospin that can take on the value of valley-pseudospin up, corresponding to electrons originating from the +K valley, or valley-pseudospin down, corresponding to electrons originating from the -K valley.

We can also see from Fig. 1.1a that monolayer TMDs lack inversion symmetry. In this case, time reversal symmetry dictates that the spin degeneracy at the valence band and conduction band is lifted, leading to opposite spin splitting driven by the

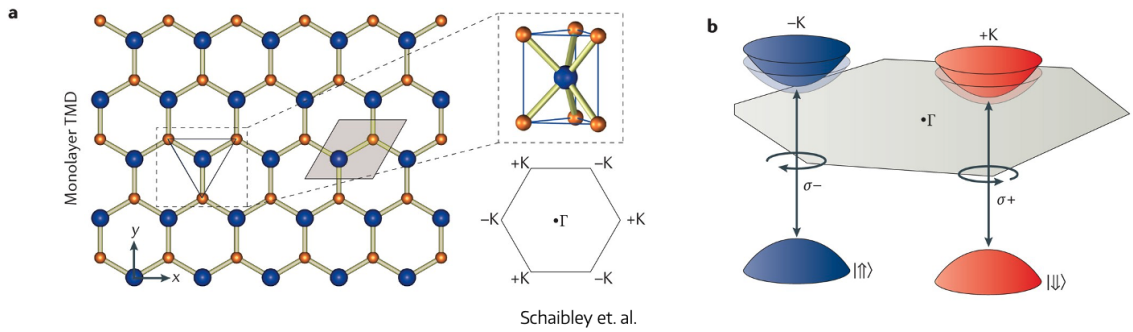

Figure 1.1: Valley dependent carrier transport. a) The 2D hexagonal crystal structure of a monolayer transition metal dichalcogenide (TMD) composed of transition metal atoms (blue) and chalcogen atoms (orange) resembles that of graphene but with broken inversion symmetry. A side view shows the 3D structure. The hexagonal Brillouin zone is shown labeling the Γ point and the two inequivalent +K and -K points. b) Valley dependent optical selection rules for interband transitions in monolayer TMDs. $\sigma+$ polarized light couples to the +K (red) valley, and $\sigma-$ polarized light couples to the -K (blue) valley. Figure and caption reprinted from [10].

spin-orbit interaction [9]. This effect is termed spin-valley coupling, and results in the valley polarization of the charge carriers strongly coupling to their spin polarization [10]. This results in a valley-dependent optical selection rule shown in Fig. 1.1b, meaning that $\sigma+$ ($\sigma-$) light couples strongly to the +K (-K) valley, critically allowing us to optically excite and detect the charge carriers spin and valley information.

The broken inversion symmetry also means that the inequivalent +K and -K valleys have opposite Berry curvatures. This enables the observation of the valley Hall effect, in which the Berry curvature serves as an effective magnetic field that deflects carriers differently depending on their valley polarization, resulting in spatially separated valley-polarized currents. This effect has given birth to the field of valleytronics, in which the valley degree of information is used to store and carry information, and

is yet another unique property of TMDs that make them interesting for quantum information applications [10].

1.2.2 Phonons in transition metal dichalcogenides

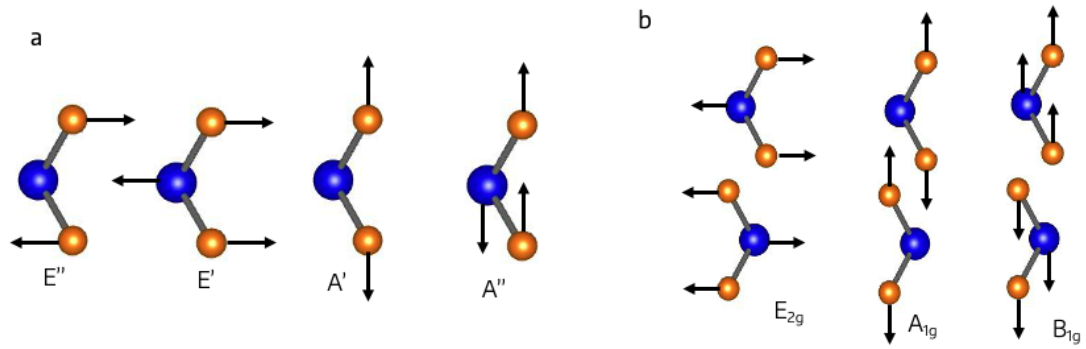

Figure 1.2: Examples of phonon modes in (a) monolayer and (b) bilayer TMDs.

Phonon modes, which are the quantized vibrational modes of a crystal lattice, play a huge role in the optical and electronic properties of TMDs. Monolayer TMDs have a symmetry group of D_{3h}, meaning that they are symmetric under rotations of 120° around the out-of-plane axis and the crystal lacks inversion symmetry. This reduced symmetry point group gives rise to distinct Raman-active modes, with some examples shown in Fig. 1.2a, such as the in-plane E and E' modes and the out-of-plane A and A' modes.

These phonon modes become more complex in bilayer TMDs, where the symmetry group changes to D_{3d}, meaning that the lattice still has threefold rotational symmetry as in the monolayer case, but now also has an inversion center. The additional layer introduces interlayer coupling, leading to variations on the monolayer phonon modes, and introduces new possible modes. Some examples are shown in Fig. 1.2b, with the E_{2g} and A_{1g} modes corresponding to the E' and A' modes in the monolayer.

Additional phonon modes such as the B_{1g} mode (breathing mode) appear at lower frequencies, and are highly sensitive to strain, doping, and stacking order.

1.2.3 Excitons in transition metal dichalcogenides

Monolayer TMDs host intralayer excitons, which are excitons in which the electron and hole are localized to the same atomic layer. The spatial separation of the electron and hole results in an in-plane dipole moment. A doping contact to the TMD can inject charges, resulting in more complex excitonic complexes such as biexcitons and trions.

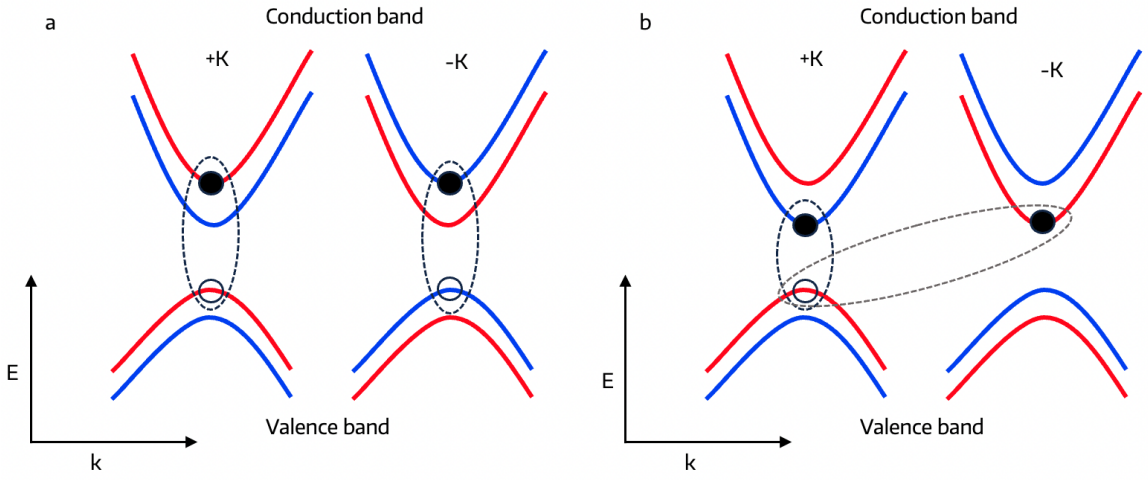

Figure 1.3: Intralayer excitons in monolayer TMDs. a) The spin-valley configurations of optically bright excitons in monolayer WX_2. b) The spin-valley configurations of optically dark excitons in monolayer WX_2, adapted from [11].

The PL spectrum of these monolayers is dominated by optically bright excitons, which are excitons that originate from the direct bandgaps at the +K and -K points of the Brillouin zone, shown in Fig. 1.3a. Because these excitons result from a set valley, they are governed by the valley-dependent optical selection rule. Also visible in the

PL spectrum are much weaker peaks, corresponding to dark excitons. One of these peaks corresponds to spin-forbidden intravalley excitons, in which the electron and hole are localized to opposite +K and -K valleys, as shown in Fig. 1.3b, circled in black [11]. The other type of dark exciton that can be seen is the momentum-forbidden intervalley dark exciton, shown in grey in Fig. 1.3b [11, 12]. These dark excitons have longer lifetimes than bright excitons due to strict recombination requirements, making them interesting for information storage and manipulation, but the drawback is that they lack clearly defined valley information like bright excitons.

In bilayer TMDs, either naturally occurring (homobilayers) or artificially stacked (heterobilayers), while intralayer excitons still exist, the excitonic population is dominated by interlayer excitons, in which the electron and hole are spatially separated into two separate atomic layers of the material. Bilayer TMDs are an indirect bandgap semiconductor, and while the degeneracy between the +K and -K valleys is no longer naturally broken, an applied voltage or magnetic field can still enable these IXs to carry valley information [13]. IXs in TMDs have many interesting properties, and there are many varieties depending on the stacking orientation of the layers. However, there are two key features that make these excitons of great interest for device integration. The indirect nature of the IX necessitates a phonon assist for recombination, resulting in significantly longer lifetimes compared to intralayer excitons. The other key property of IXs is that the vertical spatial separation creates an out-of-plane electric dipole moment, allowing for control of the exciton energy with an external electric field.

1.2.4 Electrical control of transition metal dichalcogenides

Interlayer excitons, as shown in Fig. 1.4a, will have an out-of-plane electric dipole moment equal to $\mathbf{p} = -e\mathbf{d}$, where e is the charge of an electron and $\mathbf{d}$ is the distance between the electron and hole. This dipole will be modulated with an out-of-plane electric field $\mathbf{E}$ via the linear Stark shift given by $\Delta U = \mathbf{p} \cdot \mathbf{E}$.

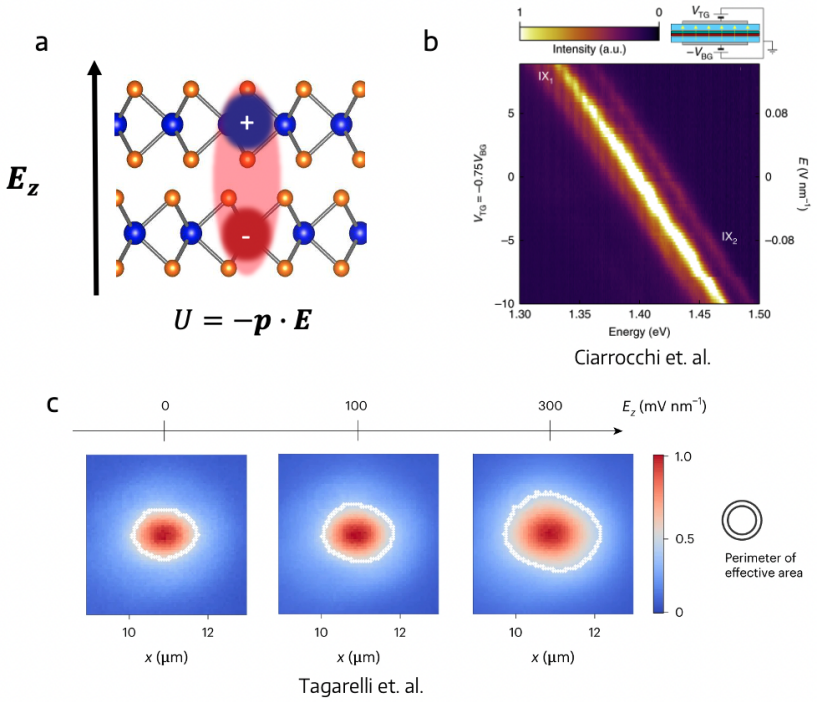

Figure 1.4: Electrical control of interlayer excitons. a) A diagram of an interlayer exciton in a TMD. b) Energy tuning of IX in a $MoSe_2/WSe_2$ heterostructure with an out-of-plane electric field, reprinted from [14]. c) Exciton diffusion in bilayer WSe_2 with different out-of-plane electric field, reprinted from [15].

An example of this is shown in Fig. 1.4b, where Ciarrocchi and collaborators shifted the energy of the IXs in a $MoSe_2/WSe_2$ heterobilayer [14]. The dipole moment of an exciton will be species-dependent based on the origin of the electron and hole within the band structure. This electric tunability is critical for integrating these IXs into application-based devices.

The electric control of IXs can be leveraged in many interesting ways. For example, in typical heterostructures, excitons diffuse over several microns, driven apart due to exciton-exciton repulsion. With an applied electric field, Tagarelli and collaborators are able to demonstrate strong control of the IX dipole moments, leading to enhanced

exciton-exciton repulsion and stronger exciton diffusion, as shown in Fig. 1.4c [15].

1.2.5 Strain control of transition metal dichalcogenides

Like with electric field, TMDs are highly tunable with mechanical strain. Because the band structure is so dependent on the hexagonal lattice, small amounts of strain can greatly impact the bandgap, impacting which species of excitons are favored. This will also impact phonon behavior and charge carrier behavior. For example, Fig. 1.5a demonstrates a redshift in the intralayer exciton energy of monolayer WSe_2. In addition to the energy shifting, there is also a substantial decrease in the exciton linewidth, which is attributed to the suppression of phonon-mediated exciton scattering [16].

Additionally, tensile strain has been shown to enhance electron and hole mobility in monolayer MoS_2, as shown in Fig. 1.5 [17]. A final example is that as the hexagonal lattice is disrupted, the phonon modes will be affected. As shown in Fig. 1.5c, in-plane strain leads to the shifting of various phonon modes in monolayer WSe_2 [18].

1.3 Applying strain to two-dimensional materials

There are many methods to apply strain to 2D materials. Some of these methods are static, where the strain is fixed over the course of the exciton lifetime. Other methods are dynamic, meaning that the strain at a specified point changes on the time scale of the exciton lifetime. Different methods of strain applications have different advantages and disadvantages, which we will discuss in further detail. Here, we will only focus on methods that are able to deterministically create strain, meaning they are able to reliably induce a strain at a specific location on demand.

1.3.1 Methods of static strain application

TMDs have some of the highest mechanical flexibility observed, with conservative estimates that they can withstand up to 10% tensile strain [9]. Transferring these

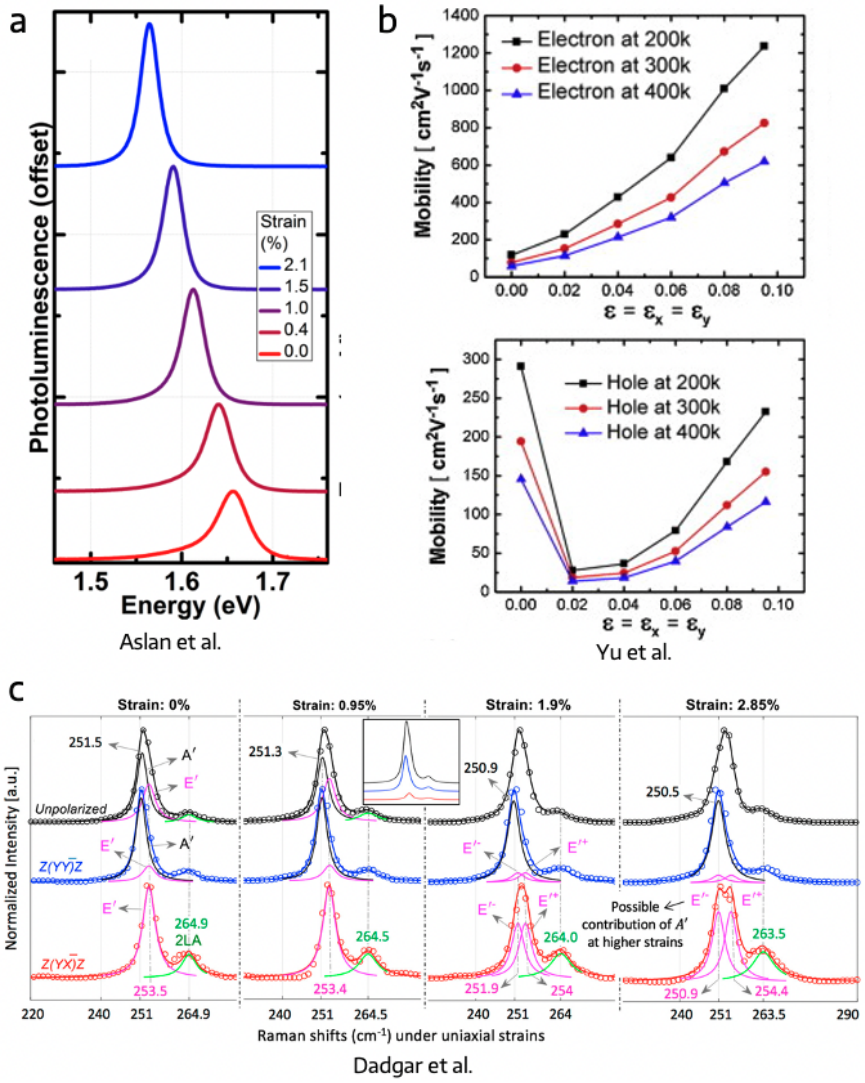

Figure 1.5: Strain modulation of TMDs. a) Strain-dependent PL spectra of monolayer WSe2, reprinted from [16]. b) Electron (top panel) and hole (bottom panel) mobility in MoS_2 with in-plane strain at different temperatures, reprinted from [17]. c) Unpolarized (black, parallel-polarized (blue), and cross-polarized (red) Raman spectra of monolayer WSe_2 under various strains, reprinted from [18].

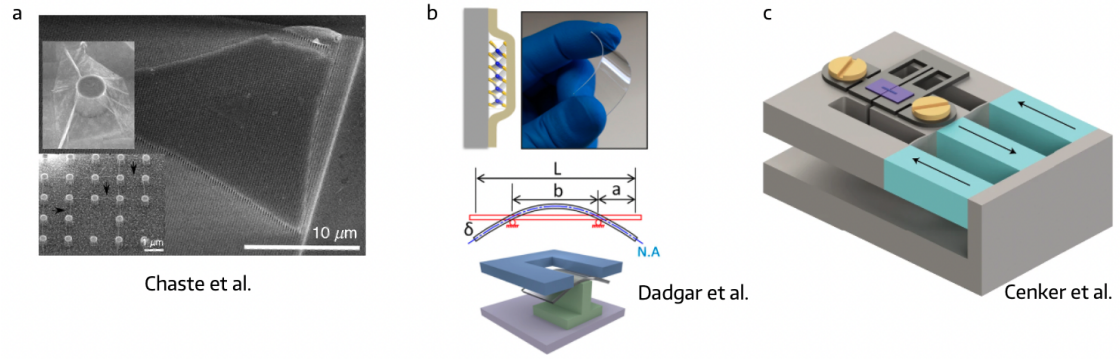

Figure 1.6: Examples of static strain methods. a) 2D material strained over a nanopillar array, reprinted from [19]. b) 2D material encapsulated in a polymer and bent, reprinted from [18]. c) A diagram of a piezo-based strain cell to apply multiple strains to 2D materials, reprinted from [20].

TMDs directly on top of an array of nanopillars is one of the most effective ways to induce strain that approaches this limit. The 2D material folds around the nanopillars, as shown in Fig. 1.6a, where they estimate that they are able to achieve a maximum 2% strain within the material [19]. The strong and highly localized nature of the strain induced by the nanopillars makes them a popular method to induce single photon emitters. Local strain creates a funneling effect that sends excitons from the larger bandgap regions of lesser strain to the smaller point-like bandgap regions where the strain is maximized [7]. A key issue with this method of strain creation is that it is not tunable. Upon transfer of the material on top of the nanopillars, the strain profile is fixed. Additionally, these nanopillars must be pre-fabricated on a substrate, and the height profile makes integration with photonic structures difficult.

A more tunable method of strain control is shown in Fig. 1.6b, where the authors encase the 2D flake in a flexible polymer and press down on the edges of the substrate. This resolves a major problem experienced by the nanopillars, in that the strain can be tuned by how much pressure is put on the edges of the substrate. However, this

method does not allow for the 2D material to be on a standard substrate where it could be integrated with photonic or electronic structures, and the strain profile across the 2D flake will be non-uniform.

Shown in Fig. 1.6c is a piezo-based strain cell pioneered in [20]. The 2D material is transferred on top of a small gap and is pinned down on either side, where piezo stacks control the width of the gap to apply precise and uniform strain profiles across the flake. While this method is very exact, tunable, and uniform, it still is not on chip, and, because it requires the flake to be directly on the device, is relatively invasive.

1.3.2 Methods of dynamic strain application

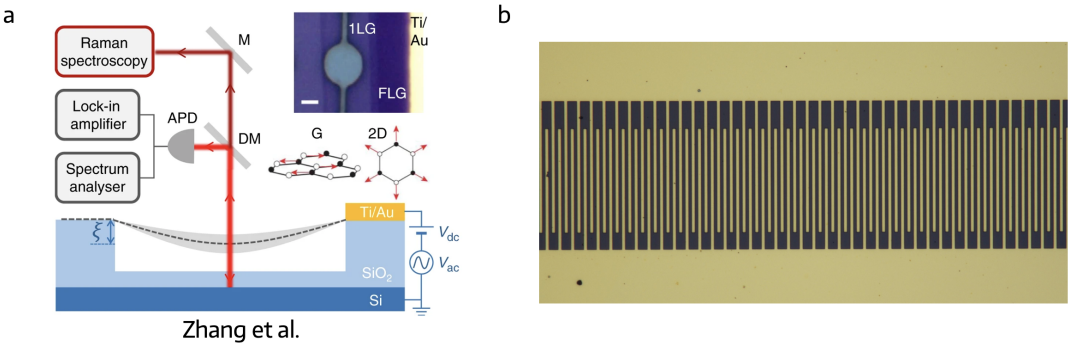

Figure 1.7: Examples of dynamic strain methods. a) A diagram of a graphene-based nano-drum resonator, reprinted from [21] b) An optical image of an interdigital transducer for creating surface acoustic waves.

Several methods exist to apply dynamic strain to materials. Unlike static strain, dynamic strain modulates the forces on a material on the scale of the exciton lifetime, allowing for direct interaction and modulation of excitons, as well as the direct study of excitons during the course of a varying applied strain. One common example of dynamic strain application is shown in Fig. 1.7a. This is a monolayer of graphene

transferred over an etched hole in the substrate. By gating the graphene, a DC signal creates a net strain in the material, while an AC signal drives a dynamic "drum" like mode, creating a nano-drum resonator [21]. While this method effectively and controllably creates a dynamic strain within the 2D material, it requires the substrate to be directly etched and the 2D material to be suspended, which makes the devices very delicate.

Another example of dynamic strain, and one we will look into more in-depth, is surface acoustic waves (SAWs). Surface acoustic waves are Rayleigh-waves that have modes localized to the surface of the substrate. Shown in Fig. 1.7b is an interdigital transducer (IDT) that launches and detects surface acoustic waves. SAWs are able to propagate freely through a substrate, enabling on-chip non-invasive interaction with the 2D heterostructure. Additionally, the wavelength and amplitude of these SAWs can be controlled by the IDT finger width and the applied power, respectively. One potential disadvantage of this method is that IDTs require a piezoelectric substrate to generate the SAWs, which can create stray electric fields detrimental to device measurement, although we will discuss ways to alleviate this in future sections.

1.4 Surface acoustic waves

Surface acoustic waves provide a non-invasive method for applying strain and electric field on-chip. This, along with the intrinsic surface nature of these waves, mark SAWs as an inherently compatible platform to interface with 2D materials.

1.4.1 Background

An acoustic wave is a mechanical wave that propagates through a medium by deforming its structure through the compression and expansion of its particles. Acoustic waves can be transmitted in a longitudinal or transverse mode. In a longitudinal acoustic mode, the particles of the medium are displaced parallel to the direction of the propagating wave. In a transverse acoustic mode, the particles are displaced

perpendicularly to the direction of the propagating wave. The velocity of the wave v_{SAW} is determined by the material the wave is passing through, and is related to the wavelength λ and frequency f with the equation $f = v_{SAW}/\lambda$.

Acoustic waves have long been used as a component in electronic devices, including SONAR, which uses acoustics to detect underwater objects, and delay lines that leverage a material's relatively slow acoustic velocity to give a long delay in space. Surface acoustic waves were first described by Lord Rayleigh in 1885 with his paper "On waves propagated along the plane surface of an elastic solid" [22]. These surface waves, also known as Rayleigh waves, are mechanical waves propagating only on the surface of a material. Because these surface acoustic waves, or SAWs, are highly confined near the surface of the substrate, they are susceptible to surface perturbations, making them suitable for sensing things like mass, temperature, pressure, and more [23].

1.4.2 Interdigital transducers

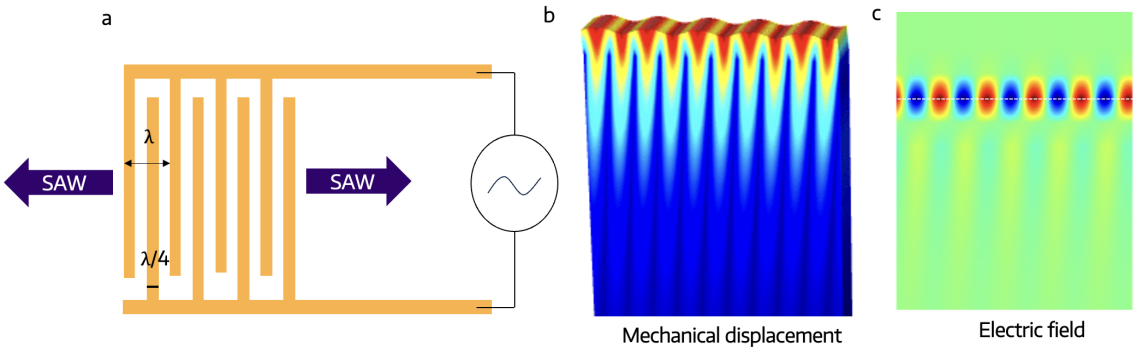

Figure 1.8: Surface acoustic wave diagram and modes. a) A diagram of an interdigital transducer. b) The mechanical displacement mode of a SAW. c) The out-of-plane electric field mode of a SAW.

To integrate these SAWs in electronic devices, we need a method of exciting and

detecting them. The first experimental demonstration was by White and Voltmer in 1965 with an interdigital transducer (IDT) fabricated on a piezoelectric substrate [24, 23]. The IDT is a series of metal electrodes (fingers) which are alternately connected to a metal bar and pad on either side of the fingers, one of which is grounded and the other of which is connected to an RF source as shown in Fig. 1.8a. Each finger and the spacing between the fingers is $\lambda/4$ wide, where λ is the SAW wavelength. By exploiting the piezoelectricity of the substrate the IDT is fabricated, the electrical signal applied to the fingers is excited into a mechanical and electrical wave that propagates through the surface of the substrate. COMSOL simulations showing these mechanical and electric modes can be seen in Fig. 1.8b and c. Connecting the IDT to a vector network analyzer (VNA) allows these waves to be launched and measured via its scattering parameters; S11 or S22 for a single IDT and S21 (S12) when looking at a SAW launched from IDT 1 (2) and detected by IDT 2 (1).

The efficiency of one of these IDTs will be determined partially by its geometry and partially by the piezoelectric coupling constant K^2 intrinsic to the substrate, commonly defined by Eq. 1.1

$$K^2 \equiv 2\frac{\nu_f - \nu_m}{\nu_f} \equiv 2\frac{\Delta\nu}{\nu} \tag{1.1}$$

Where ν_f and ν_m are the wave velocities for a free surface and a metallized surface, respectively [25]. Materials with the highest K^2 convert applied electric power to acoustic power most efficiently, and include lithium niobate, quartz, lithium tantalate, and gallium arsenide. Because piezoelectric materials are anisotropic, the cut of these substrates changes the K^2 and v_{SAW}. In this work, we rely on different cuts of lithium niobate (LN) to serve as our piezoelectric substrate, as they have some of the highest K^2 values, as well as being optically dark at the energies of the excitons we are interested in.

1.4.3 Types of IDTs

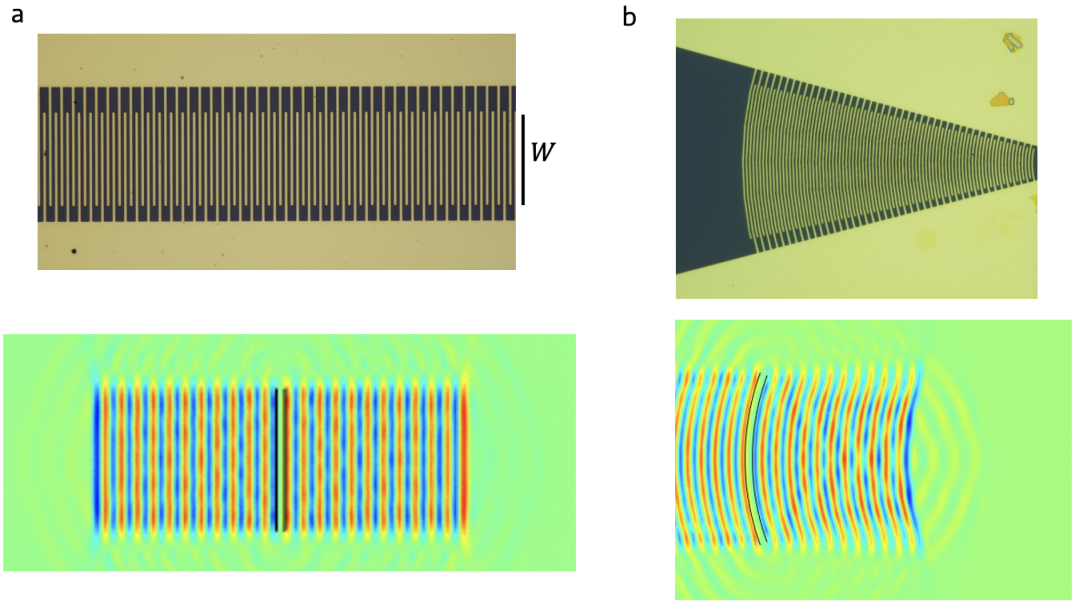

Figure 1.9: a) The top panel shows an optical image of a standard plane-wave IDT, and the bottom panel shows a simulation of the mode shape. b) The top panel shows an optical image of a focused IDT, and the bottom panel shows a simulation of the mode shape.

A standard IDT launches a plane wave with the acoustic aperture the width of the finger overlap W as shown in Fig. 1.9a. This means that the acoustic power is distributed over the length of that 1D line segment given by Eq. 1.2

$$P_{SAW} = A|\phi|^2 \frac{\epsilon\omega k}{2K^2} \tag{1.2}$$

where A is the cross-sectional area, ϕ is the wave amplitude, ϵ is the dielectric constant, $\omega = 2\pi f$, and $k = 2\pi/\lambda$. Approximating the cross-sectional area of the surface wave as $A \simeq W(1/k)$, we can write

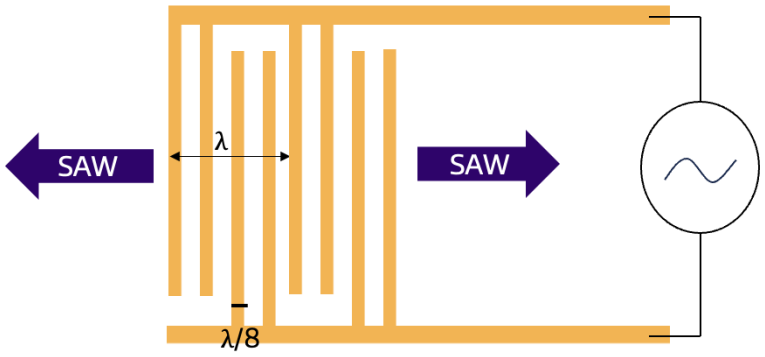

Figure 1.10: A double finger IDT design.

$$P_{SAW} = W|\phi|^2 \frac{\epsilon\omega}{2K^2} \tag{1.3}$$

Where W is the width of the acoustic aperture of the IDT as shown in Fig. 1.9a [25, 26]. A more thorough derivation can be found in Appendix A. This design is advantageous when applying a SAW over a large surface area perpendicular or parallel to the SAW propagation direction.

Plane-wave IDTs can have the standard single-finger design, as shown in Fig. 1.8a, or a double-finger design, as shown in Fig. 1.10. Although both of these IDTs are designed to excite SAWs with wavelength λ, the single-finger IDT consists of single alternating fingers, each with width and spacing of $\lambda/4$, while the double-finger IDT consists of pairs of alternating fingers, each with width and spacing of $\lambda/8$. This double-finger design aims to reduce the effect of the SAW reflection from the electrodes. Each electrode introduces a discontinuity that slightly reflects the propagating SAW due to a local change in characteristic impedance [26]. While these reflections are individually weak, they can constructively interfere at the design frequency f_0 (2λ) due to the bidirectional excitation of SAWs. In contrast, the double-finger ge-

ometry introduces a reflection path difference of λ, causing destructive interference at $f_0/2$ (λ) and thus minimizing net reflections [26, 27]. For this reason, double-finger IDTs are preferred in larger devices. However, they require patterning features that are half the size of those in single-finger IDTs, which can be challenging at higher frequencies for photolithography and electron-beam lithography.

An alternative to a plane-wave IDT is a focused IDT, shown in Fig. 1.9b. This IDT has fingers that are curved to focus towards a single 0D point, the location of which is determined by the curvature of the fingers. This design enables much greater acoustic power per aperture width as seen in Eq. 1.3, and is advantageous if the goal is to maximize the effect of the SAW at a specified point.

1.4.4 Standing waves

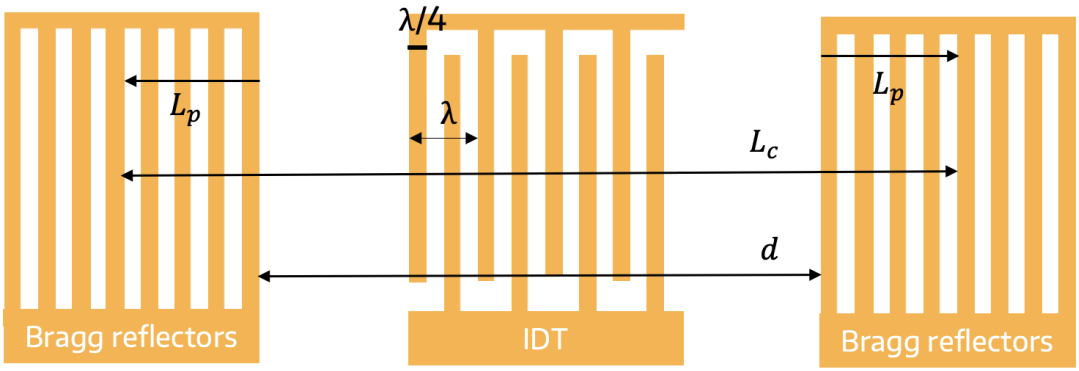

Figure 1.11: A diagram of a SAW resonator

All of the IDTs we discussed launch traveling SAWs. To generate a standing wave SAW, we can add reflector arrays on either side of the IDT to form a SAW resonator [28]. These Bragg reflector arrays are essentially shorted IDTs with the same periodic structure. These reflectors are separated by a distance that allows for the successive reflections off of each finger to constructively interfere to form a Fabry-Perot type

cavity.

Like IDT fingers, each finger in the reflector array has a small reflectivity r, and the reflector array has a total reflection coefficient at f_0 given by $R \simeq \tan(Nr)$ where N is the number of reflectors in the array. We see that R will approach 1 as $N|r| \gg 1$ [26]. Each reflector causes a small fractional change in the velocity of the wave given by $(v - v_0)/v_0$, resulting in a small impedance mismatch. This impedance mismatch will result in losses to the SAW signal through conversion to other acoustic modes. Therefore, a smaller r is desirable while still trying to maximize total reflection R.

$L_p/\lambda = |r|/4$ gives the depth into the reflector array that the SAW propagates, and the total cavity length can then be calculated with $L_c = 2L_p + d$ where d is the distance between the two reflector arrays, as shown in Fig. 1.11 [26]. The SAW resonator can be characterized by an unloaded quality factor Q_u, which is proportional to the number of times the wave travels back and forth through the cavity before its energy is dissipated. This quality factor takes into account only the properties of the cavity itself and is given by Eq. 1.4.

$$Q_u = \frac{2\pi f_0 L_c}{R_c} = \frac{\pi L_c}{\lambda_0(1 - R)} \tag{1.4}$$

For more details on the origin of the equations in this section, see Appendix A.

1.5 Scope of thesis

In this work, we narrow our focus to strain engineering of 2D transition metal dichalcogenides (TMDs), with particular emphasis on applications for quantum information storage and processing. In Chapter 2, we present our work published in [29], where we demonstrate long-range exciton transport using surface acoustic waves (SAWs). This represents a significant advance in achieving controlled, directional, and non-invasive transport of excitonic states, laying the groundwork for excitonic circuits that can shuttle quantum degrees of freedom across TMD heterostructures.

In Chapter 3, we turn to our work published in [30], in which we realize highly tunable interlayer excitonic quantum emitters (QEs). These emitters are dynamically controllable in energy via applied electric fields, and intriguingly exhibit unexpected coupling to discrete phonon modes intrinsic to the TMD. This novel single exciton–phonon mode coupling is also highly tunable, opening up the possibility of encoding quantum information into the robust phonon modes of TMDs and retrieving it optically via the emitters.

Chapter 4 explores our ongoing work leveraging SAW resonators to dynamically modulate excitonic properties in TMDs. We show preliminary results demonstrating modulation of both free excitons and tightly confined quantum emitters. Additionally, we observe intriguing long-lived changes induced by SAW pulses at cavity resonances, highlighting the versatility of using high-Q acoustic cavities. This platform creates a natural intersection between our work on long-range exciton transport and tunable QEs, offering a promising route toward on-chip quantum information manipulation that integrates strain, phonons, and excitons in a single architecture.

Finally, in Chapter 5, we summarize the key takeaways from this body of work, discuss future research directions, and articulate how these studies collectively advance the pursuit of controllable, strain-engineered quantum platforms based on 2D materials.

Chapter 2

TRANSPORTING 2D EXCITONS WITH SURFACE ACOUSTIC WAVES

This work has been published as *Long-range transport of 2D excitons with acoustic waves* in *Nature Communications* (link).

2.1 Abstract

Excitons are elementary optical excitation in semiconductors. The ability to manipulate and transport these quasiparticles would enable excitonic circuits and devices for quantum photonic technologies. Recently, interlayer excitons in 2D semiconductors have emerged as a promising candidate for engineering excitonic devices due to their long lifetime, large exciton binding energy, and gate tunability. However, the charge-neutral nature of the excitons leads to weak response to the in-plane electric field and thus inhibits transport beyond the diffusion length. Here, we demonstrate the directional transport of interlayer excitons in bilayer WSe_2 driven by the propagating potential traps induced by surface acoustic waves (SAW). We show that at 100 K, the SAW-driven excitonic transport is activated above a threshold acoustic power and reaches 20 μm, a distance at least ten times longer than the diffusion length and only limited by the device size. Temperature-dependent measurement reveals the transition from the diffusion-limited regime at low temperature to the acoustic field-driven regime at elevated temperature. Our work shows that acoustic waves are an effective, contact-free means to control exciton dynamics and transport, promising for realizing 2D material-based excitonic devices such as exciton transistors, switches, and transducers up to room temperature.

2.2 Background and motivation

Excitons in semiconductor systems can be optically excited and read out, thereby encoding and storing optical signals into the excitons' spin, valley, and orbital degrees of freedom [31, 32, 10, 33]. Analogous to electronic circuits, circuits with excitons as the active information carriers have been envisioned, which transport and manipulate excitonic states with applied electrical and magnetic fields [34, 35]. Transducing between photons and solid-state media, such excitonic circuits can directly process optical signals and regenerate light without additional optical-electrical conversions so that they can be very efficient [35].

2.2.1 Previous methods of exciton transport in TMDs

Many previous methods of exciton transport in TMDs have focused on methods to increase exciton diffusion, as shown in Fig. 1.4c from [15], where electrical control of the IXs was used to increase the diffusion length.

Another example is shown in Fig. 2.1, in which the authors demonstrate that increasing the optical power of the pump laser can greatly increase the spatial diffusion length of neutral IX in a TMD-based van der Waals heterostructure [36]. This is attributed to the increase in IX density, leading to increased exciton-exciton interactions that drive them further away from the excitation site.

Although focusing on enhancing exciton diffusion does indeed enable further exciton transport, this method has fundamental limitations. First, these techniques used for enhancing IX diffusion as in [15, 36] both rely on exciton-exciton repulsion to drive exciton transport. This means that the transport is exciton density specific, and would not work in quantum situations requiring a low exciton density. Second, exciton diffusion is not directional, meaning that although the excitons do travel further than they otherwise would, they are not being steered, which is preferable for creating an excitonic circuit.

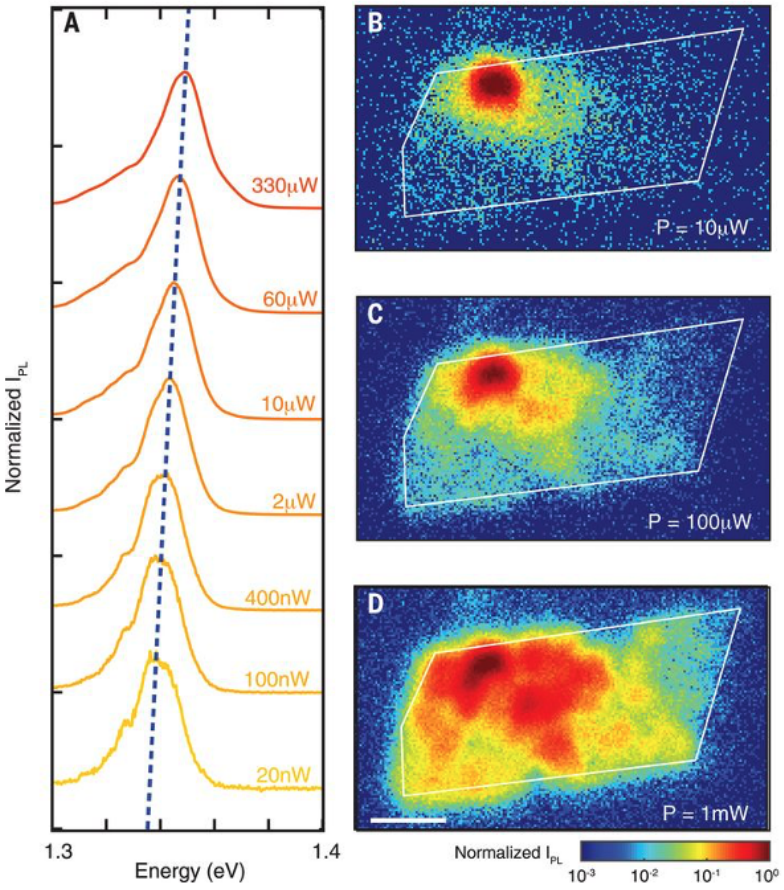

Figure 2.1: Spatial control of neutral interlayer excitons. a) Power (P) dependence of the normalized PL spectra collected from the same spot as the excitation. The blue dashed line corresponds to the PL peak position versus power. b,c,d) Spatial dependence of the intensity of the normalized PL for P = 10, 100, and 1000 μW, respectively. The white outlines depict the heterostructure area. The continuous wave laser excitation (λ = 660 nm) is fixed at the top left of the sample. Scale bar, 5 μm. All measurements were performed at 4 K. Experiments performed at higher temperatures provide smaller spatial extension of PL around the excitation. Figure and caption reprinted from [36].

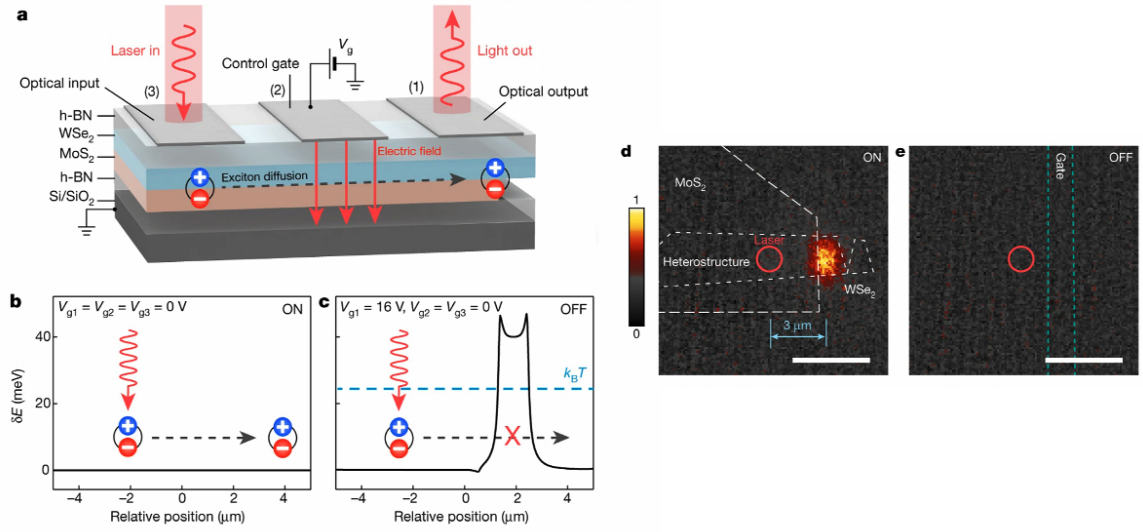

Figure 2.2: Excitonic transistor operation at room temperature. a) The application of gate voltages (V_{g1}, V_{g2}, V_{g3}) to transparent graphene electrodes (gates 1-3) can engineer a potential landscape for the diffusion of excitons, controlling their flux through the device. b, c) Calculated energy variation δE for the excitons in the ON (free diffusion; b) and OFF (potential barrier; c) states. Red arrows represent laser excitation; the bound charges and black dashed arrows denote the excitons and their diffusion, respectively. d, e) Corresponding images of exciton emission. Dashed lines indicate the positions of the different layers that form the heterostructure and the top graphene gate (gate 1). The laser spot is represented by the red circle. Colour scale indicates the normalized photoluminescence intensity. Scale bars, 5 μm. Figure and caption reprinted from [37].

The other primary method for IX transport is using a series of gates to bias the excitons towards a specific direction of motion. An example of this is shown in Fig. 2.2 from [37], where the authors demonstrated an electrically controlled excitonic switch. In this switch, gate biases enable or disable directional IX diffusion across a defined region, allowing for the creation of an excitonic transistor. This method improves on

previous work by demonstrating directional and switchable exciton transport. However, there are still two major issues. The first is that the application of the electric fields requires a series of gates to be patterned directly on top of the TMD heterostructure, which is invasive and could result in unwanted effects within the heterostructure. The second is that despite being guided by an external electric field, the exciton velocity is still dominated by diffusion, which will be material dependent and a function of temperature and exciton density. This fundamentally limits the distance the IX can travel before recombining. To demonstrate exciton transport not limited by exciton velocity, we can take a look at previous work on exciton transport in GaAs.

2.2.2 Exciton transport in GaAs

Unlike electrons or holes, charge-neutral excitons experience no net force under uniform electric fields. They can also be dissociated by a moderately strong in-plane electric field if the binding energy is small, for example, in GaAs quantum well systems [38, 39]. Therefore, diffusion has been one of the main mechanisms utilized for exciton motion in GaAs [40, 41] and 2D materials [42, 43, 44]. Particularly, in GaAs systems, the high mobility of excitons has enabled 10s of microns diffusion length at low temperature [35]. To actively transport excitons with controlled directionality, surface acoustic waves (SAWs) have been employed to effectively transport excitons in GaAs quantum wells [45, 46, 47, 48, 49]. Hundreds of microns transport distance is achieved at a temperature below 4K [46, 47]. However, the low exciton binding energy of only a few meVs in GaAs prohibits operation at higher temperatures [50].

2.2.3 Applications of GaAs transport to TMDs

Compared to GaAs quantum wells, excitons in 2D transition metal dichalcogenides (e.g., MoS_2, $MoSe_2$, WS_2, WSe_2) have binding energies on the order of hundreds of meVs [10, 33] with strong resonances even at room temperature (RT) [51, 52, 53, 54],

making them promising for a plethora of optoelectronic and quantum applications [55, 56, 57, 58, 59].

Particularly, the indirect excitons (IXs) in bilayers and heterobilayers of TMDs have additional desirable properties [58, 60, 61, 62, 63]. Because these IXs consist of electrons and holes separated in different layers and valleys, their population lifetimes at low temperature are up to 100s of nanoseconds [33], facilitating long-range transport before relaxation. Importantly, IXs have a permanent perpendicular dipole moment so that their energy can be tuned with an out-of-plane electric field [64, 65], thus they can be driven by a lateral gradient of electric-field [37]. Indeed, prototypical TMD excitonic transistors have been demonstrated based on field-controlled IX diffusion in $MoSe_2/WSe_2$ heterobilayers [37, 66, 67]. The application of an out-of-plane static electric field creates an energy barrier or trap for IXs, so switching on and off the electric field can suppress or enable exciton diffusion [67]. However, due to limited exciton mobility [68], diffusive and repulsive transport of IXs can only achieve a transport distance of a few μm using milliwatts of optical excitation power at a low temperature [69]. More importantly, such diffusive transport is non-directional, thus challenging to realize functional excitonic circuits, which entail transporting excitons in a controlled direction over a long distance.

Here, we demonstrate the long-range and directional transport of IXs in a bilayer WSe_2 using SAW at temperatures up to RT. The IXs in a bilayer WSe_2 are momentum indirect with a long lifetime of up to 10 ns at 10 K and ∼1 ns even at RT [60, 67].

2.3 Device design

2.3.1 Device principle

Consider a bilayer WSe_2 flake placed directly on a piezoelectric substrate (Fig. 2.3a). SAWs are excited and propagate through the area where a bilayer WSe_2 flake is transferred. On a piezoelectric substrate such as $LiNbO_3$, the propagating SAW will

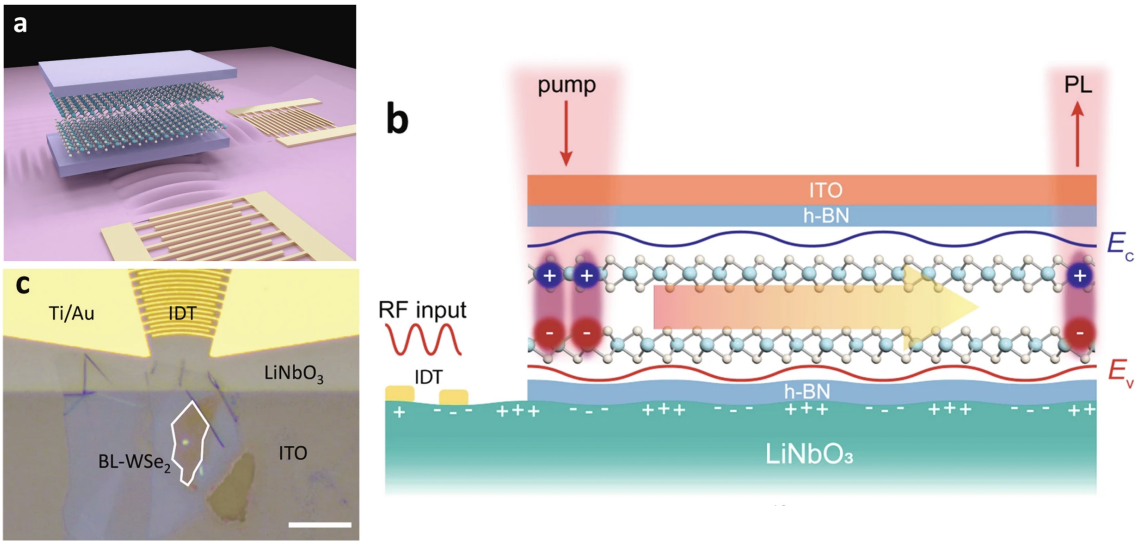

Figure 2.3: Device design of WSe_2 integrated with SAWs. a) Schematic illustration of the h-BN encapsulated bilayer WSe_2 stacked on SAW devices. The IDTs generate SAWs to transport the excitons in different directions. b) The propagating SAW modulates the energy of the excitons and transports them from the pump spot to the flake edge, where they recombine to generate photoluminescence. For simplicity, we only plot +z interlayer exciton in bilayer WSe_2. c)Optical microscope image of the device, with the white line outlining the bilayer WSe_2. Scale bar, 20 μm.

generate a near-field piezoelectric field with a large out-of-plane field (E_z) amplitude on the order of 10^7 V/m at 1 mW/μm of acoustic power density. As such, the E_z component will periodically modulate the IX energy in space and time, creating a dynamic trapping potential for the IXs in the extrema of E_z. As the SAW propagates, the IXs will drift along the time-varying gradient of E_z and thus be carried by the SAW—like surfing on a wave—to travel a long distance before they recombine (Fig. 2.3b). With a SAW velocity of 3.0×10^3 m/s and an exciton population lifetime >10 ns, the IXs can travel > 30 μm, an order of magnitude longer than the exciton

diffusion length.

Fig. 2.3b depicts the scenario when the bilayer WSe_2 is under both optical pumping and SAW modulation. Since the bilayer WSe_2 is inversion symmetric, there are two energy degenerate IXs with dipole moment $\mathbf{p}$ pointing along the +z and -z directions, respectively. For simplicity, we use +z IX to explain the transport process. The electric field $E(r,t)$ induced by the SAW modulates the IX energy by $\Delta U = -\mathbf{p}\cdot\mathbf{E}$ and thus creates a dynamic potential well moving at the acoustic velocity. At low temperatures, the optically excited IXs will quickly relax to the energy minimum created by the SAW in real space and travel with the propagating SAW. An optical image of an actual device is shown in Fig. 2.3c. To reduce the inhomogeneous broadening and exciton trapping from spatial variation of surface potential, we encapsulated the bilayer WSe_2 with 10nm hexagonal boron nitride (hBN) flakes using the standard dry pick-up method and transferred the heterostructure onto the $LiNbO_3$ substrate with pre-patterned IDTs [70]. Additionally, a thin layer of indium-tin-oxide (ITO) was deposited on the heterostructure region as a top transparent electrode. This top electrode plays an important role by efficiently suppressing the in-plane piezoelectric field component (E_x), which may cause exciton dissociation [45, 71, 72, 73], as depicted in Fig. 2.4a.

2.3.2 ITO prevention of exciton dissociation

An example of this can be seen in a control device with no ITO top cladding. In Fig. 2.4b and c, the WSe_2 flake (white outline) is pumped with a HeNe laser. The spectrometer detects the intensity of the PL spatially, without SAW (Fig. 2.4b) and with SAW (Fig. 2.4c). No transport of IXs beyond the diffusion distance can be observed. Rather, the SAW piezoelectric field dissociates the IXs into free carriers, suppressing emission everywhere and resulting in a dramatic decrease in the PL intensity.

The effect of the ITO layer on this exciton dissociation is dramatic. The finite-

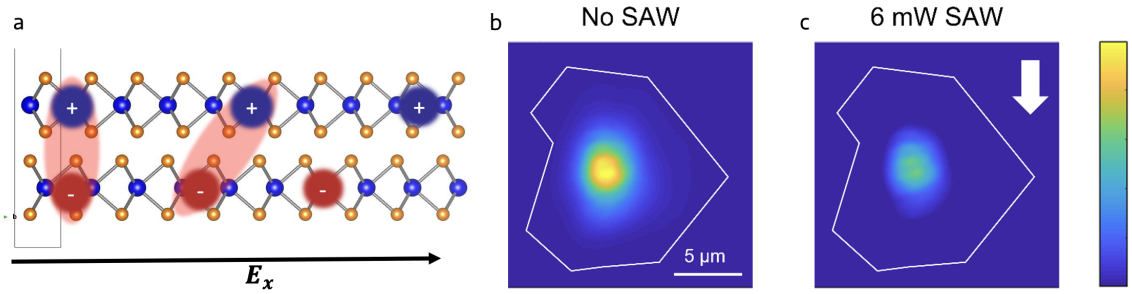

Figure 2.4: Exciton dissociation as a result of in-plane electric fields. a) Diagram depiction of interlayer exciton dissociation via in-plane electric field. The PL of a device without an ITO layer without SAW (b) and with SAW (c).

element method (FEM) simulation (Fig. 2.5a) compares the piezoelectric fields in the situations of without (top panel) and with (bottom panel) the top ITO layer, showing that the ITO layer suppresses E_x by about two orders of magnitude. For the simulation domain shown in Fig. 2.5b, we can also look at the E_x modes without (Fig. 2.5c) and with (Fig. 2.5d) the ITO layer. This allows the effect of the out-of-plane electric field to dominate the interactions with the interlayer excitons.

2.3.3 SAW generation

To successfully apply this electric field, we designed a focusing IDT structure that focuses the acoustic wave into the WSe_2 region (Fig. 2.6a) to concentrate the acoustic power density and enhance the piezoelectric field **E**. The IDT excites a strong SAW mode at 1.237 GHz with an acoustic wavelength of 2.832μm, assuming an acoustic velocity of 3.5×10^3 m/s for the z-propagating Rayleigh mode in a y-cut $LiNbO_3$ substrate. Fig. 2.6a shows the simulated electric field profile of the focused beam of the acoustic wave, which at the focal point has a waist of 3.0 μm. When designing the IDT, we tested a number of periods (N), with S11 shown in Fig. 2.6b. The device with N=42 exhibited the best impedance match, as seen in the polar S11 data in

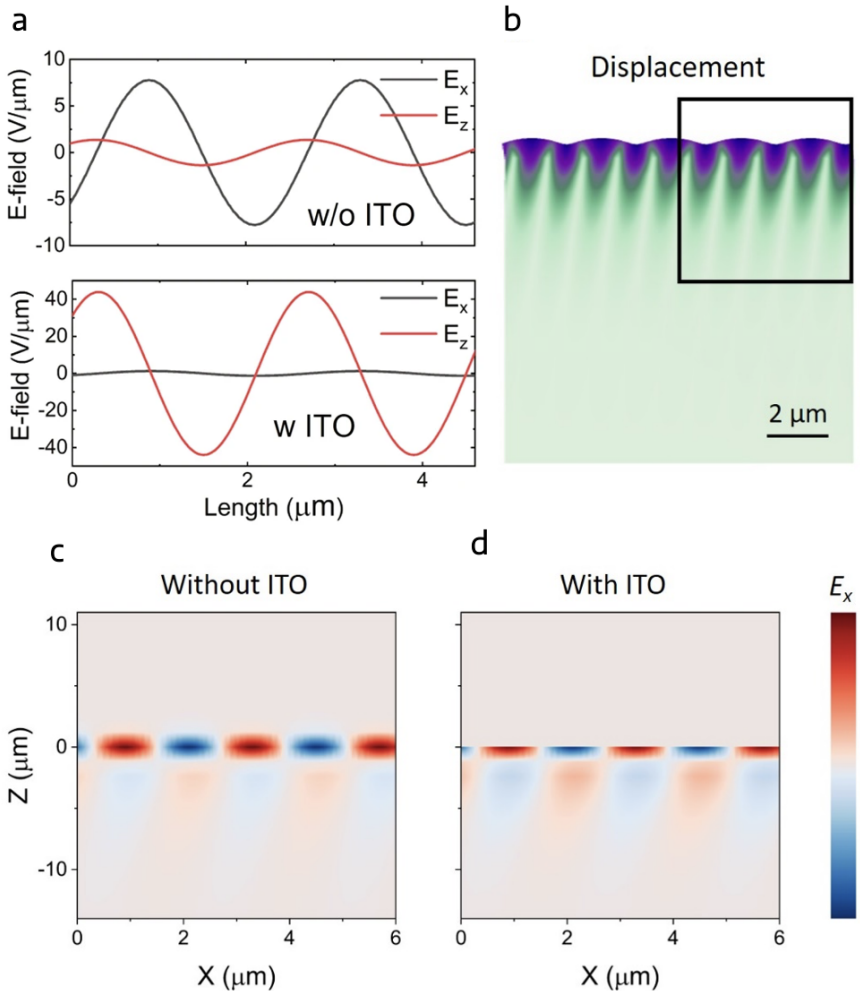

Figure 2.5: Effect of ITO layer on exciton dissociation. a) The piezoelectric field distribution with (top panel) and without (bottom panel) the top ITO electrode. The field amplitude is calculated assuming an acoustic power density of 1 mW/μm. The ITO electrode can efficiently suppress the in-plane piezoelectric field component E_x, which causes undesirable exciton dissociation. b) The magnified displacement of the SAW. c,d) the in-plane component of the piezoelectric field without (c) and with (d) ITO cladding. The ITO layer can strongly screen the in-plane field.

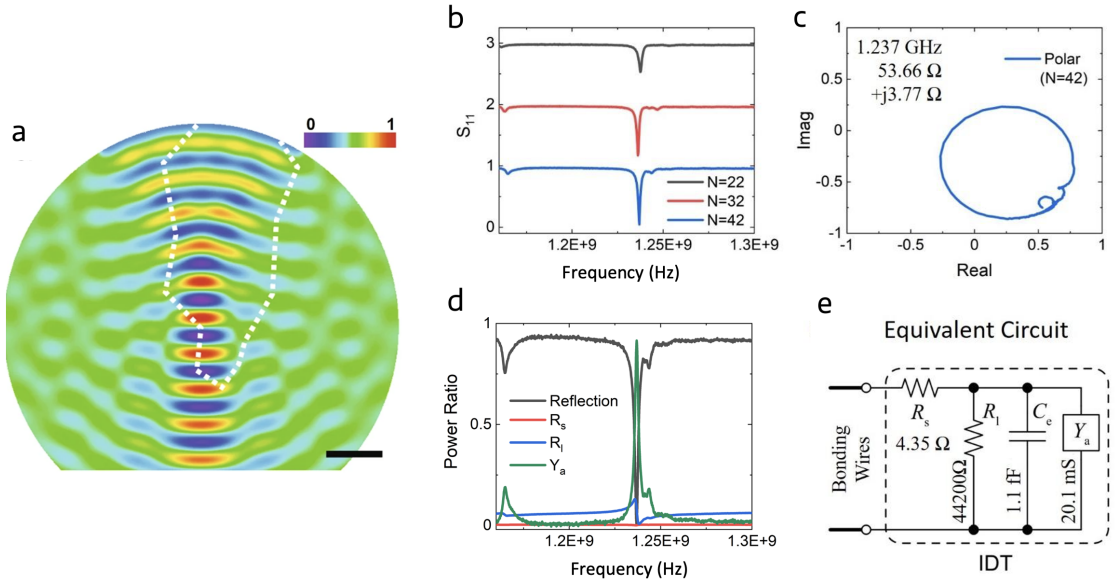

Figure 2.6: SAW mode characterization. a) The piezoelectric field profile of the SAW generated by the focusing IDT. The acoustic focal point has a waist of 3 μm and is at the edge of the bilayer WSe_2. The dotted line outlines the WSe_2 flake. Scale bar, 5 μm. b) RF reflection coefficient S11 measurement of the IDT devices with a varied number of periods N. c) the IDT resonance on a polar chart showing a strong acoustic resonance at 1.237 GHz for N=42. d) The RF power ratio for different circuit components for N=42. e) Equivalent circuit model of the IDT acoustic transducer for N=42.

Fig. 2.6c, where the on-resonance impedance is calculated to be 53.66 Ω + 3.77iΩ, closely matching the 50Ω impedance of the RF source. The RF power ratio for different circuit components (including serial resistance R_s, shunt resistance R_l, and admittance Y_a) for N=42 is shown in Fig. 2.6d. This shows that the on-resonance conversion efficiency is 91%, indicating a strong RF to acoustic wave conversion. These values were extracted using the equivalent circuit model of the IDT, shown in Fig. 2.6e.

2.4 Device fabrication and characterization

2.4.1 Device fabrication

The WSe_2 device was fabricated by the standard polymer-assisted (PC) pick-up method. The 2D flakes of hBN and WSe_2 (HQ graphene) were exfoliated to a 90 nm SiO_2/ Si substrate and then picked up using PC/PDMS (Sylgard 184) stamps. The bilayer WSe_2 flakes were identified by their optical contrast and then confirmed with PL measurements. The IDTs were patterned on a y-cut $LiNbO_3$ wafer (MTI) using electron-beam lithography (EBL). The IDT is aligned to generate SAW propagating along the z-axis of the $LiNbO_3$ wafer. Layers of 12 nm chromium and 120 nm gold were deposited using an electron-beam evaporator under high vacuum. Aligned transfer was then done by a home-built transfer stage with high accuracy so that the WSe_2/hBN heterostructure was precisely aligned at the focus region of the curved IDTs. PC residue was then removed using chloroform for 1 h and followed by a 5 min rinse in IPA. Finally, aligned EBL was performed and 50 nm indium-tin-oxide (ITO) was deposited by a sputtering system (Evatec LLS EVO) under O_2 conditioning. After deposition, the device was annealed in atmosphere at 300°C for 5 min to improve the conductivity of the ITO film, which can ensure a better screening of the in-plane field.

2.4.2 Measurement scheme

A continuous-wave HeNe laser (633 nm) was used to excite the excitons in bilayer WSe_2. With an objective lens (NA=0.42), the laser beam was focused with a diffraction-limited spot size of about 1 μm. The sample was mounted in a cryostat (Montana Instruments) with a window for optical access. Meanwhile, the RF signal was generated by a vector network analyzer (VNA) (Agilent E8362B) and then coupled to the wire-bonded device inside the cryostat. A calibration kits (Keysight 8052D) were used to de-embed the system so that the IDT resonance could be resolved. The in-

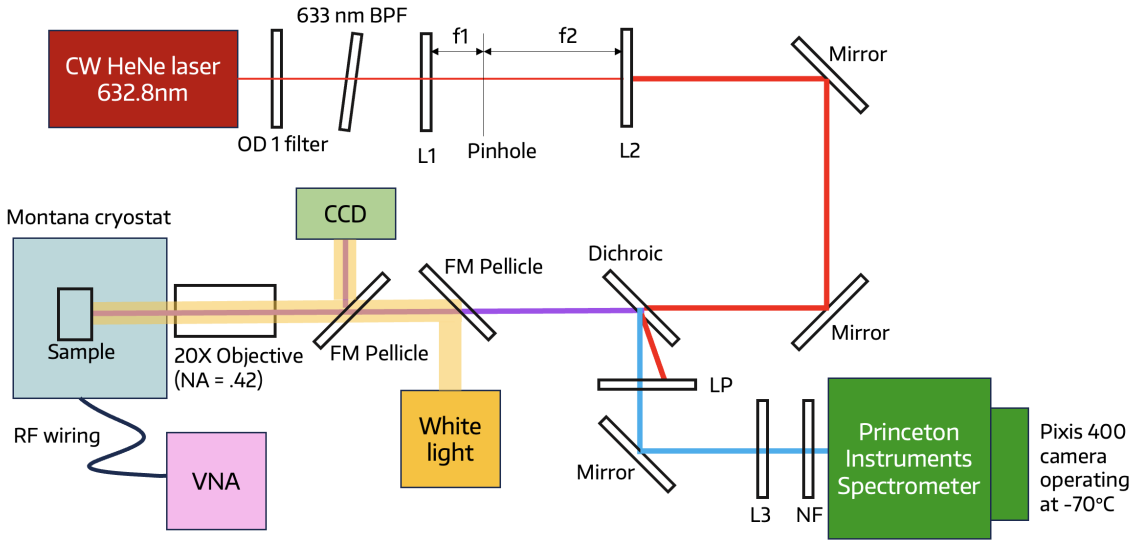

Figure 2.7: Measurement scheme for exciton transport.

terlayer exciton emission was acquired with a spectrometer (Princeton Instrument) after the laser line was removed with a 633-notch filter (Thorlabs). To image the spatial transport of the exciton, the center wavelength of the spectrometer was set to be 0 so it functioned like a mirror. The filtered signal was then collected by a cooled camera (Pixis 400) operating at -70°C to improve the signal-to-noise ratio. To collect the spectrum results, we set the center wavelength to 790 nm, which covered the emission spectrum of the interlayer exciton. To perform the spectral-PL imaging measurement of the exciton transport, the transport direction was aligned with the slit of the spectrometer and the x-axis of the CCD camera displayed the spectrum information. The y-axis signal gave the spatial emission of the bilayer devices.

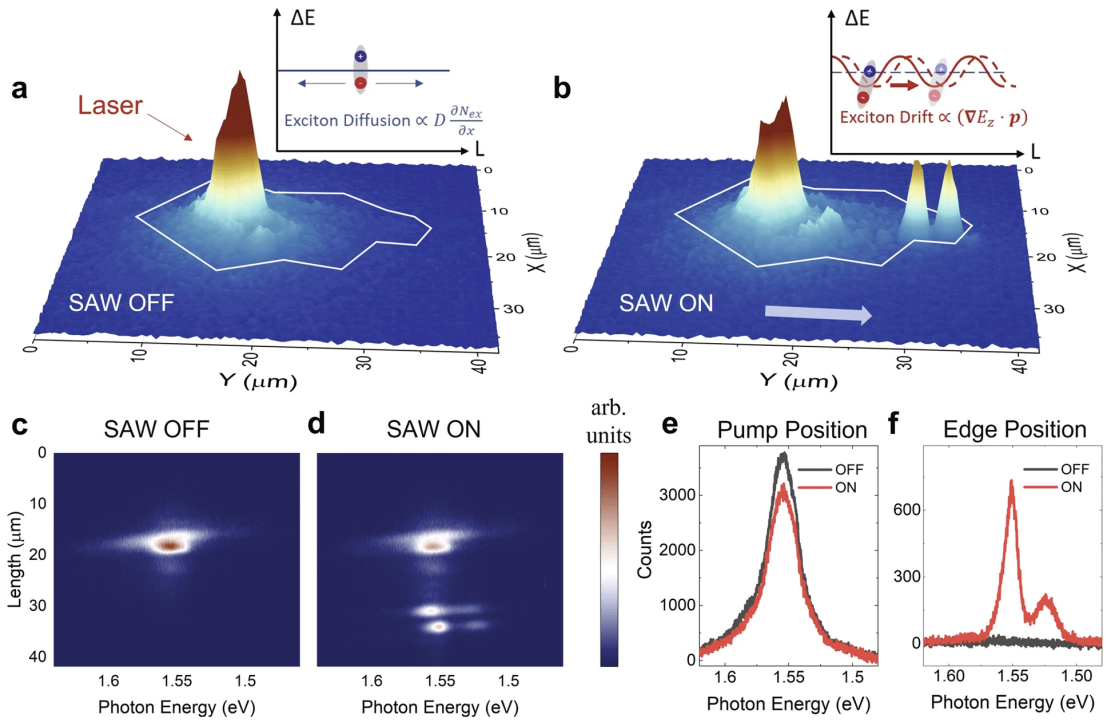

Figure 2.8: Observation of exciton transport. Real-space PL mapping (a), when SAW is off, and (b) when SAW is on with 6 mW power. Two bright emission spots appear at the edge of the flake and the focal point of the acoustic wave (see Fig. 2.6a) due to the SAW-driven transport of IXs. Insets: Illustration of free diffusion and SAW-driven drift of IXs. c, d) The spectral PL image at the same experimental conditions as a, b. The non-local exciton emission at the flake edge is clearly attributed to the IXs in WSe_2, which have an emission peak at 1.56 eV. e) The emission spectrum at the pump position slightly decreases when SAW is turned on. f) The emission spectrum at the flake edge position drastically increases when SAW is turned on.

2.5 Transport of excitons at 100 K

2.5.1 Observation of exciton transport

We first demonstrate efficient SAW transport of IXs by performing spatially resolved photoluminescence (PL) measurements. Without SAW and at a low pump power, the diffusive IX flux density can be described by the diffusion equation: $j = -D\nabla N$, where D is the temperature-dependent diffusion coefficient and N is the exciton density (inset, Fig. 2.8a). Due to the low D in TMDs, the IX diffusion is relatively weak. In comparison, when the SAW is turned on, the IX population is strongly modulated by the piezoelectric field and drifts along the SAW propagation direction (inset, Fig. 2.8b). As the velocity of the SAW (3,500 m/s) is much lower than the thermal velocity of excitons (10^4 - 10^5 m/s in our experimental condition, see Section 2.7), the IXs can be treated as an exciton gas in quasi-equilibrium. With sufficiently high SAW amplitude, the IX gas will be trapped in the energy minimum of SAW and drift with a center-of-mass velocity identical to the SAW velocity.

Fig. 2.8a,b compare the PL images measured at 100 K with SAW off and on, respectively. The IXs were excited with a HeNe laser at 633 nm, having a power of $P_p = 20$ μW, and focused to a diffraction-limited spot size of 1 μm. The excitation spot is placed near the edge of the WSe_2 flake close to the IDT and in the middle of the acoustic wave beam (Fig. 2.6a). Without SAW (Fig. 2.8a), the IXs diffuse by only 1–2 μm, consistent with previous measurement results. When SAW is turned on with power $P_s = 6$ mW, as shown in Fig. 2.8b, we observe strong exciton emission at two spots on the far edge of the WSe_2 flake, along the SAW propagation direction and 20 μm away from the pump spot. The two separate emission spots are at the corners (one convex and one concave) of the flake edge, where the acoustic wave is most focused (Fig. 2.6a). The IXs are transported at the acoustic velocity of 3500 m/s, so the traveling time is less than 6 ns, shorter than their lifetime [60]. The results reveal SAW-driven transport of IXs over a device-size limited distance, setting

the lower bound of the propagation length to 20 μm.

To confirm that the transport is indeed from IXs, we performed spatial and energy-resolved measurements. We aligned the slit of the spectrometer with the SAW propagation direction (y-axis) and acquired spectral PL images with SAW off and on (Fig. 2.8c, d). The emission of the transported IXs are predominantly at the energy around 1.5 6eV, which agrees with the IX energy of bilayer WSe_2 [60, 74, 75]. The result is consistent with our expectation that only IXs with perpendicular dipole moments are efficiently transported by SAWs. At the pump spot (Fig. 2.8e), the IX emission slightly decreases when SAW is turned on, presumably due to the transport of IXs by the SAW. In contrast, at the far edge of the flake (Fig. 2.8f), the application of SAWs increased the IX emission intensity by more than two orders of magnitude. In control devices without the top ITO layer, no IX emission can be observed beyond the IX diffusion distance (see Fig. 2.4). It agrees with the expectation that the in-plane piezoelectric field, if not screened by the ITO (Fig. 2.5a), will dissociate the IXs to free carriers [76]. These free carriers will have a very low recombination rate in the SAW because they are spatially separated by half the acoustic wavelength (1.4 μm in our device). Therefore, we can confirm that the emission at the edge of the flake is from SAW-transported IXs.

2.5.2 SAW power-dependent exciton transport at 100 K

We next characterize the IX transport at different SAW powers P_s. We find that the transported exciton density increases monotonically with the SAW power, but the trend is highly nonlinear with an activation behavior. For $P_s < 3.0$ mW, the IX transport is negligible, and the IX emission is localized near the laser excitation spot (Fig. 2.9a). When P_s increases to 4.5 mW, two emission spots appear at the flake edge (Fig. 2.9b), suggesting activation of the transport process. When P_s is further increased to 6 mW, the exciton transport becomes so efficient that the emission intensity at the flake edge is already comparable to that at the pump spot (Fig. 2.9c). Fig. 2.9d

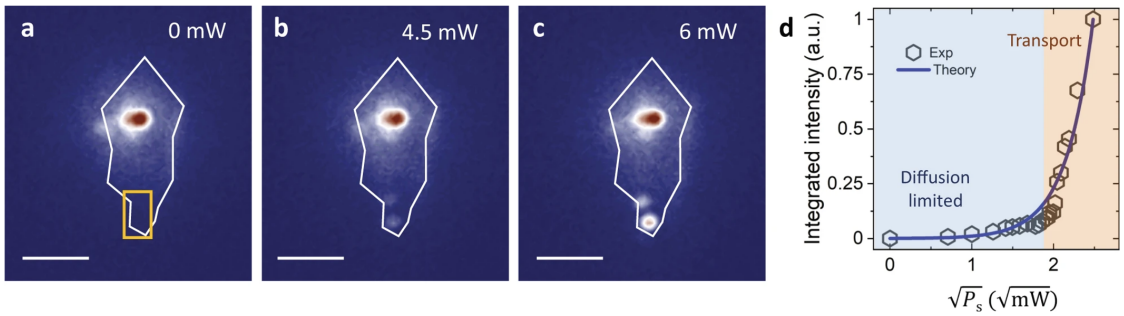

Figure 2.9: Exciton transport dependence on acoustic power. PL images at different SAW power P_s of (a) 0 mW, (b) 4.5 mW, (c) 6 mW. The solid white line outlines the WSe_2 flake. The two bright emission spots at the edge of the WSe_2 flake highlight the SAW-driven transport of IXs. Scale bar, 10 μm. d) The integrated emission intensity at the flake edge (in the area indicated by the yellow box) in (a) as a function of SAW power P_s. The experimental data is fit with the theoretical model that the transport exciton density exponentially depends on the square root of P_s. At low P_s, the exciton transport is diffusion-limited (blue shaded). A high P_s, SAW-driven transport is activated (red shaded).

plots the integrated emission intensity at the flake edge, which is proportional to the transported exciton density n_T, as a function of P_s. The experimental result agrees with our theoretical model of SAW-activated transport in which the transported exciton density n_T is proportional to $e^{\sqrt{P_s/P_t}}$ at a given temperature (see Section 2.7). Fitting the result at 100 K gives a relatively small threshold power of $P_t \sim 0.1$ mW, beyond which exciton transport is activated by the SAW. Similar exponential behavior and power law have also been observed in coupled GaAs quantum wells [45], where exciton transport is impeded by disorder and defect-induced potential variations at the low SAW power limit. In TMDs such as bilayer WSe_2, the intrinsic defect density can be $> 7.0 \times 10^{10}$ cm^{-2}, along with the strain-induced potential variation caused by

the transfer process [70]. For efficient IX transport to happen, the SAW modulation of IX energy ΔU needs to overcome the defect and strain-induced potential variation (see Section 2.7), and the efficiency of exciton transport is sensitive to the material quality.

2.5.3 Optical power dependence of exciton transport

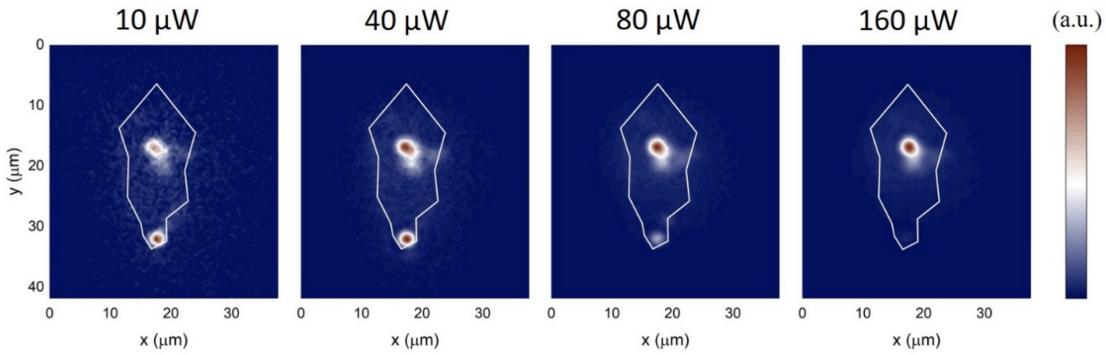

Figure 2.10: Optical power-dependence of exciton transport with 6 mW SAW power and (a) 10 μW, (b) 40 μW, (c) 80 μW, and (d) 160 μW optical power.

We can also look at the optical power dependence of exciton transport at 100 K, as seen in Fig. 2.10. The percentage of excitons transported decreases monotonically with higher optical pump power. This can be attributed to the high density of excitons screening the piezoelectric field of the SAW, which reduces the acoustic modulation of the exciton energy.

2.6 Temperature-dependent exciton transport

The activation behavior motivates us to further measure SAW-driven IX transport at different temperatures. Fig. 2.11 shows the spectral PL mapping at temperatures from 6 K to 200 K with fixed pump power $P_p = 20$ μW and SAW power $P_s = 6$ mW.

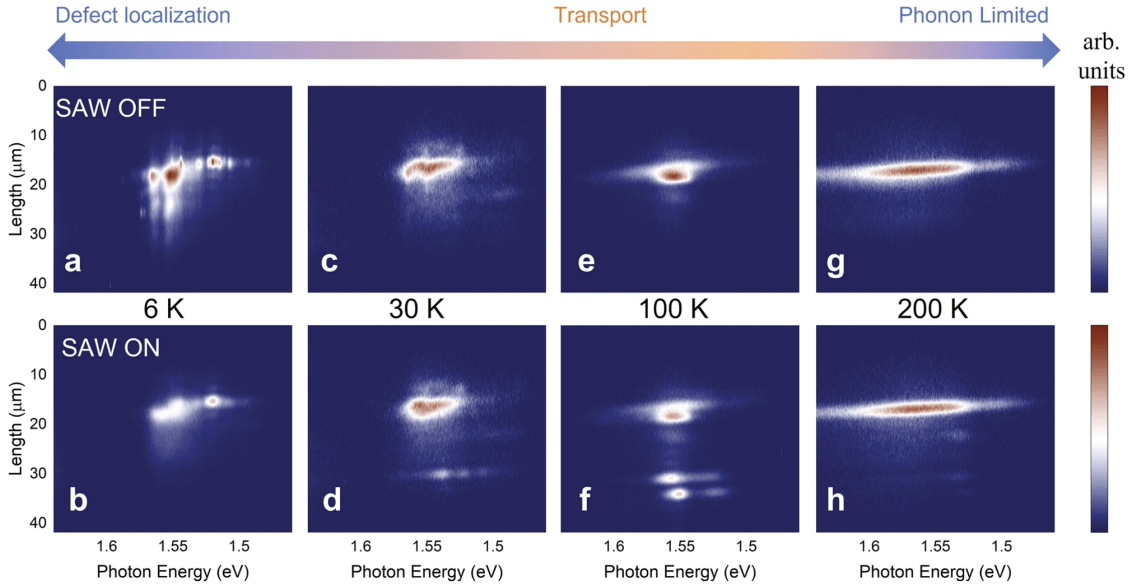

Figure 2.11: The spectral PL image of exciton transport at 6-200 K with SAW off (a, c, e, g) and on (b, d, f, h). For clarity, the data at each temperature is normalized separately. a, b) At low temperature (6 K), IXs show narrow peaks as they are highly localized to recombination centers such as defects or couple strongly to local vibrational modes. SAWs can delocalize the IXs, thereby suppressing the emission. However, the transported IXs remain dark because of the reduced phonon-assisted recombination at low temperatures. c, d) At elevated temperatures (30 K), the IXs are thermalized with broad emission. SAW transport turns on with visible emission at the flake edge. e, f) At 100 K, SAW transport of IXs is most prominent as IXs have a sufficiently long lifetime and are less susceptible to defect trapping. g, h) At even higher temperatures, SAW transport, although still visible, is inefficient as exciton-phonon scattering dominates and the IX population lifetime is short.

In this wide temperature range, we observe rich features showing the roles of exciton localization, SAW-driven transport, recombination, and phonon scattering. Note that the measurement at each temperature is normalized to its respective maxima for

clarity. At 6 K and with SAW off, the emission spectrum shows a series of sharp resonances (Fig. 2.11a), which are attributed to defect emission and phonon-assisted recombination of the IXs. When SAW is on, the sharp resonances disappear and the emission intensity decreases significantly (Fig. 2.11b). Meanwhile, IX transport at this low temperature is very weak. The suppression of IX emission can be explained by the SAW reducing the coupling between excitons and recombination centers such as defects.

When the temperature increases to 30 K, the sharp exciton resonances disappear (Fig. 2.11c). At this elevated temperature range, the excitons are thermalized into exciton gas, leading to weaker couplings with the local defects. As a result, the SAW-driven transport starts to make the PL at the flake's edge observable (Fig. 2.11d). When the temperature reaches 100 K, the IX emission becomes more than two times brighter at the pump spot (Fig. 2.11e) than at 30 K. This is because indirect IX recombination becomes more efficient when the thermal phonon density is high. The SAW-driven transport is also the most prominent at this temperature (Fig. 2.11f) because the defects and disorders have a smaller trapping effect on the thermalized excitons and the exciton population lifetime is still sufficiently long.

At 200 K (above the Debye temperature), the thermal phonon population is high. As a result, IX emission has a broad spectrum and high intensity without SAW (Fig. 2.11g). However, the IX transport is impeded due to strong exciton-phonon scattering and decreased exciton population lifetime (Fig. 2.11h). Overall, our systematic measurements have revealed three regimes of IX behaviors and the transition between them. At the lowest temperatures, the IXs are highly localized and their transport is diffusion-limited. At intermediate temperatures, the IXs are bright with phonon-assisted recombination. At the same time, they still have a long lifetime, allowing for efficient SAW-driven transport over a long distance. At higher temperatures, significant phonon scattering reduces exciton mobility and lifetime, hindering efficient transport.

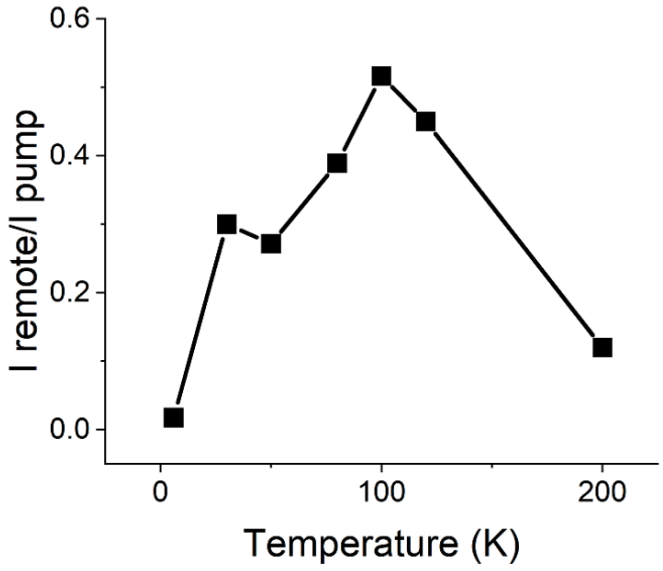

Figure 2.12: Evaluation of the exciton transport at different temperatures. The exciton emission at the edge is normalized to the emission intensity at the pump center.

Fig. 2.12 shows the ration of the intensity of the edge position relative to the intensity of the pump position at different temperatures. As we observed in Fig. 2.11, the transport is fairly low at both low temperatures (∼4K) and high temperatures (∼200K), and reaches a maximum at 100K.

Nevertheless, thanks to the strong SAW modulation, even at room temperature, we still observe a SAW-driven transport distance of ∼2.0 μm, as seen in Fig. 2.13. Here, despite the short exciton lifetime and significant phonon scattering, the exciton transport is still nearly double that from exciton diffusion.

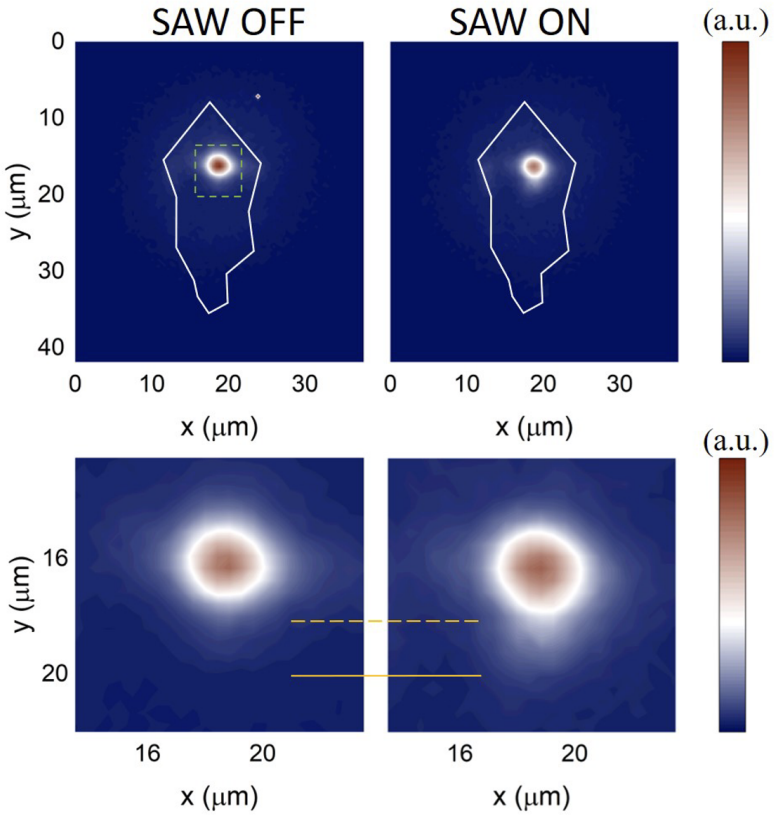

Figure 2.13: Exciton transport at 290 K. The lower panels are a zoomed in view of the dashed box. The exciton transport over ~ 2 μm can still be observed at room temperature due to the strong SAW modulation.

2.7 Theory of exciton transport

In the IXs of bilayer WSe_2, the bound electrons and holes live, respectively, in the Q (also called Λ in literature) and the K valleys of the Brillouin zone [77, 78, 79]. Due to the spin-valley locking of bilayer WSe_2, the dipole moment of an IX can point along the +z or -z directions, depending on the layer localization of the electron and the hole in the IX. Under the periodic out-of-plane electric field induced by the SAW, the two types of IXs with opposite dipoles are driven to two nearby field extrema separated

by half the acoustic wavelength and propagate together in the same direction.

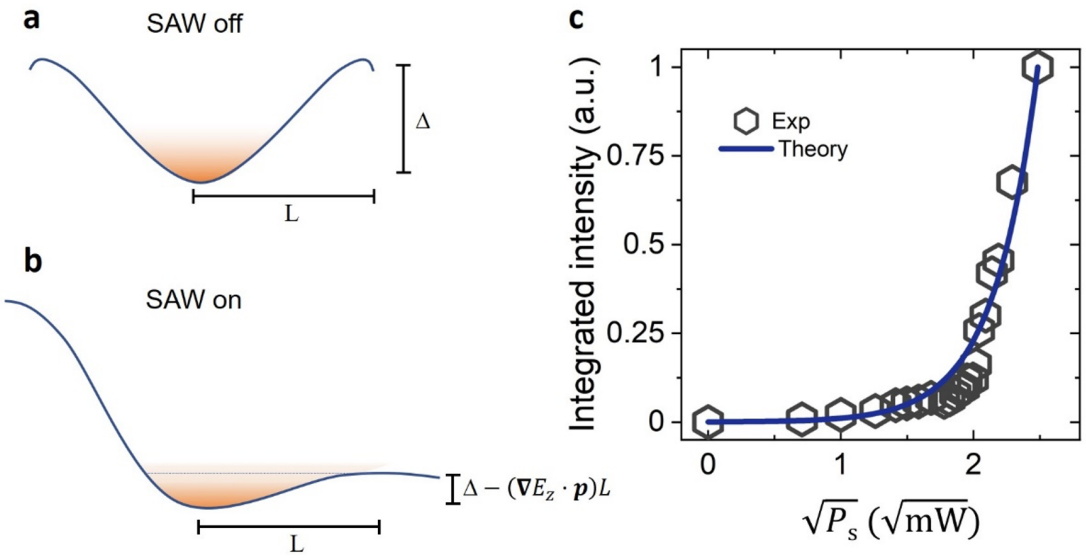

Figure 2.14: Exciton transport by surface acoustic wave under disorder potential. a) Schematic of an exciton gas in a trap with a characteristic depth in energy of Δ and length L. The exciton gas in quasi-equilibrium is shown in orange. b) Schematic of an exciton gas when maximum electric potential gradient from SAW is applied, creating a shallower potential barrier on one side of the trap. The exciton population above the dotted line can travel with SAW. (c) Fitting the power-dependent PL intensity to the SAW power.

In the temperature range of 6 K - 300 K, excitons have an average kinetic energy of 0.6 meV - 26 meV. Taking the effective mass of an exciton to be $\sim m_e$ (bare electron mass), the thermal velocity ν_{IX} of the exciton is in the range of $1.5 \times 10^4 - 9.6 \times 10^4$ m/s. This value is an order of magnitude larger than the traveling velocity of SAW ($\sim 3.5 \times 10^3$ m/s). As a result, the IX ensemble can be approximated as an exciton gas under quasi-equilibrium, when it is trapped at the minima of the slowly varying

potential energy landscape. Here, the trap can arise either from disorder or from the electric field gradient induced by SAW.

We next model the transport of excitons in a realistic bilayer WSe_2 device, assuming that the excitons do not recombine during the transport. The surface potential disorder caused by strain and other imperfections is described by potential wells that can trap excitons (Fig. 2.14a) with a characteristic barrier height of Δ and length L. If L is much smaller than the wavelength of the SAW, the electric field gradient of the SAW can help the excitons to overcome these potential barriers. An exciton that is not localized by the disorder should have kinetic energy larger than $E_{min} = \Delta - (\nabla E_{z-max} \cdot \mathbf{p})L$ (Fig. 2.14b) to overcome the barrier, where ∇E_{z-max} refers to the maximum gradient of the electric field induced by the SAW. Under quasi-equilibrium, the population n of these excitons is given by

$$n(\nabla E_{z-max}, T) = \int_{E_{min}}^{\infty} e^{-\frac{E-\mu}{k_B T}} \cdot e^{\frac{Lp}{k_b T} \nabla E_{z-max}} dE \tag{2.1}$$

where the density of states factor is taken as a step function for 2D excitons.

At 100 K, the PL intensity at the edge of the bilayer WSe_2 flake should be proportional to n. As the maximum electric field gradient induced by SAW is proportional to the square root of SAW power $\nabla E_{z-max} \sim \sqrt{P_s}$, we fit the PL intensity with $n(P_s) = n_0 e^{\sqrt{\frac{P_s}{P_t}}}$, where P_t is a temperature and sample-quality dependent factor, above which the exciton can respond efficiently to the electric field generated by SAW. Fig. 2.14c shows that this exponential dependence is consistent with experimental observations.

2.8 Conclusion

2.8.1 Discussion

In conclusion, we have demonstrated that SAW is an efficient, contact-free approach to transport IXs in bilayer WSe_2 over a distance far beyond the diffusion length. The

SAW-driven transport occurs when the SAW modulation of the IX energy can overcome local potential variations and defect traps. Since the transport distance depends on the exciton lifetime of the optically active material and the acoustic velocity of the substrate, using TMDs with longer lifetimes and a piezoelectric substrate with higher acoustic velocity can lead to a much longer transport distance. The contact-free transport, driven by an acoustic wave launched remotely, also preserves the high quality of the materials and prevents undesired effects induced by local gates [37, 66, 67, 69]. Although the maximal transport distance is reached at the temperature of 100 K in the current device, further improvement of the material quality and interface cleanness will make efficient room-temperature operation possible. We note that SAWs are a universal approach to control excitons with both its piezoelectric field and strain field, and can be utilized to manipulate and transport excitons in many other 2D material systems. SAWs can also be guided and circulated in phononic circuits and resonators [80, 81], which will afford rich functionality and flexibility.

2.8.2 Future Directions

The ability to transport excitons over long distances in 2D materials via surface acoustic waves (SAWs) opens exciting avenues for developing excitonic circuits and hybrid quantum systems. Unlike approaches relying on patterned gates or high carrier densities, the acoustic method demonstrated here offers a dynamic, non-invasive, and scalable platform to manipulate neutral quasiparticles with high spatial precision. Transport distances are currently limited by exciton lifetimes and SAW velocity, but leveraging materials with longer-lived excitonic states or designing heterostructures supporting indirect or interlayer excitons with suppressed non-radiative recombination could enable even more extended transport regimes, potentially at room temperature.

Building on this foundation, future work can explore the co-integration of SAWs with quantum emitters in 2D heterostructures to examine how localized excitonic states respond to traveling or standing acoustic waves. Such integration could enable

SAW-controlled modulation of single-photon emission properties, facilitating on-chip excitonic transistors, switches, or entangled photon sources controlled via mechanical waves.

Optimizing the interplay between temperature, disorder, and acoustic confinement remains a key challenge. While 100 K emerged as an optimal temperature for long-range transport in current devices, reducing defect densities and improving interface quality may push efficient transport to higher temperatures, which is crucial for practical optoelectronic applications. Furthermore, designing phononic circuits or SAW resonators could allow guiding, storing, or even coherently manipulating excitonic populations on-chip, paving the way toward acousto-excitonic quantum networks.

Lastly, time-resolved experiments probing exciton drift velocities and transient dynamics under pulsed SAWs would provide deeper insight into transport mechanisms, enabling refined control and new functionalities in excitonic devices.

Chapter 3

HIGHLY TUNABLE 2D BASED QUANTUM EMITTERS

This work has been published as *Tunable phononic coupling in excitonic quantum emitters* in *Nature Nanotechnology* (link) [30].

3.1 2D materials as a single photon emitter platform

3.1.1 Summary of SPEs in 2D materials

The reduced dimensionality of 2D materials affords them many quantum properties not found in bulk materials, as discussed in Section 1.1.2. These quantum properties as well as long lived exciton lifetimes at high temperatures has made quantum confinement in these 2D materials particularly interesting in recent years, as researchers search for an ideal single photon emitter (SPE) platform.

The key criteria for a single photon emitter are purity, brightness, and indistinguishability [82]. Purity is defined by second order autocorrelation measurements ($g^{(2)}(\tau)$), which characterizes the multi-photon emission probability. These measurements are performed using the Hanbury-Brown-Twiss (HBT) setup, where the signal from the SPE is sent through a beam splitter, and then each arm of the beam splitter is sent to a single photon detector. For a SPE, at zero time delay ($\tau = 0$), there will be a characteristic dip, with $g^{(2)}(0) < 0.5$ indicating single photon emission, and $g^{(2)}(0) = 0$ indicating an ideal single photon emitter. Similarly, photon indistinguishability characterizes the two-photon destructive interference by performing Hong-Ou-Mandel (HOM) measurements. The brightness of a source characterizes the maximum rate that single photons can be emitted.

Recent studies have shown that TMDs as well as hexagonal boron nitride (hBN)

are able to host SPEs. These 2D SPEs are exciting because of the long exciton lifetimes, quantum properties, and because the 2D nature of the material itself allows for easy photonic integration [83], opening up the possibility of on-chip single-photon generation, manipulation, and read-out. Both TMD and hBN emitters have advantages and disadvantages; TMD based quantum emitters are electrically and magnetically addressable, allowing their emission to be tuned, but only operate at cryogenic temperatures [82, 84]. hBN has a larger band gap, allowing hBN based emitters at room temperature, however these emitters are less tunable and have a larger spectral range [82, 6], making indistinguishability an issue. For the scope of this thesis, because we are specifically interested in devices based on tunability, we will focus on TMD and specifically WSe_2 based SPEs.

The origin and mechanism by which these SPEs operate is still an area of active research. Recent experimental studies have shown that the SPEs in WSe_2 appear frequently in strained regions, and the magnitude of the strain has an affect on spectral properties [86], and researchers were able to demonstrate near-unity yield of WSe_2 SPEs by transferring the TMD on top of predefined nanopillars that induce local strain [7]. However, strain alone is not enough to create a SPE in WSe_2. A theoretical study suggested that both defects and strain are required for the creation of an SPE [87], and experimental studies confirmed this [85]. This mechanism is illustrated in Fig. 3.1 [85], in which defect engineered WSe_2 is strained over a nanopillar. Neutral excitons created by the laser pump funnel to low-potential strained region, where they then hybridize with a defect state, allowing these (momentum forbidden) intervalley exciton emission.

3.1.2 Motivation for our work

The quantized vibrational motion in solid-state quantum systems, that is, phonons, has been exploited as an important modality that interfaces with electrons and photons for quantum information science and applications [88]. In bulk diamond, optical

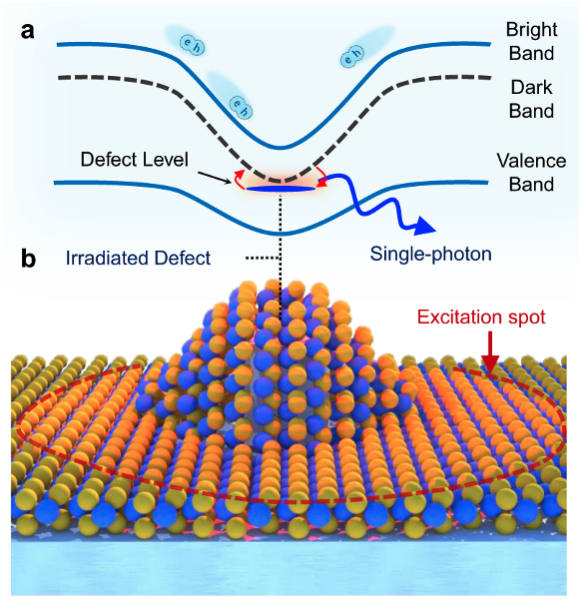

Figure 3.1: Illustration of a strain and defect engineered WSe_2 single-photon emitter. a) Denotes the spatial bandgap variations due to strain (solid blue lines represent excitonic bright band and valence band, respectively, dashed gray line represents the dark excitonic band). b) Demonstrates an illustration of 1L-WSe_2 strained over a SiO_2 nanopillar (W atoms in blue and Se in yellow). Neutral excitons, represented as e–h pairs, created within the excitation laser spot (red dashed line) funnel to low-potential strained regions. Note that WSe_2 also has a dark-exciton band at energies below the bright exciton, which is optically forbidden due to the transition selection of WSe_2. However, at strained regions and in the presence of a defect (top of the irradiated nanopillar, denoted with a blue dash), the dark-exciton can become strain-tuned to a defect-level forming intervalley defect excitons. Given that the defect-level breaks the spin-momentum locking of WSe_2, the dark-exciton state can then efficiently recombine through the defect level, giving rise to an exponentially bright single-photon emission line (outgoing blue arrow). Figure and caption reprinted from [85]

phonons with a frequency of 40 THz have been mapped to Raman scattered photons to realize non-local entanglement at room temperature [89, 90, 91]. In microscopic cavity optomechanical systems, phonons of megahertz to gigahertz frequencies have been used to store and transfer quantum states between microwave and optical photons [92, 93]. In molecular quantum emitters (QEs), coupling with the phonons of the host medium is generally considered detrimental to the quantum properties [94], although the molecule's internal optomechanical degree of freedom has been exploited [95]. These archetypical demonstrations utilize either bulk phonon modes involving collective vibration of many atoms or a phonon band including a large number of unresolved modes, resulting in a relatively low phonon–photon scattering probability or coupling rate. To further explore the phonon degree of freedom in the quantum regime, it is highly desirable to engineer new quantum light sources that afford strong phonon–photon coupling involving a well-defined single-phonon mode, preferably with an intermediate high frequency and tunable coupling strength.

QEs in two-dimensional materials [84], including TMDs, hexagonal boron nitride (hBN), and their heterostructures, provide new opportunities for engineering quantum-regime phonon–photon coupling. These atomically thin materials have bright exciton emissions and are very rich in optically (Raman) active phonon modes [96, 97]. Their multilayers further afford intralayer and interlayer phonons with a vast span of frequencies from optical to acoustic ranges. Moreover, QEs in 2D materials can be deterministically created with several approaches, such as strain engineering and ion implantation [98, 7, 85]. These techniques have enabled the site-controlled creation of QEs with a high yield and high single-photon purities. Because they are hosted in atomically thin materials, 2D QEs are amenable to photonic integration to facilitate photon extraction [83] and Purcell effect enhancement of emission [99], providing a versatile quantum system to explore phonon–photon interactions.

Here we report strong and tunable phonon–photon coupling in strain-engineered 2D QEs that are deterministically created in bilayer WSe_2. These 2D QEs emit single

photons with high purity and have a high electrical tunability in emission energy. Remarkably, in the single-photon emission spectra, multiple well-resolved phonon replica lines are observed, each of which heralds the creation of a phonon Fock state. The large phonon–photon coupling in this QE system stems from the colocalization and quantum confinement of the interlayer excitons (IXs) and the breathing-mode (BM) phonons, which directly modulates the exciton energy. The very high phonon–photon coupling strength is characterized by a large and electrically tunable Huang–Rhys factor that is, to the best of our knowledge, the highest achieved in solid-state QE systems [100, 101, 102, 103]. The demonstrated strong and tunable single phonon–photon coupling provides an invaluable resource for engineering quantum light emission systems with an internal mechanical degree of freedom for quantum information processing.

3.2 Device design

The bilayer WSe_2 is an ideal system to explore the phonon–photon interaction because it affords many Raman-active phonon modes covering a broad frequency range [104, 105]. Particularly, as shown in Fig. 3.2a, the interlayer BM phonon strongly couples with the IXs because the vertical dipole moment of an IX is modulated directly by the interlayer vibration. To explore this coupling at the single-photon level, we use a strain-engineering approach to create QEs in bilayer WSe_2 by transferring them onto patterned nanopillars [98, 7, 85], as illustrated in Fig. 3.2a. The nanopillars induce local strain that modulates the bandgap and thus creates spatial confinement of IXs in the bilayer WSe_2 [106], resulting in quantum dots that host QEs [87]. Fig. 3.2c illustrates the potential traps formed by the localized strain in the bilayer WSe_2. The optically excited IXs are funnelled into the traps where they are bound with natural defects and recombine to emit single photons. In comparison with excitons in monolayer TMDs, IXs in bilayer WSe_2 have a large out-of-plane electric dipole moment [105, 60, 107, 108]. Therefore, they couple efficiently to both a perpendicular electric field that generates a Stark shift and interlayer vibration. Stark shifts of the

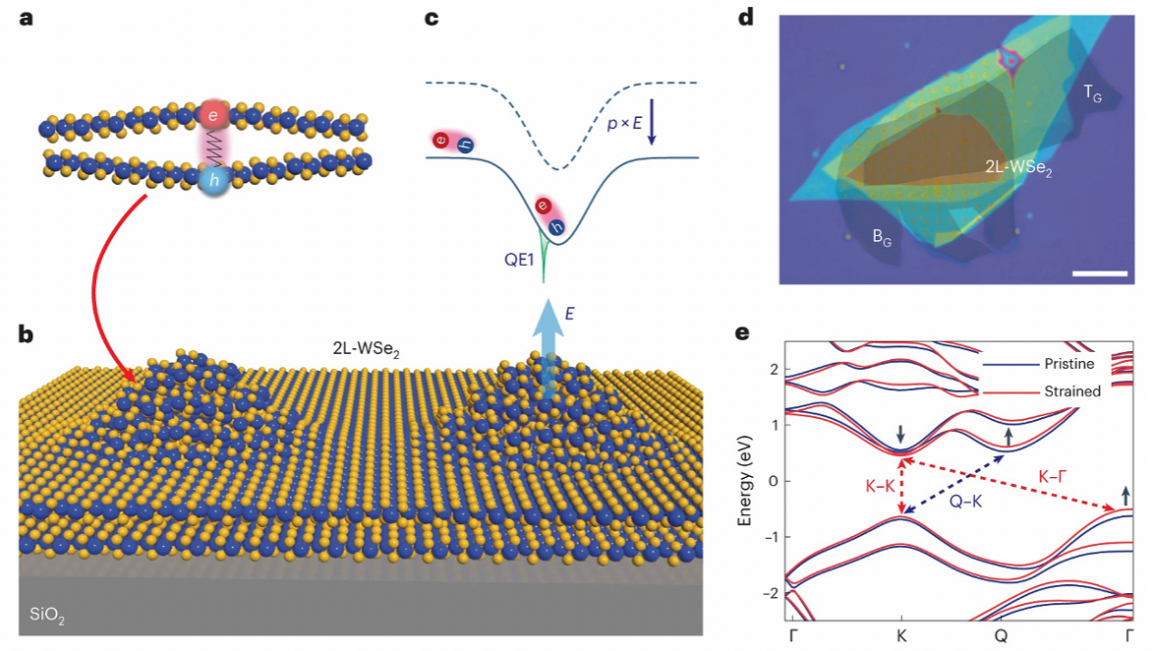

Figure 3.2: Strain-engineered 2D QEs. a) Schematic of the interlayer BM phonon which couples strongly with IXs in bilayer (2L) WSe_2 because the IX with vertical dipole moments is directly modulated by the vibrational mode. b) Illustration of bilayer WSe_2 transferred onto SiO_2 nanopillars, forming quantum dots with local strain modulation, which host the QEs. c) Strain-induced potential traps with natural defects (green dips), where excitons are funnelled into and localized. The QE energy can be efficiently tuned by electric fields through the Stark effect. d) Optical microscopy image of a representative device. The bilayer WSe_2, encapsulated by hBN and gated with top and bottom graphite layers (TG, BG), is transferred onto an array of SiO_2 nanopillars. Metal electrodes are subsequently deposited to contact the graphite layers. Scale bar, 10 μm. e) The DFT-calculated band structure of the bilayer WSe_2 in pristine (blue) and under 1% tensile strain (red) conditions.

IX energy by more than 50 meV have been achieved in bilayer WSe_2 and other TMDs [109, 110]. Multiple QEs can be created at each site in the nanopillar array

(Fig. 3.2b). Although the QEs at different sites have different emission energies due to the variation of the local parameters such as the amount of strain and the energy level of the defects, applying a local electric field to each of them using separate gate electrodes can tune their emission energies to be the same.

Fig. 3.2d shows an optical image of a fabricated device. A stack of bilayer WSe_2 encapsulated by two hBN layers (∼30 nm), with top and bottom graphite electrodes, is transferred onto a substrate with an array of nanopillars made of SiO_2. The top and bottom graphite electrodes enable electrical tuning of the QEs' energy. Fig. 3.2e shows the density functional theory (DFT) calculated band structure of bilayer WSe_2 in its pristine state and strained state with 1% tensile strain. In pristine bilayer WSe_2, indirect bandgap transition Q–K can occur, assisted by various single-phonon or two-phonon processes [105]. When under a sufficient amount of strain, the conduction band minimum is shifted from the Q point to the K point, and the valence band Γ point is shifted up such that direct K-K and indirect K-Γ transitions can become favorable in energy, enabling strong exciton coupling to zero-momentum phonons [105, 111, 112, 12, 113]. Therefore, depending on the level of local strain, IX species corresponding to either Q-K, K-Γ or K-K transitions can dominate the photon emission. These IX species have different dipole moments [108], but because their energy is susceptible to the interlayer separation, they all couple to the BM phonon strongly.

3.3 Tuning the energy of quantum emitters

3.3.1 Interlayer excitonic quantum emitters

We fabricated multiple samples. In each sample, we can find multiple QEs at different nanopillars in the array. All the measurements were performed in a cryostat at a temperature of 10 K. Fig. 3.3 shows the photoluminescence (PL) spectrum of three QEs (QE1, QE3, and QE4) as a function of top-gate voltage (with the bottom-gate grounded). The excitation laser is 632.8 nm with a fixed power of 15 μW. All three

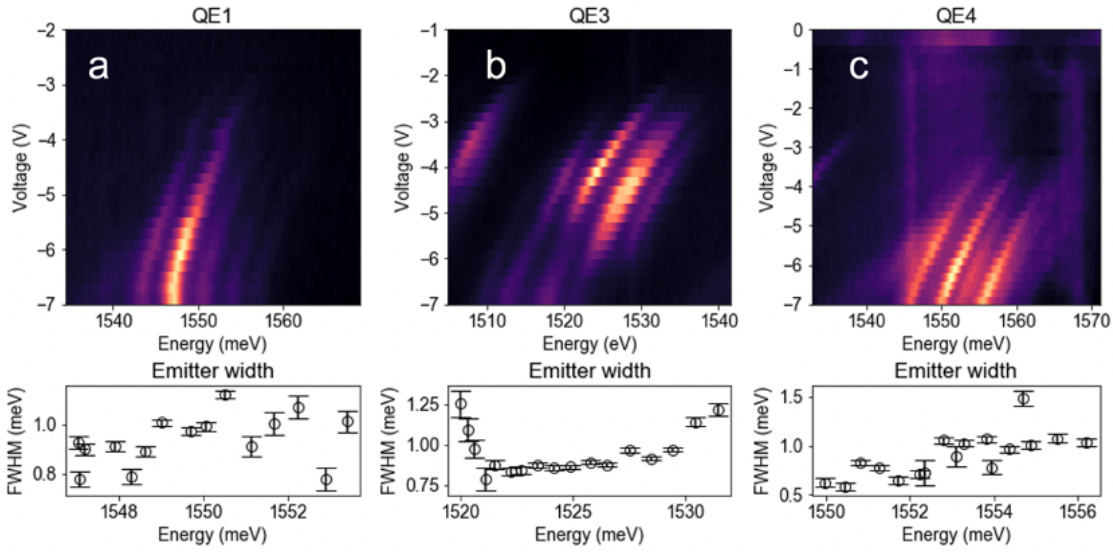

Figure 3.3: Tunable interlayer excitonic emitters. a, b, c) Three different quantum emitters. The top panel shows how the PL changes with applied out-of-plane voltage. The bottom panel shows the FWHM of the QE peak at each voltage point as a function of energy.

QEs remain dark until the gate voltage reaches a negative value of ∼-3.5 V, after which a bright, sharp PL peak is observed at 1,555 meV with a full-width at half-maximum (FWHM) linewidth of 1.1 meV. This turn-on behavior may be attributed to the IXs being bound to a donor (or acceptor)-type defect, meaning that electron (or hole) doping is needed for IX to bind to the defect and form a QE. Both donor- and acceptor-type defects in WSe_2 have been reported previously [114]. Among the 19 IX QEs in five devices (see Supplementary Fig. D.1, D.2, D.3) we have measured, 16 of them turn on at negative gate voltage, and three of them turn on at positive gate voltage. The gate voltage induces doping because of the top/bottom structure asymmetry of the devices, including the nanopillars at the bottom, and the thicker bottom hBN layer that prevents piercing by the nanopillars. There is also possible

non-negligible current leakage through the layers.

After QE1 is turned on, its emission can be redshifted by more than 6.4 meV (∼3.3 nm in wavelength) with the application of gate voltage up to -7 V. From the dipole model of field tunability, $\Delta U = \mathbf{p} \times \mathbf{E}$, we calculate the IX dipole moment of QE1 to be 0.341 e·nm, consistent with previous experimental results for K-Γ IX [105, 60, 107]. Among the 19 IX QEs we have measured (see Supplementary Table D.1), we observed three ranges of dipole moments around 0.32, 0.46 and 0.63 e·nm. Respectively, they correspond to the theoretical values of K-Γ, Q-K, and K-K IXs. As shown by the DFT-calculated band structure under strain (Fig. 3.2d) and previously reported experimental results, which type of IX dominates the QE depends on the local strain level [105, 108, 111, 74, 115, 75, 79]. Because the local strain level can vary considerably at each nanopillar, and QE formation results from the accidental occurrence of a suitable defect, the strain levels at different QEs can be very different, thereby leading to different types of IX. Even higher tunability can be achieved with QEs in heterobilayers, such as moiré excitons [116], which have an even larger dipole moment.

3.3.2 Intralayer excitonic quantum emitters

Fig. 3.4 shows the PL spectra of several QEs (QE2, QE21, and QE22), which behaves differently from IX QEs. These QEs are bright at zero gate voltage with an emission energy of 1,550 meV, which remains unchanged with varying gate voltage until ∼3.0 V when the emission is turned off. This type of QE can be attributed to defect-bound intralayer excitons, which do not couple to the out-of-plane electric field and are more rare (only three out of 22 QEs we measured). However, a sufficiently high electric field can cause electron or hole tunnelling to another layer of WSe_2, consequently turning off the intralayer exciton emission. These emitters are characterized more thoroughly in Table D.2.

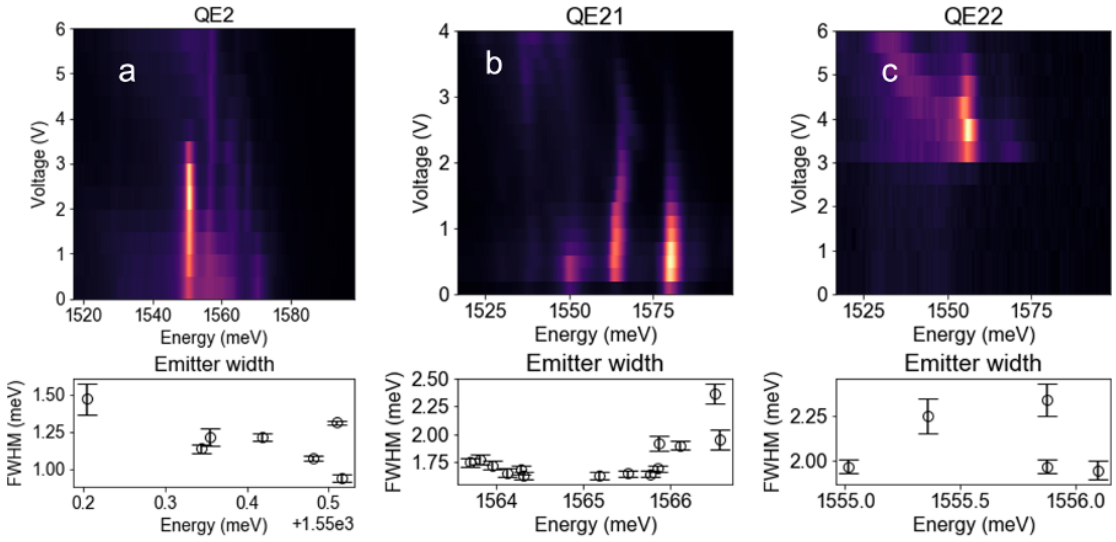

Figure 3.4: Tunable intralayer excitonic emitters. a, b, c) Three different quantum emitters. The top panel shows how the PL changes with applied out-of-plane voltage. The bottom panel shows the FWHM of the QE peak at each voltage point as a function of energy.

3.3.3 Tuning two emitters to the same energy

The different responses of the two types of QEs to electrical modulation allow us to tune them to the same energy, as summarized in Fig. 3.5e. In Fig. 3.5b,d, when gate voltages of -5.0 V and 2.0 V are applied to QE1 and QE2, respectively, both QEs emit photons at 1,550 meV with similar linewidths. Fig. 3.5f shows the second-order photon correlation $g^{(2)}(\tau)$ measured from a device (QE13 in Supplementary Fig. D.2) behaving similarly to QE1. A filter with ∼5.0 nm (9.7 meV) bandwidth was used to select the measurement range. The result shows clear antibunching with $g^{(2)}(0) = 0.169 \pm 0.005$, indicating a single-photon purity of 83%. From fitting the autocorrelation data, we estimate the QE lifetime to be 2.0 ± 0.25 ns. More details about the $g^{(2)}(0)$ measurements can be found in Section 3.6.3.

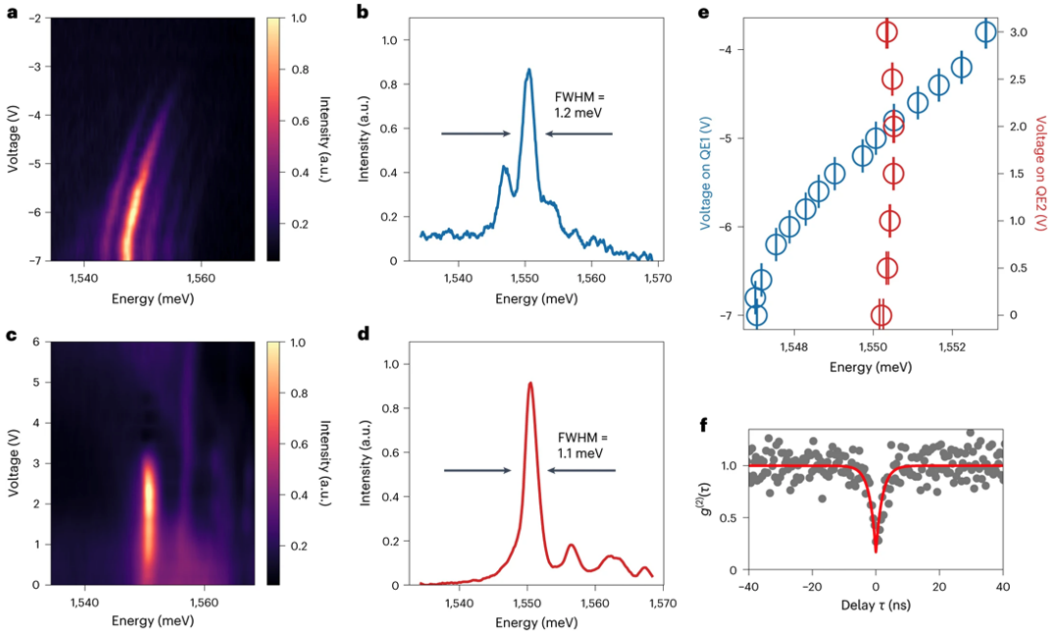

Figure 3.5: Tunable 2D QEs. a) PL spectra of QE1 as a function of the gate voltage. The emitter turns on at around -4 V and is accompanied by sidebands that are turned on at the same voltage. b) Line-cut of the PL in (a) at $V_g = -5$ V, showing an FWHM linewidth of 1.2 meV. c) PL spectra of QE2 as a function of the gate voltage. The emitter is on at zero gate bias, suggesting it has a different origin to that of QE1. At around 3.5 V, the emitter is turned off. d) Line-cut of the PL in (c) at $V_g = 2$ V, showing an FWHM linewidth of 1.1 meV. e) Modulation of emitter energy of QE1 and QE2 with gate voltage. The two QEs can be tuned to have nearly identical energy and linewidth. The center energy of the QE is extracted through a least-squares fit to a Lorentzian function of the PL spectra. The error bars represent the standard error in this fit for $n = 190$ PL points. f) Second-order photon correlation $g^{(2)}(\tau)$ measured from a representative QE, showing antibunching with $g^{(2)}(0) = 0.169 \pm 0.005$, indicating a single-photon purity of 83%. The data is shown in grey, and the fit to the data is shown in red.

The demonstrated wide electrical tuning range makes these 2D QEs promising for achieving scalable arrays of indistinguishable single-photon sources. In areas without nanopillars, we measure IX emission with a much broader linewidth > 5 meV and without antibunching, which is consistent with previous reports [105, 60, 108, 67].

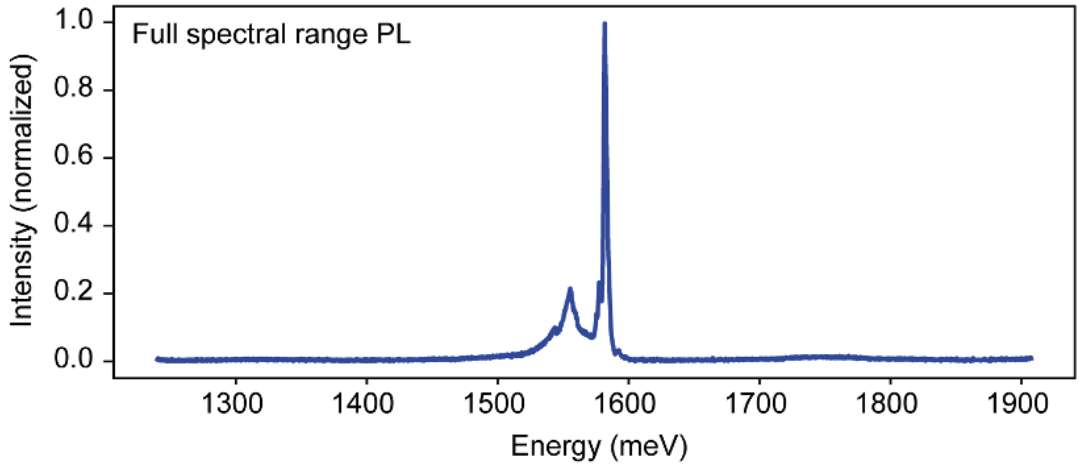

Figure 3.6: Emission over a wide energy range. PL spectrum was collected over the full range of the spectrometer to confirm that the emission only appears within the expected region corresponding to the interband transition of bilayer WSe_2. There is no emission related to below-bandgap defect states.

In addition, we observed no pronounced emission in a wide energy range below the bandgap as seen in Fig. 3.6, and therefore emission due to in-gap defect states can be ruled out. Therefore, we conclude that the combination of defect and strain engineering is necessary to create the QEs [7]. There are several possible types of defects in WSe_2, including selenium vacancies, tungsten antisites, oxygen-passivated selenium vacancies, and oxygen interstitials [87, 117, 70, 118, 119]. Although it is unclear which type of defect is responsible for forming the QE–microscopy studies are needed to reveal this–the selenium vacancy has a higher density than other types and

hence is more likely to occur at the nanopillars.

3.4 Observation and characterization of a quantum phonon sideband

3.4.1 Quantum phonon sideband

A very notable feature in the PL spectra of QE1 (Fig. 3.5a) is multiple emission lines on both sides of the main peak. These emission lines are turned on/off by the gate voltage along with the main peak and modulated at the same rate, suggesting their correlation. We observed similar features in many devices. Fig. 3.7a,b shows the PL spectra of QE1 and another QE (QE3), measured with gate voltages of -6.4 and -5.0 V, respectively. Five emission lines can be observed with spacings in the range of 3.0-3.7 meV for QE1 (Fig. 3.7a) and 3.7-5.1 meV for QE3 (Fig. 3.7b). We then measured the polarization of the photons from each emission line. As shown in Fig. 3.7c,d, photons from each QE's emission line are linearly polarized with the same orientation. Fig. 3.7e,f shows that the energies of these lines are tuned by the gate voltage synchronously at the same rate, with their spacings unchanged. All these features allow us to conclude that these emission lines originate from the same QE, rather than from other emitters nearby.

3.4.2 Polarization measurements

The polarization measurements of the QEs (Fig. 3.7c,d) were conducted with a linear polarizer mounted on a rotation stage in the signal path. The results were processed by fitting Lorentzian functions to the PL peaks to extract the central energy and peak intensity of each emission line measured with the polarizer at different angles. The amplitude of each peak at different polarization angles θ was plotted to show the angular dependence. The $\cos^2(\theta)$ dependence of a linearly polarized emitter is also plotted as a guide to the eyes. Because emitters from strained 2D materials have a randomly oriented linear polarization, these results strongly support our claims that

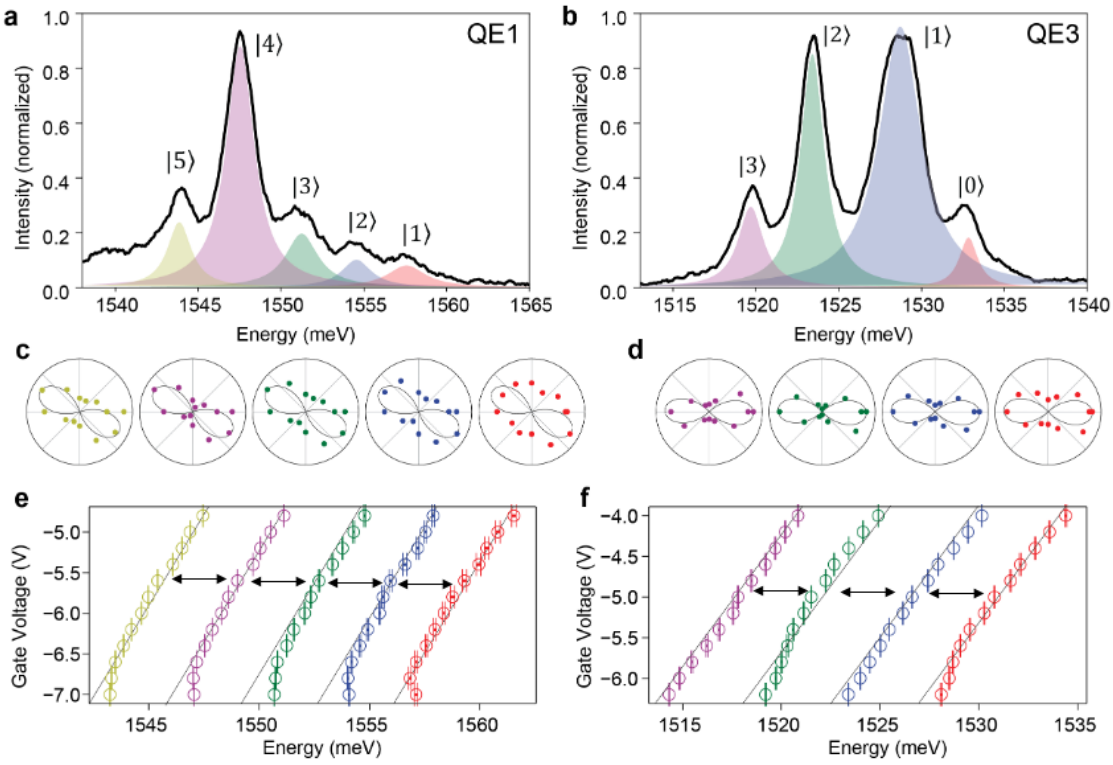

Figure 3.7: Single-phonon emission lines. a) PL spectrum of QE1 at -6.4 V. Five emission lines can be observed and are fitted with Lorentzian functions (shaded area). b) PL spectrum of QE3 at -5.0 V. Four emission lines can be observed and are fitted with Lorentzian functions (shaded area). c, d) The photons from the sidebands of QE1 (c) and QE3 (d) are polarized with the same orientation. The thin black lines are guides for linear polarization. e,f) The sideband energy of QE1 (e) and QE3 (f) is tuned by the gate voltage synchronously at the same rate with an unchanged spacing in energy. The center energy of each QE sideband is extracted through a least-squares fit to a Lorentzian function of the PL spectra. The error bars represent the standard error in this fit for $n = 400$ PL points.

these lines originate from the same emitter [7, 87, 120, 121, 122].

3.4.3 Power dependence

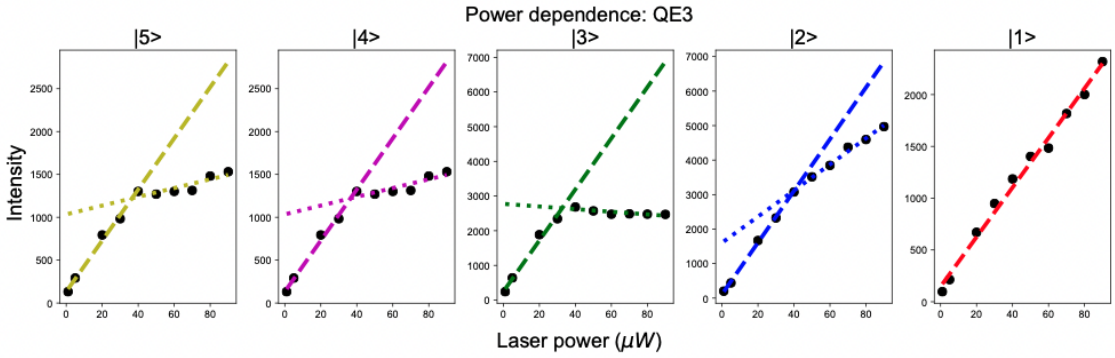

Figure 3.8: The measured data is shown as black symbols. The data is fit with linear functions (dashed lines) in two regions. The colors of the lines correspond to the coloring of the peaks in Fig. 3.7.

We further characterized the power-dependent PL of QE3 by changing the pump laser power while fixing the gate voltage. The PL was then fit with Lorentzian functions to find the central energy for each PL peak. The peak amplitude at that energy was then extracted for different pump powers. From the results, we observe a trend that the higher-order phonon lines (lower energy states) saturate at a lower pump power than the lower-order phonon lines (higher energy states). This trend is consistent for all emission lines in QE3, as shown in Fig. 3.8. The saturation behaviors can be attributed to the lifetime-limited excited state, considering the nature of the localized quantum emitters [123, 124].

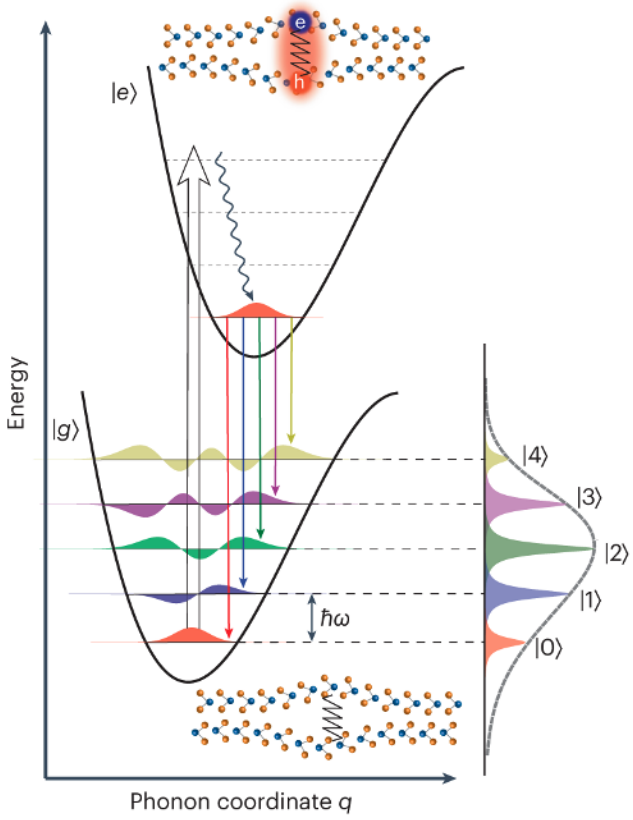

Figure 3.9: A diagram of the Franck-Condon model of exciton-phonon coupling in a 2D QE. The lower parabolic potential represents the ground-state PES of the QE. Multiple phonon states with an energy spacing of 3.4 meV are shown, with their wavefunctions illustrated. The upper potential represents the excited-state PES of the QE with optically pumped IX. The phonon mode that strongly couples with the IX is the BM, in which the layers of WSe_2 move in opposite directions, modulating the interlayer spacing and IX energy. Based on the Huang–Rhys theory, the phonon line intensity should have a Poisson distribution with an average phonon number at S, which is the Huang–Rhys factor. The anharmonic effect can result in unequal energy spacing for the adjacent phonon lines.

3.5 Tunable phononic coupling

3.5.1 Franck-Condon model

The observation of multiple well-resolved emission lines can be explained as phonon replicas due to the coupling between a single IX and a single-phonon mode that are colocalized in the QE. Their coupling can be understood with the Franck-Condon principle, as illustrated in Fig. 3.9 [102, 103, 122, 125]. The ground state of the QE and its excited state when an IX is generated can be modeled with two potential energy surfaces (PESs). Each PES is populated with phonon states that are not evenly spaced because of the anharmonicity of the PES. Under the linear coupling approximation, the phonon-exciton coupling is represented by a shifted equilibrium position of the excited-state PES relative to the ground state. At low temperatures, the QE at the ground-state PES has nearly zero phonon occupancy. When an exciton is created by the pump laser, the QE is excited into a higher-energy PES and quickly relaxes to its zero phonon level. Upon exciton recombination, the QE emits a single photon and relaxes to its ground-state PES but at an elevated phonon state, as illustrated in Fig. 3.9. As a result, the energy of the emitted photon is Stokes-shifted from the zero-phonon line, forming phonon replicas spaced by the phonon energy. In Fig. 3.9, the emission lines are labeled with the corresponding phonon number state $|n\rangle$ in the ground-state PES. According to the Huang-Rhys theory for discrete phonon lines, the intensity of the nth phonon line is proportional to the overlap integral between the initial and final phonon states, that is, $|\langle 0|n\rangle|^2 = e^{-S}S^n/n!$, where S is the dimensionless Huang-Rhys factor measuring the strength of the exciton-phonon coupling. Therefore, the phonon line intensities have a Poisson distribution with an expectation value of S, as illustrated in Fig. 3.9. In many other solid-state QEs, such as the color centers in diamond, the coupling of defect emitters to bulk phonons produces phonon sidebands that are not well resolved due to the continuous phonon density of states in energy. In contrast, in Fig. 3.7a,b, we observe clearly resolved

phonon lines generated by a single localized phonon mode that couples with a single IX in the QE.

3.5.2 Breathing mode phonon

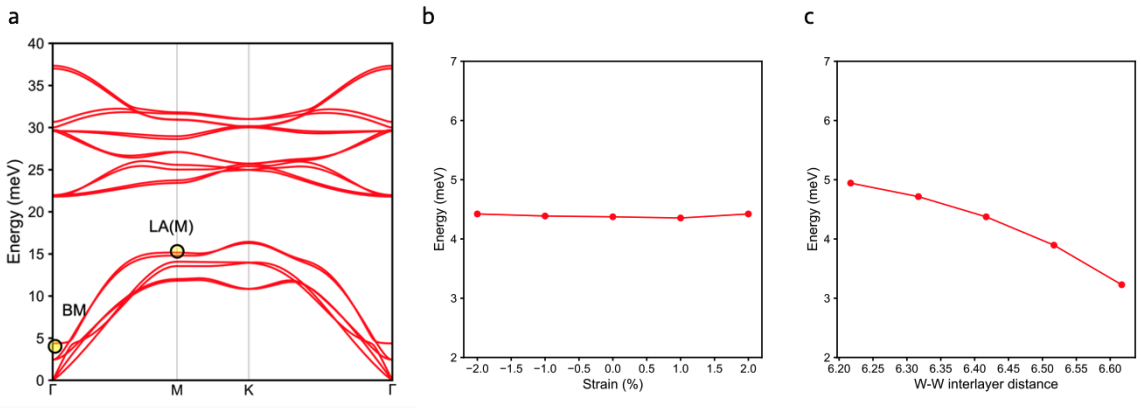

Figure 3.10: Phonon properties in bilayer WSe_2. a) Phonon dispersion of intrinsic bilayer WSe_2. b) BM phonon energy dependence on in-plane strain. c) BM phonon energy dependence on the W-W interlayer distance. The equilibrium distance is 6.417 Å.

The phonon dispersion for intrinsic bilayer WSe_2 is shown in Fig. 3.10a. In addition to the phonon modes typically found in monolayer WSe_2 such as the longitudinal acoustic mode at the M-point in the Brillouin zone (LA(M) mode) in which the atoms collectively move in the same direction longitudinally, there are also phonon modes that appear only in 2D heterostructures with at least two layers. Specifically, the breathing mode (BM) phonons in bilayer WSe_2 arise from the atoms in the individual layers moving in opposite directions in the out-of-plane axis, in a breathing-like motion, as in the inset of Fig. 3.9.

The energy spacing of the phonon lines in the range of 3.0-5.0 meV matches the energy of the BM phonons in bilayer WSe_2. Time-resolved transmission measurements

in pristine bilayer WSe_2 give the frequency and the coherence time of the BM phonon as 0.8 THz (or 3.4 meV) and 3.5 ps, respectively [104]. However, the interaction between the WSe_2 and the encapsulating hBN can cause mode hybridization that modulates the frequency of the BM phonon [126]. Additionally, the strong local strain gradient and the quantum confinement also affect the BM phonon frequency.

The local strain induced by nanopillars not only creates local potential wells to trap IXs, but also strongly modulates the interlayer phonon modes, causing an energy shift of the breathing mode (BM) phonon. Without knowing the detailed local strain, however, it is not possible to directly compute the strain caused by nanopillars and the corresponding phonon energies. Instead, we choose different interlayer distances and lattice constants for the unit cell of bilayer WSe_2 and then calculate the BM phonon energies using the first-principles density-functional perturbation theory. Fig. 3.10b shows the BM phonon energy variations under different in-plane strains. Fig. 3.10c shows the BM phonon energies at different interlayer distances around the equilibrium interlayer distance. It can be seen that the BM phonon energy weakly depends on the in-plane strain but strongly depends on the interlayer distance. It indicates that the out-of-plane strain due to nanopillars can significantly modulate the BM phonon energy. The BM phonon couples strongly with the IXs by directly modulating the interlayer distance, generating the pronounced phonon lines. The calculated energy variation range of the BM phonon is consistent with the energy spacing range as in Supplementary Table D.3 and Supplementary Fig. D.5.

3.5.3 Huang-Rhys parameter fitting

The Huang-Rhys parameter S is determined by fitting the series of phonon peaks with Lorentz functions and extracting the amplitude of each peak. Those peak amplitudes follow the Poisson function according to the Huang-Rhys theory:

$$f(n, S) = e^{-S} S^n / n! \tag{3.1}$$

where n is the number of phonons [127]. The highest observable energy peak was assigned with the lowest phonon number n_0, the second-highest energy peak was assigned $n_0 + 1$, and so on. The peak intensities were then fit with the above Poisson function with n_0 and S as free parameters with an upper limit of n_0=3. Once n_0 was determined for a given QE, it was fixed, and the peak amplitudes were fit with a Poisson distribution to determine S.

In Fig. 3.11, with additional data points shown in Supplementary Fig. D.5, the fitting results of several QEs are shown with the black stars. To be identified as one of these phonon states, the peaks must behave the same with voltage modulation (i.e., tuning at the same rate, appearing at the same voltage), and have the same linear polarization. As listed in Supplementary Table D.3, the calculated S ranges between $1.0 - 6.0$. However, the Poisson fitting is not ideal, with a large error. The reason is that the phonon lines are not evenly spaced, and the amplitudes deviate from the ideal Poisson distribution. This discrepancy is caused by the approximate treatment of exciton-phonon coupling in the Huang-Rhys theory, including approximating the exciton states as harmonic oscillators and assuming linear coupling between the exciton and phonon states. The interplay of the excitonic band structures of WSe_2 and local strain due to the nanopillar and breathing phonon modes further complicates the problem. Nevertheless, the analysis qualitatively determines the S value, showing a clear trend when it is tuned by the gate voltage, as seen in Fig. 3.12b.

The phonon line spacings of the emitters in Fig. 3.11 and Supplementary Fig. D.5 are in the range of 3.0 to 8.0 meV. This variation of phonon energy can be attributed to several reasons. First, as discussed, there are three interlayer breathing modes for TMDs encapsulated with hBN due to the interface phonon mode hybridization [104, 126]. Second, as shown by the phonon band calculations in Fig. 3.10a, the strain induced by the nanopillar will modulate interlayer separation of the bilayer WSe_2, resulting in a shift of the breathing mode energy, as shown in Fig. 3.10c. The calculation results support that these energy spacings are well within the range

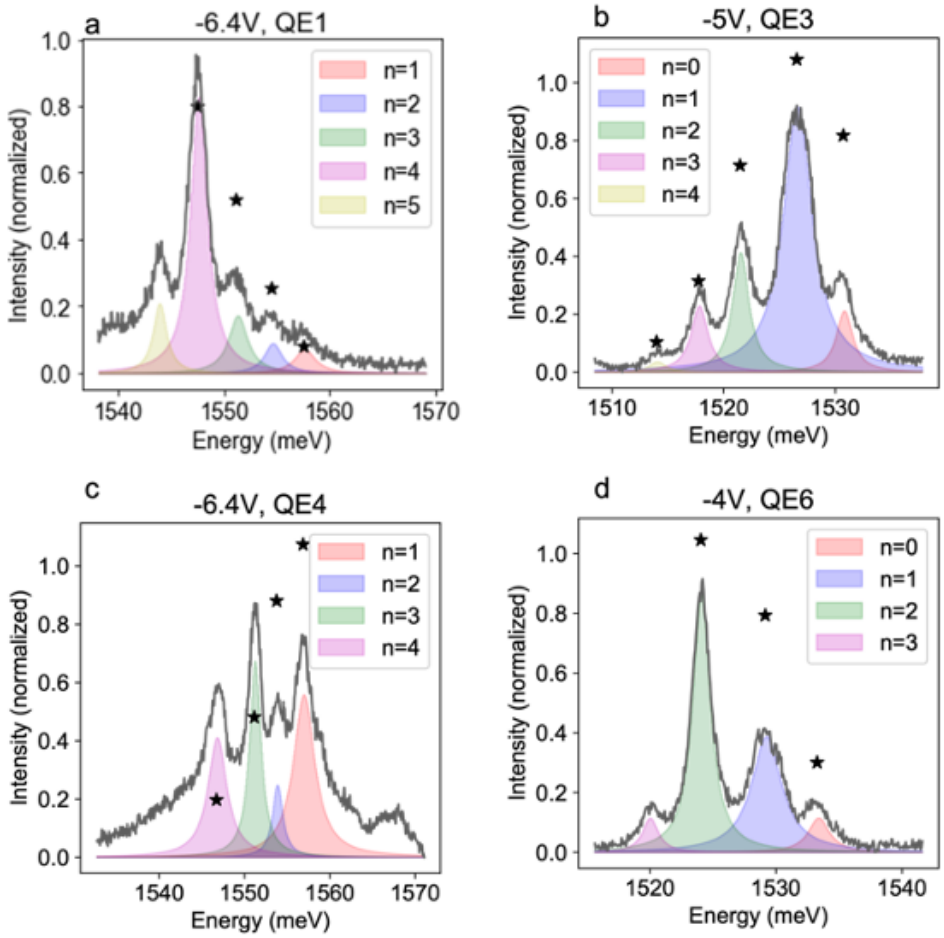

Figure 3.11: The phonon lines in IX QEs coupled to interlayer breathing mode phonons. Each peak is fit with a Lorentzian function shown as shaded areas. The amplitude of each peak was fit with a Poisson function to extract the Huang-Rhys parameter, shown as black stars.

expected from theory.

To extract the Huang-Rhys S parameters, the PL spectrum was first normalized and then fit with between 3 to 6 Lorentzian functions, depending on how many

pronounced peaks were present. From these Lorentzian fittings, the central energy of each phonon line was extracted, and this value was used to retrieve the intensity of each peak. The error in the Lorentzian fittings was very small, so it did not contribute to the overall error to the value of S. Using the peak intensities, the least-squares fit (SciPy) was used on a Poisson distribution to find the optimal S, given these peak intensities. Because of the approximations we made, there was a substantial error from this fitting, determined from the diagonal elements of the covariance matrix corresponding to S. The other source of error in S would come from the signal-to-noise ratio of the PL spectrum itself, which varies from sample to sample, and even voltage step to voltage step, depending on how strong a given peak is. To account for this, the root-mean-square error (RMSE) resulting from the noise in the PL was determined for each emitter at each voltage step. To determine the upper bound of the error this would cause, the Poisson fitting was done with the peak intensities $\pm$ RMSE, and the difference in S was taken. Because the RMSE was so small in comparison to the error in the fitting, even for the data with the highest RMSE, this resulted only in very small errors in S (~ 0.01). The dominant error in S, therefore, stemmed from the fitting itself.

3.5.4 Tunability of exciton-phonon coupling

Fig. 3.12a shows the PL spectra of QE1 with increasingly negative gate voltage and a fixed pump power of 15 μW. In addition to a consistent redshift of the phonon lines, their intensity distributions change substantially, indicating the modulation of the phonon coupling strength S. We extract the S factors by fitting the peak intensities with the Poisson distribution [103]. Because the PES of the QEs is more complicated than the simple harmonic oscillator model assumed in the Huang-Rhys theory, the fitting has a large error, which outweighs the signal's noise, so it can only estimate the S factors. Despite the relatively large fitting errors, the result of S versus gate voltage in Fig. 3.12b clearly shows that S initially increases with the gate voltage,

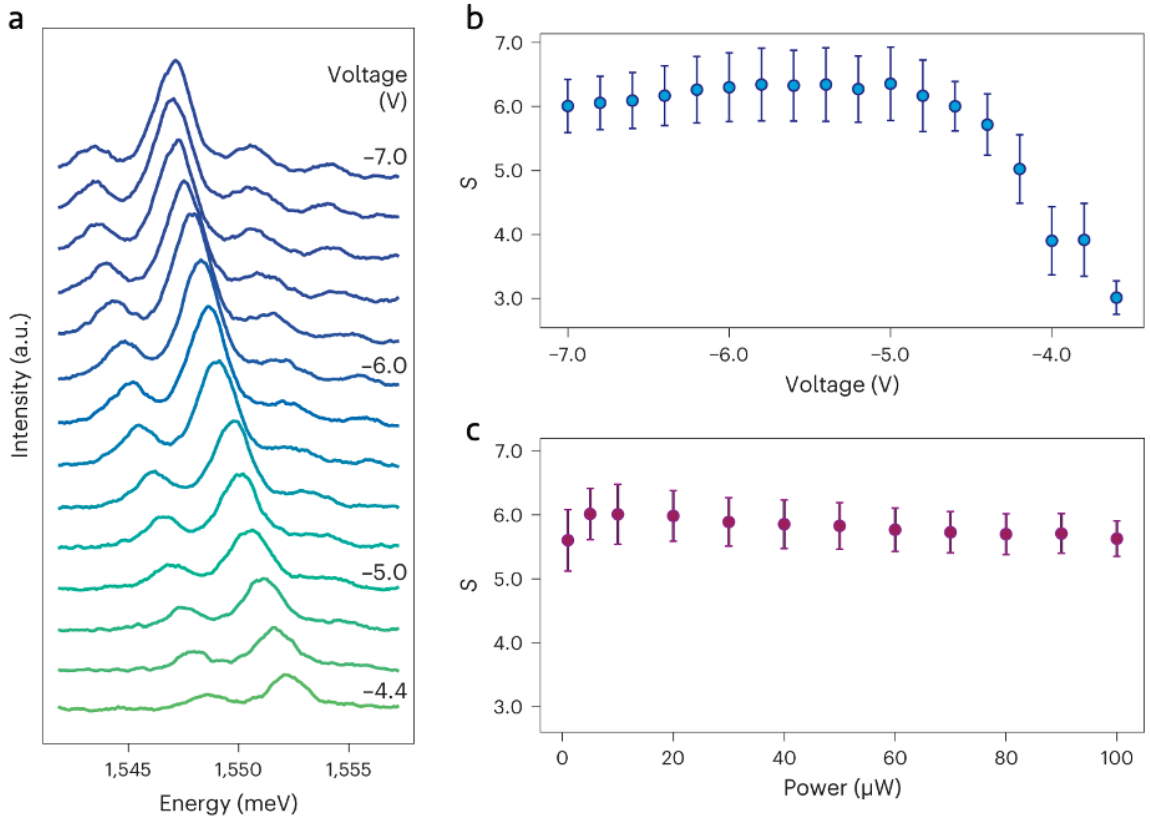

Figure 3.12: S tuning with voltage. a) PL spectra of QE1 at different gate voltages. The intensity distribution of the phonon lines is strongly modulated by the gate voltage. We extract the value of S by fitting the intensity with the Poisson distribution. b) S as a function of the gate voltage. S initially increases with the voltage, in agreement with theory, and levels off after -5.0 V. c) S as a function of pump power. The error bars in (b) and (c) represent the standard error in the least-squares fit to the Poisson distribution for $n = 450$.

reaching a maximal value of 6.3 at ∼-5 V, and saturates thereafter. Although the coupling strength g_0 is proportional to the effective field across the materials, the dependence of S on the field is indirect and cannot be ascribed to a simple linear dependence. In particular, when the phonon coupling is large, the dependence of S

on the coupling strength and electric field will involve the detailed change of the PES in response to the electric field. The saturation is possibly due to gate leakage and charge screening, which prevent further increase of the electric field, as also observable in the emission energy tuning in Fig. 3.7e and f. For comparison, we also measured S with increasing pump power and a fixed gate voltage of -6.4 V. S for the most part is unaffected by the pump power. Our results show that the coupling between the colocalized quantum phonon mode and a single exciton can be precisely tuned by an electric field to a large value.

3.5.5 Estimation of coupling strength

The colocalization of the IX and the BM phonon in the strain-engineered QE results in a very large coupling between them. The single exciton–phonon coupling can be described with the spin–boson interaction Hamiltonian:

$$H_{int,\nu} = g_0 \sigma_z (b^\dagger + b) \tag{3.2}$$

where $b(b^\dagger)$ is the phonon annihilation (creation) operator on phonon number states $|n\rangle$, σ_z is the Pauli matrix on the basis of the ground $|g\rangle$ and excited $|e\rangle$ states of the exciton, and g_0 is the single exciton-phonon coupling rate [88, 128]. The BM phonon directly modulates the dipole moment of the IX by adjusting the interlayer distance. Under an electric field E, the single-phonon-IX coupling rate can be calculated from the zero-point amplitude $\overline{x}_{zpf}$ of the Γ-point BM:

$$g_0 = g^0 + 2eE\overline{x}_{zpf}. \tag{3.3}$$

where $\overline{x}_{zpf}$ is calculated from first-principles theory to be ~ 0.026 Å.

g^0 is the zero-field coupling rate, which is calculated to be < 0.08 meV, as shown in Fig. 3.13, which is one order of magnitude smaller than the second term when the field is strong. Thus, assuming that the applied field can reach a reasonably high value of 0.24 V/nm in our device ([66]), g_0 can be increased to 1.3 meV. The system

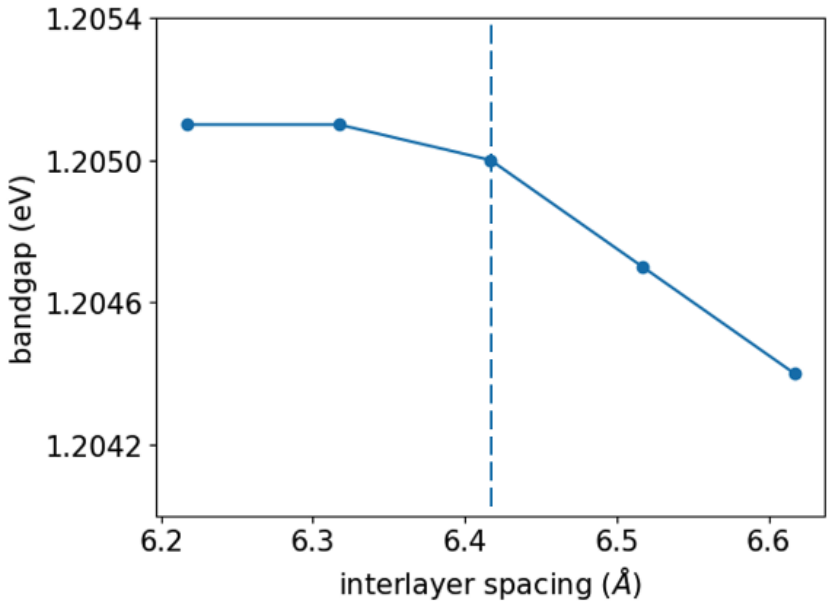

Figure 3.13: DFT calculation of bandgap at different interlayer spacing. The dashed line indicates the equilibrium position of interlayer spacing for bilayer WSe_2. The change of the bandgap energy in response to the change of the interlayer distance of bilayer WSe_2 is insignificant. The corresponding zero-field coupling rate is < 0.08 meV.

thus can reach the strong-coupling regime, satisfying $2g_0 > (\gamma_e, \gamma_p)$, where $\gamma_e \approx 1.17$ meV is the exciton linewidth (Fig. 3.5b) and $\gamma_p < 1.18$ meV is the BM phonon decoherence rate given its coherence time of 3.5 ps measured at room temperature [104]. At cryogenic temperatures and with better sample quality, we expect γ_e and γ_p can be further reduced.

3.5.6 IX QEs coupling to other phonon modes

Fig. 3.14 shows PL spectra from QE7, which is an interlayer QE that has phonon lines with energy spacing in the range of 10.0-16.0 meV, much larger than the BM

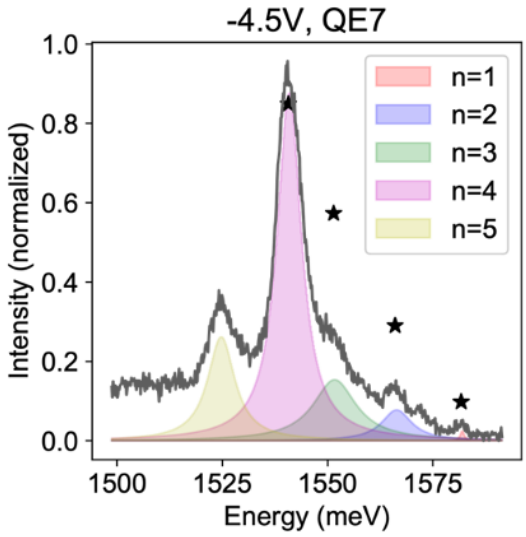

Figure 3.14: The phonon lines observed in interlayer QE7 with larger energy spacing than the BM phonon mode. Each peak is fit with a Lorentzian function shown as shaded areas. The amplitude of each peak was fit with a Poisson function to extract the Huang-Rhys parameter, shown as black stars.

phonon energy. We attribute these phonon lines to other lattice phonon modes, such as the LA(M) phonon (Fig. 3.10), which has an energy of 15.3 meV in pristine bilayer WSe_2 [104]. Typically, LA(M) phonons are only observed in Raman measurements of monolayer WSe_2 because they require inelastic scattering processes at structural defects or along the edges of the flake. However, our emitters are created by a combination of localized strain and defects under a large tensile strain. The modified band structure increases the strength of the LA(M) phonon, and in certain cases, allows it to couple to IXs. Nevertheless, the LA(M) phonon lines are much less frequently observed than the BM phonon lines.

Because of the much higher energy of the LA(M) than the BM phonons, it would follow that the anharmonic effects are more apparent when excitons are coupled to

them, which could explain the large variation of phonon line spacings as listed in Supplementary Table D.4. Another possible explanation is that the IXs couple to the hybridized modes of different phonon modes with varying energies.

3.5.7 Intralayer QEs coupling to phonon modes

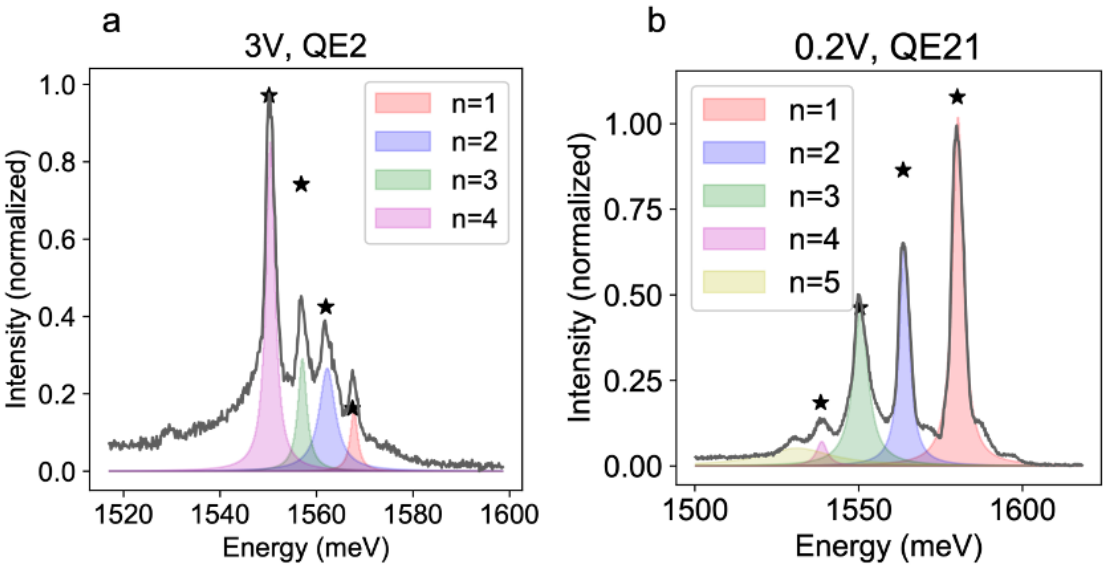

Figure 3.15: The phonon lines of intralayer exciton in QEs. Each peak is fit with a Lorentz function shown in dashed colored lines, and the intensity of each peak was fit with a Poisson function to extract the Huang-Rhys parameter, shown in black stars.

In rare cases, we also observed phonon lines in QEs with only intralayer exciton emission, which is shown in Fig. 3.15. The coupling between the lattice phonon and the intralayer exciton is not expected to happen in pristine bilayer WSe_2. But the local strain effect, materials defects, and the local charging effect may enable the coupling between intralayer exciton and lattice phonon modes, such as the shear mode and LA(M) modes. The details of these modes can be seen in Supplementary Table D.5.

3.6 Device fabrication and characterization

3.6.1 Device fabrication

A 17 × 17 array of nanopillars, each with a diameter of 140 nm, a height of 200 nm and spaced with a 2.5 μm pitch, were patterned on 300 nm SiO_2 deposited by electron-beam evaporation using electron-beam lithography. The 2D material heterostructure consists of bilayer WSe_2 encapsulated by hBN around 30 nm thick with few-layer graphite as top- and bottom-gate electrodes. In some devices, an additional graphite layer is transferred in contact with the WSe_2 to control the doping of the material. The heterostructure is stacked and transferred onto the nanopillar array by a conventional dry transfer method using polycarbonate/polydimethylsiloxane (Sylgard 184) stamps. After the device has been transferred, contact electrodes of Ti/Au to the graphite were patterned with photolithography using a direct laser writer and deposition using electron-beam evaporation. An optical image of a device is shown in Fig. 3.5d, where the strain induced by the nanopillars is visible.

3.6.2 Photoluminescence measurements

The sample was wire bonded to a sample holder and loaded into a cryostat (Montana Cryostation S-100) to be cooled to 10 K for measurement. A leakage test was done to ensure that the electrodes are not shorted together, and then the PL spectra of strained heterostructure can be measured at different bias voltages. A continuous-wave helium–neon laser (632.8 nm) was used to excite the excitons. The laser beam was focused on the sample through an optical window in the cryostat with a 50× objective lens (numerical aperture, 0.55) to achieve a diffraction-limited spot size of about 1 μm in diameter. The IX emission was passed through a 633 nm notch filter to remove the reflected signal of the laser before being acquired with a spectrometer (Princeton Instruments, IsoPlane 320). A diagram of these measurements can be seen in Fig. 3.16.

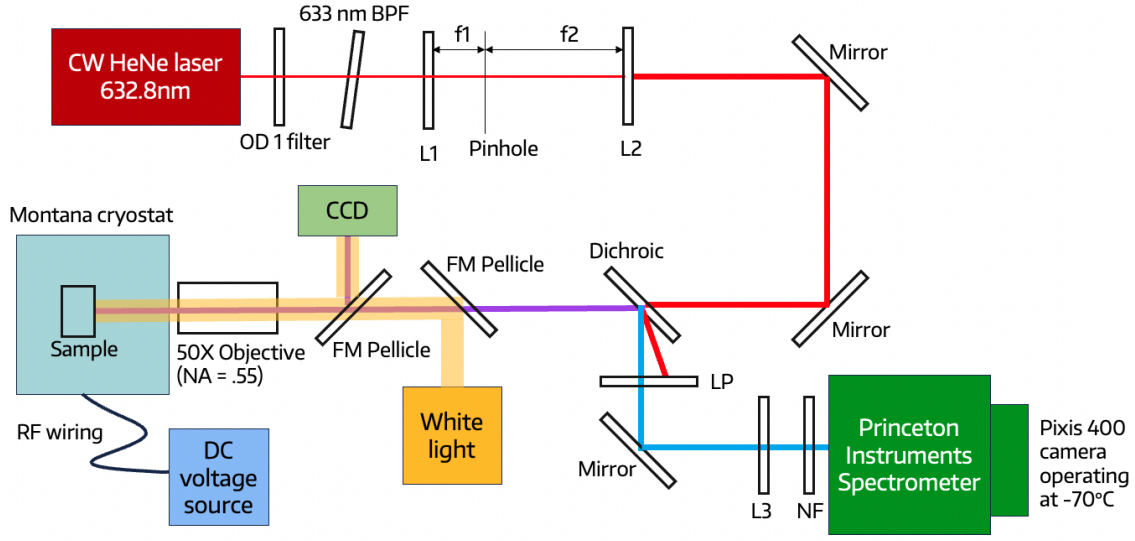

Figure 3.16: The PL measurement scheme for the quantum emitters.

3.6.3 $g^2(0)$ measurements

To confirm that the QEs emit single photons, we performed measurements of the second-order correlation function $g^{(2)}(0)$ using a pair of single-photon Si avalanche photodetectors (SPADs) and a Time-Correlated Single-Photon Counting (TCSPC) module. A tunable bandpass filter was used to select the signal within the frequency range highlighted in red on the left of Fig. 3.18. The filtered signal was then split with a beam splitter and coupled to the two SPAPDs, which were connected to the TCSPC, as shown in Fig. 3.17. The $g^{(2)}(0)$ was plotted as a function of the time lag between triggering events of the two SPADs [7, 83, 116]. We have measured similar antibunching results from many QEs with linewidths in the range of 1-3 meV across different devices (Supplementary Fig. D.4).

The results in Fig. 3.18 and Supplementary Fig. D.4 clearly show the characteristic dip of $g^{(2)}(0)$ at zero delay, with $g^{(2)}(0) < 0.5$ signaling the non-classical anti-bunching behavior. The data in black was fit (red line) with the function $g^{(2)}(\tau) = 1 - \alpha \cdot e^{-\tau/T}$,

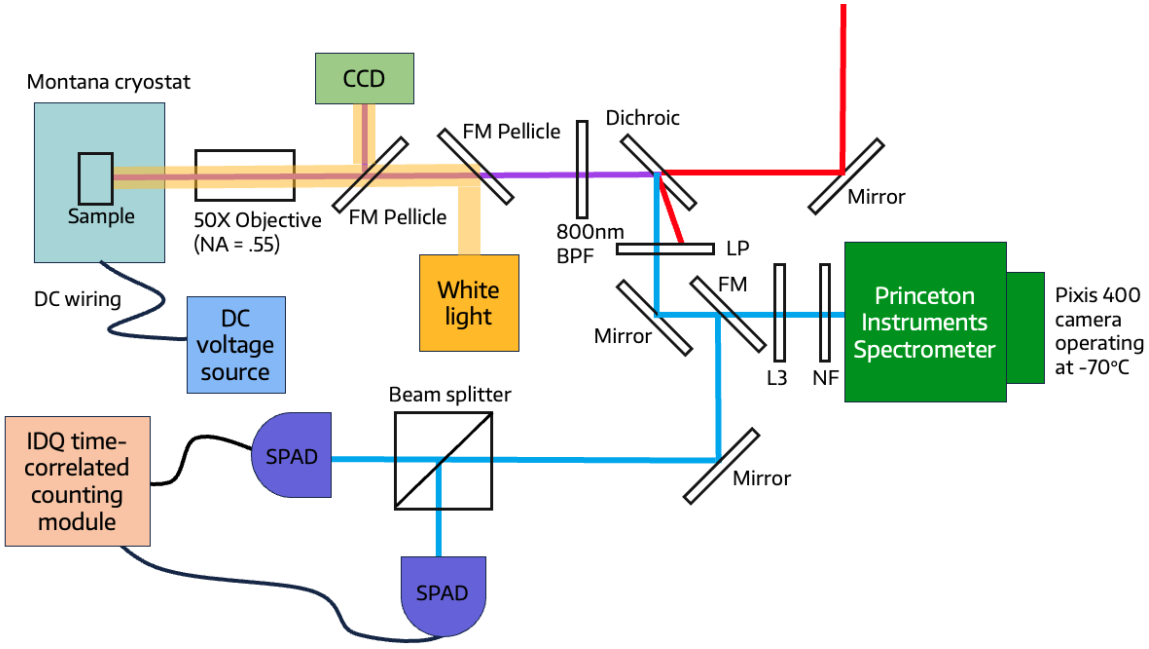

Figure 3.17: The measurement scheme for $g^{(2)}(0)$, intercepting the PL from the spectrometer and redirecting it towards two SPADs which are connected to a TCSPC.

where τ is the time delay between photon detection events, and T is the lifetime of the exciton. $\alpha = \mathrm{SBR}^2/(1+\mathrm{SBR})^2$ is the normalization factor, where SBR is the signal-to-background ratio [7, 87]. With this fit, we can extract the values of $g^{(2)}(0)$, as well as the exciton lifetime T.

From all the 2D QEs we have measured, we found that the linewidth of PL peaks correlates well with whether an emitter is a single-photon emitter and whether the emitter is intralayer or interlayer. In Fig. 3.18 and Supplementary Fig. D.4, we found single photon emitting QEs all have a linewidth less than 2.0 meV (e.g., 0.96 meV for QE13), which is significantly narrower than that of free excitons in bilayer WSe_2, which is $>$ 10 meV [79, 75]. Therefore, we can consider a linewidth of 3.0 meV as the upper bound for single-photon emitters in our samples. Furthermore, in Fig. 3.18 and Supplementary Fig. D.4, we note that the filter passband includes

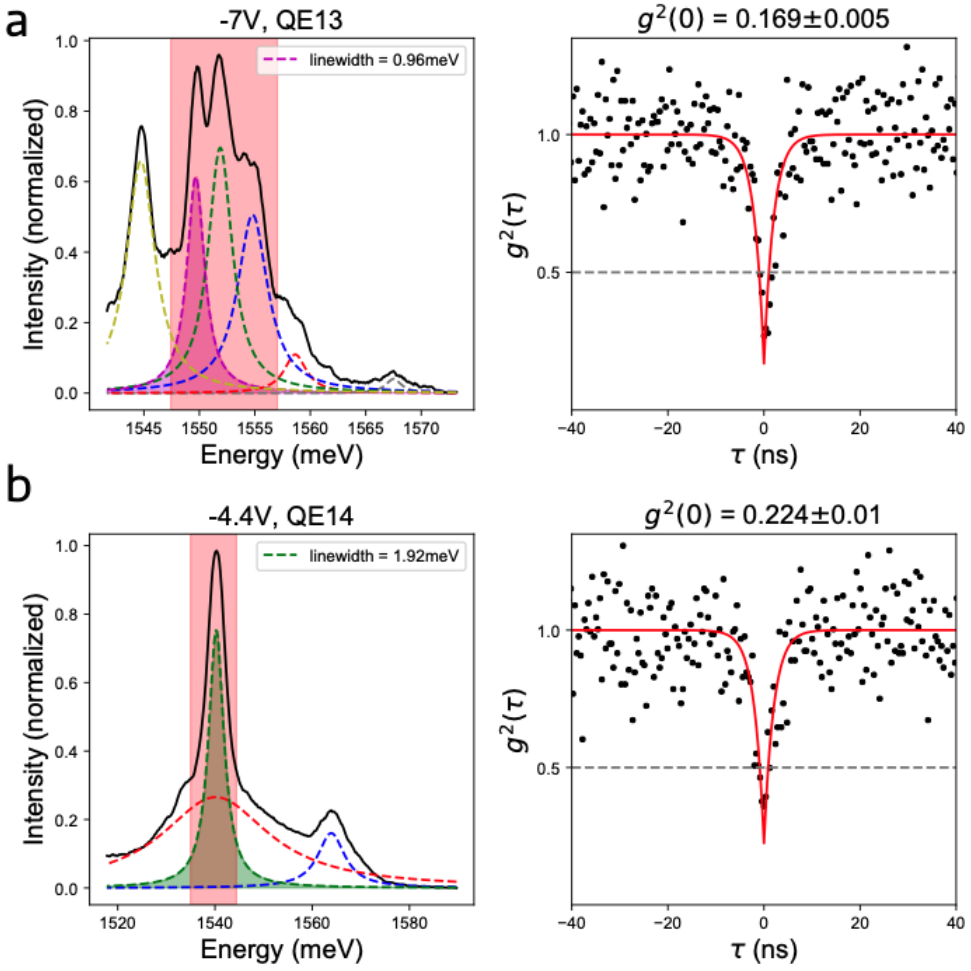

Figure 3.18: PL and corresponding $g^{(2)}(0)$ measurements of a) QE13 and b) QE14. The left panels show the PL of the emitter, with the peaks fit with Lorentz functions. The region highlighted in red corresponds to the PL that passes through the notch filter to the SPADs. On the right panel, the $g^{(2)}(0)$ measurements (black) and the fit (red) are shown.

multiple overlapping phonon lines, yet still has $g^{(2)}(0) < 0.5$ in the interlayer QE emitters (QE13 to 16). This further supports our conclusion that the set of multiple emission lines originates from phonon coupling to a single QE, and that these series

of peaks each act as one single photon source.

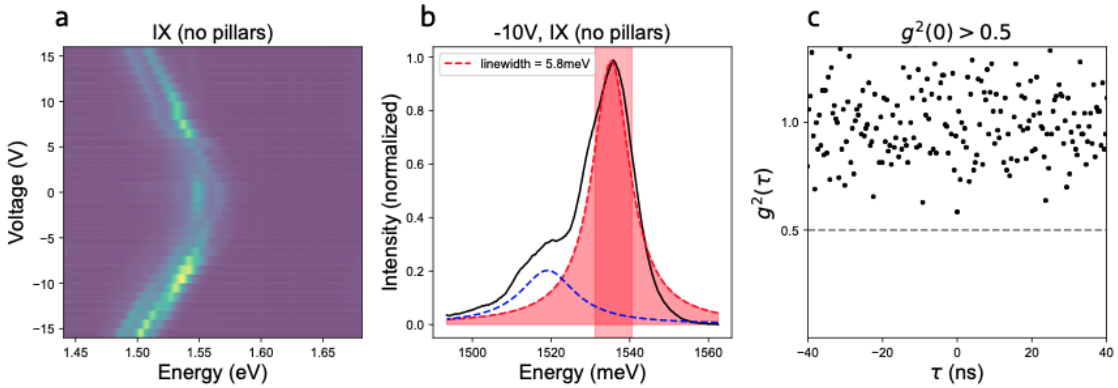

Figure 3.19: Broadband emission from IX in bilayer WSe_2 with no strain. a) The tunability of broadband IX with out-of-plane voltage. b) PL of the broadband IX at -10 V. The IX emission is fit with Lorentz functions, shown with dotted lines. The spectra region that passes through the notch filter and is sent to the SPADs is highlighted in red. c) The corresponding $g^{(2)}(0)$ measurement for the highlighted region in (b).

An unstrained WSe_2 flake was also characterized as a control device, using the same procedure as the quantum emitters. In Fig. 3.19a, we see that the IX emission energy is tunable with gate voltage, but do not display key properties that the quantum emitters have. Namely, the excitons are bright at 0V, have a broad linewidth as shown in Fig. 3.19b, and do not have $g^{(2)}(0) < 0.5$ to be classified as a single photon emitter, as shown in Fig. 3.19c.

3.7 Conclusion

3.7.1 Discussion

We have created highly tunable QEs in WSe_2 bilayers by strain-engineering methods. An immediate next step is to integrate these emitters with integrated photonic

platforms such as waveguides and photonic crystal cavities to achieve super-radiant emission, Purcell enhancement, and cavity quantum electrodynamics. With twisted bilayer WSe_2, rather than a natural bilayer, the IX energy can be tuned electrically while still maintaining the characteristic valley states similar to those reported in moiré systems [109, 110, 129]. Furthermore, the demonstrated tunable phonon-photon coupling strength in these 2D QEs provides a new way to explore the quantum optomechanical effects. In many ways, the 2D QEs are analogous to cavity optomechanical systems, but at the atomic interface and with a phonon frequency of 0.8-1.0 THz, which is already at the ground state at the measurement temperature of 10 K. It will be possible to use a terahertz source to resonantly excite the phonon and prepare phonon Fock states in such a solid-state system at temperatures that are among the highest reported. The archetypical excitonic-optomechanical system demonstrated here thus has the potential to be a new quantum light resource that is entangled with single phonons [89, 91] for use in quantum information processing, storage, and communication [88, 130, 131, 132].

3.7.2 Future work

Building on these results, several avenues of future work can be pursued. First, integrating these strain-engineered WSe_2 quantum emitters with on-chip photonic structures, such as waveguides or photonic crystal cavities, could enable Purcell-enhanced emission, directional coupling, and the realization of cavity quantum electrodynamics with tunable phonon sidebands. Additionally, by replacing natural bilayers with twisted bilayer WSe_2, it may be possible to exploit moiré-induced exciton superlattices for even larger electrical tunability and access to valley-specific quantum states.

The demonstrated tunable exciton–phonon coupling also opens the door to exploring quantum optomechanical phenomena at the atomic scale. For example, using ultrafast terahertz excitation to drive the breathing mode phonon could enable the preparation and manipulation of phonon Fock states. Arrays of such emitters, coupled

through shared phononic or photonic modes, could serve as a platform for studying phonon-mediated entanglement and quantum transduction. Finally, improving material quality through controlled defect engineering and optimizing the heterostructure interfaces will be crucial steps toward achieving indistinguishable, room-temperature-operable single-photon sources with engineered phonon interactions, advancing their application in scalable quantum information processing and communication technologies.

Chapter 4

EXCITONIC CONTROL VIA SURFACE ACOUSTIC WAVE RESONATORS

4.1 Background

4.1.1 Motivation for our work

In Chapter 2, we demonstrated methods for transporting excitons via SAWs, and in Chapter 3, we demonstrated the deterministic creation of localized and highly tunable quantum emitters. Both of these afford us tunability and control over excitons; however, we still desire a method for encoding and reading out information either localized to an emitter or within the free excitons across a 2D heterostructure.

Various degrees of information within 2D heterostructures have been proposed as a promising platform for information storage, including the electronic valley in some excitons [10], spin waves in magnons [133, 20], carrier density [17], Raman modes [18], and more. Because 2D materials have such strong light-matter interaction, exciton lifetimes are long at low temperatures, and can even survive at room temperature. Furthermore, the reduced dimensionality of the system enables precise control and programming of these information degrees, making them appealing not only for information processing but also for encoding and storage.

To achieve this, we aim to use a SAW resonator to dynamically modulate a 2D heterostructure. As discussed in previous chapters, 2D heterostructures are exceptionally sensitive to external perturbations such as electric fields, magnetic fields, and strain, making them highly tunable platforms. SAW resonators are particularly well suited for this purpose. They provide a non-invasive means of applying both strain and electric fields without requiring patterned electrodes directly on the heterostruc-

ture, thereby minimizing disorder and preserving material quality. Moreover, their operation in the MHz–GHz regime enables high-speed modulation, allowing us to interact with carriers and excitons on time scales comparable to their intrinsic lifetimes. This allows for real-time, dynamic control over the band structure and related electronic or optical properties.

The goal of this work is to demonstrate SAW resonators as a promising platform for enabling coherent interactions with various quasiparticles intrinsic to 2D heterostructures, including excitons, magnons, phonons, and more. As a first step, we focus on a proof-of-concept design aimed at achieving dynamic and deterministic tuning of excitonic behavior. Specifically, we investigate whether a SAW resonator can be used to dynamically program excitonic properties such as energy and linewidth. Since it is well established that exciton energies shift under static in-plane strain [18], we expect that by time-averaging over the SAW period at an anti-node, the exciton energy will oscillate back and forth, resulting in an effective linewidth broadening, while remaining unchanged at the nodes.

We are also interested in exploring whether the SAW resonator can influence the spatial distribution of exciton density. In particular, we aim to see if exciton intensity is enhanced at the anti-nodes, possibly due to the SAW driving excitons from the nodes toward the anti-nodes on the relevant timescales. Given that we have previously demonstrated SAW-driven exciton transport when excitons become trapped at the low potential point of the SAW [29], it is plausible that bidirectional transport could lead to increased exciton accumulation at the anti-nodes and suppression at the nodes. Additionally, we seek to determine whether these effects can be controlled spatially by selectively pumping different cavity nodes, providing a route to programmable exciton landscapes.

4.1.2 Previous work

Many previous studies have explored methods for patterning 2D materials, with much of the work focused on techniques that permanently modify the heterostructure to spatially tailor its fundamental properties. For example, [134, 135] demonstrated laser thinning of graphite, producing localized Raman shifts in the thinned regions. Similarly, [136, 135] achieved spatial doping of monolayer MoS_2 with phosphorus and created sulfur vacancies, leading to blue shifts in the photoluminescence spectra and increased exciton densities in the patterned areas. While these methods are highly effective for creating well-defined spatial patterns, they are also invasive and irreversible, permanently altering the material.

In contrast, surface acoustic wave (SAW) resonators provide a tunable, switchable, and dynamic alternative, offering non-invasive, on-demand control over low-dimensional systems. For instance, [137] used standing SAWs to generate periodic electric fields that organized nanowires into controllable patterns, with the spacing tunable by varying the SAW frequency. Likewise, [138] demonstrated that standing acoustic waves could induce alternating stripes of opposite magnetization in a galfenol thin film, enabling a reversible and contactless approach to modulate magnetic domains. These studies underscore the versatility of SAW resonators in structuring and manipulating nanoscale systems through dynamic strain and electric fields.

Beyond these demonstrations of SAWs as dynamic, non-invasive tools for patterning nanowires and controlling magnetic domains, recent studies have further expanded the scope of SAW resonators to interface with a broad range of excitations in low-dimensional systems. In [139], researchers showed that standing SAWs on GaAs substrates can periodically lift WS_2 monolayers from the surface, enhancing and spatially modulating photoluminescence through nanoscale strain-driven detachment. In [140], researchers extended this to the quantum regime by integrating monolayer WSe_2 and multilayer hBN single-photon emitters with high-Q SAW resonators,

achieving dynamic modulation of emission energies and fine-structure splitting via deformation potential coupling. Together, these works highlight the versatility of SAW resonators for dynamically controlling excitons, magnons, phonons, and single-photon states through high-speed, non-invasive, and spatially tunable interactions. Building on this foundation, my work seeks to harness SAW resonators to actively and coherently modulate excitonic properties in 2D heterostructures, paving the way for programmable quantum and optoelectronic functionalities.

4.2 Surface acoustic wave resonators

4.2.1 SAW resonator principles

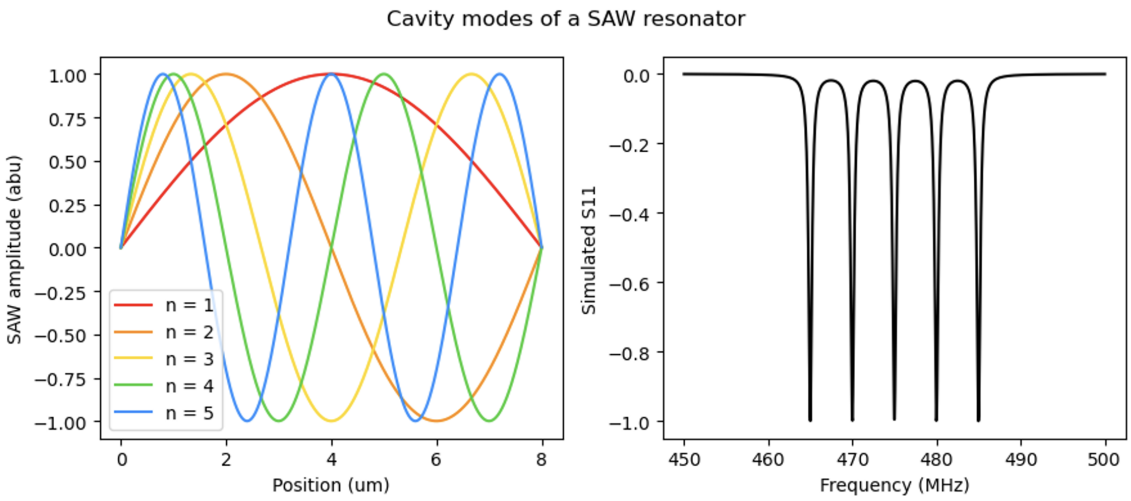

Figure 4.1: Cavity modes of a surface acoustic wave resonator. a) Cavity modes for $n = 1, 2, 3, 4, 5$. b) Simulated S11 for the cavity modes in (a).

Surface acoustic wave resonators are the easiest way to create a standing wave, as outlined in Section 1.4.4 and shown in Fig. 1.11. The resonator can host cavity frequencies when $L_c = n\lambda/2$, where L_c is the effective cavity length and n is an integer. The factor of 2 comes from the wave needing to travel the length of the cavity in each

direction before a standing wave will form. This gives the cavity the ability to host resonances at

$$f_0 = nv_f/2L_c \tag{4.1}$$

with spacings between the resonances given by

$$\frac{\Delta f_n}{f_0} = \frac{f_{n+1} - f_n}{f_0} = \frac{\lambda_0}{2L_c}. \tag{4.2}$$

where λ_0 is the fundamental wavelength of the cavity.

These modes will create different SAW amplitude profiles spatially throughout the cavity, as shown in Fig. 4.1a. These modes will create a series of dips in the S11 corresponding to the resonances, as shown in Fig. 4.1. The spacing between the resonances is given by Eqn. 4.2.

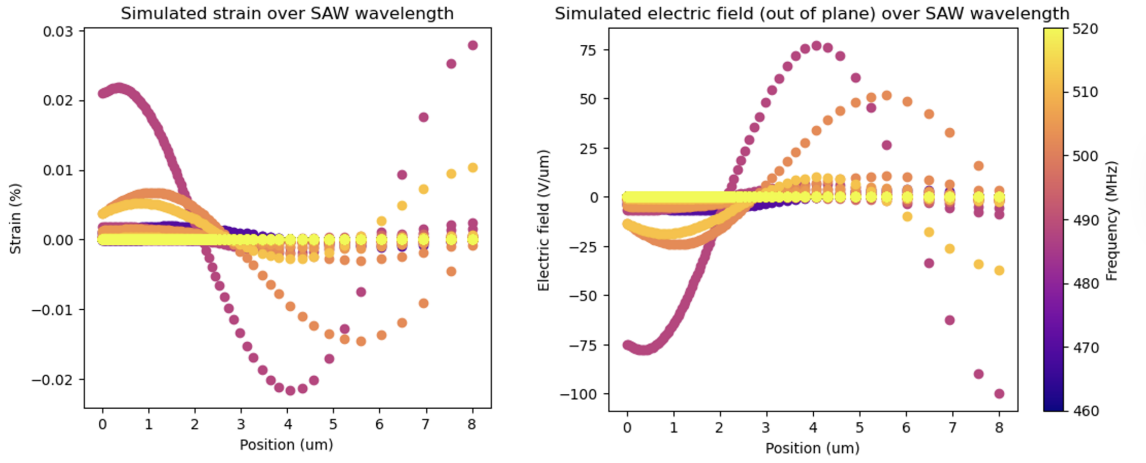

Figure 4.2: COMSOL simulation of cavity modes in a SAW resonator. Percentage of simulated strain (a) and out-of-plane electric field (b) over the SAW wavelength as a function of cavity position, assuming a cavity length of 8 μm.

By doing FTD (finite time domain) COMSOL simulations, we can look at the amplitudes of the strain and electric field waves for these different resonances, as

shown in Fig. 4.2. While the net strain and electric field at any given spot within the cavity will be net zero when time averaged over the SAW period, excitons located at the antinodes of the standing wave will experience strain and electric field over their lifetimes.

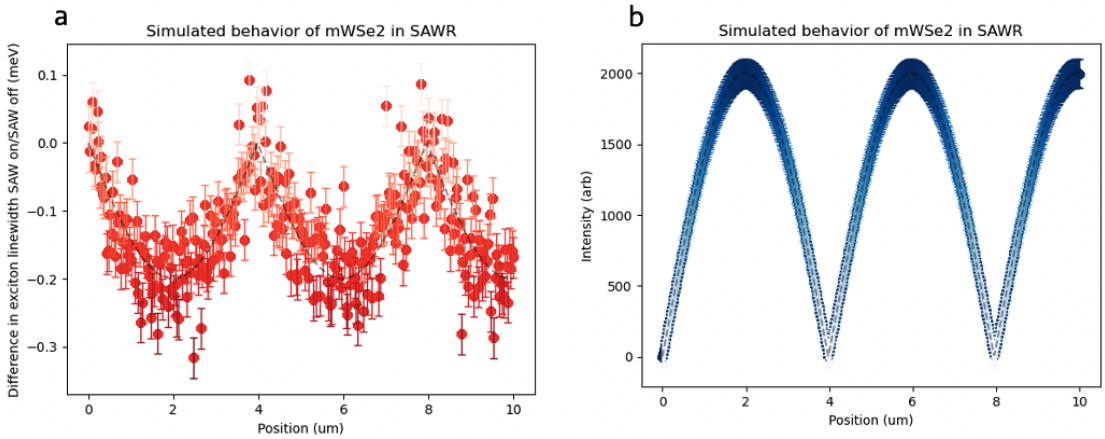

Figure 4.3: Simulated excitonic behavior of monolayer WSe_2 inside a SAW resonator. a) The difference between the exciton PL linewidth with SAW on - SAW off is shown, with broadening expected at the anti-nodes, and no modulation at the nodes. b) The exciton density profile is shown, with intensity enhancement at the antinodes and intensity suppression at the nodes.

For example, take an acoustic wave with a frequency of 500 MHz, corresponding to a period of $\sim$ 2 ns. The lifetime of excitons is highly variable as it is dependent on the exciton species, the temperature of the material, the stacking order of the heterostructure, local strain or defects, external electric fields, and more, but typically ranges from a few nanoseconds to a few tens of nanoseconds. The effects of the SAW period will result in the excitons experiencing net electric and strain fields at the anti-nodes. At these points we expect to see the exciton signal broadening as we time average over several SAW periods and exciton lifetimes, with the exciton energy red

and blue shifting in each direction over the course of the SAW period, as shown in Fig. 4.3a. Comparatively, at the cavity nodes, the strain and electric field will always be zero, so we would expect no change in the exciton PL. This gives us the ability to program the net strain and electric field of specific locations within a cavity by choosing which SAW resonance to drive and with what acoustic power.

Similarly, as we showed in Chapter 2, exciton transport was enabled over long distances when the excitons became trapped in the dynamic potential well created by the traveling surface acoustic wave. The standing wave created by the SAW resonator will similarly have a dynamic potential well at the anti-nodes, and it is possible that this will funnel excitons at the nodes towards the anti-nodes on either side via the same mechanism. This would result in intensity enhancement at the anti-nodes while the intensity would be suppressed at the nodes, creating a controllable pattern of exciton density as shown in Fig. 4.3b.

4.2.2 Design parameters and optimization

We are interested in examining the spatial and frequency effects of a 2D material within a SAW resonator cavity. To achieve this, several design parameters must be considered. The first is that we would like multiple standing wave periods to fit within a single 2D heterostructure, for a typical WSe_2 size of about 10 μm wide by 20 μm long. The standing wave period will be half that of the IDT when the forward- and backward-propagating waves constructively interfere. Our spatial resolution will be diffraction limited, with our laser spot size about 1 μm (NA = .55). Choosing a SAW wavelength of about 8 μm for a standing wave period of about 4 μm strikes a good balance between these two factors, allowing us to theoretically spatially resolve several periods worth of the effects of the SAW standing wave.

We also wish to maximize the quality factor of our cavity to achieve maximum interaction between our standing SAW and 2D heterostructure. The quality factor of the cavity itself is known as the unloaded quality factor and is given by Eq. 1.4, and

is reprinted below:

$$Q_u = \frac{2\pi f_0 L_c}{R_c} = \frac{\pi L_c}{\lambda_0(1-R)} \tag{4.3}$$

where f_0 and λ_0 are the fundamental cavity frequency and wavelength, L_c is the cavity length, R_c is the total resistance of the effective circuit, and R is the total reflectivity of the Bragg reflectors (see Appendix A). From this, we can see that maximizing the fundamental frequency and the cavity length while minimizing the total resistance in the circuit will result in the best quality factor. The phase of the SAW resonator must also match the phase of the IDT, which can be determined experimentally by sweeping the length of the cavity and the location of the IDT within the cavity. Additionally, we want the total reflectivity $R \to 1$, which we can experimentally sweep with the number of fingers in the array and the thickness of the fingers.

We can also account for losses due to the IDT with the loaded quality factor given by:

$$Q_L = \frac{2\pi f_0 L_c}{Z} \tag{4.4}$$

where the total resistance R_c in the unloaded quality factor is replaced with the characteristic impedance of the effective circuit Z. This requires impedance matching to our VNA with 50 Ω impedance, which can be achieved experimentally by sweeping the number of fingers in the IDT.

4.3 Device fabrication and characterization

4.3.1 SAW resonator fabrication

The SAW resonators are fabricated on 128°C Y-cut $LiNbO_3$. After sweeping the design parameters described in the previous section in an effort to optimize the loaded and unloaded quality factor, the winning design was a double finger IDT in the center of a cavity, with a set of Bragg reflectors on either side. The IDT has a designed wavelength of $\lambda_0 = 8$ μm, corresponding to a standing wavelength of 4 μm, and 4.5 SAW periods worth of fingers, with the additional half pair of IDT fingers accounting

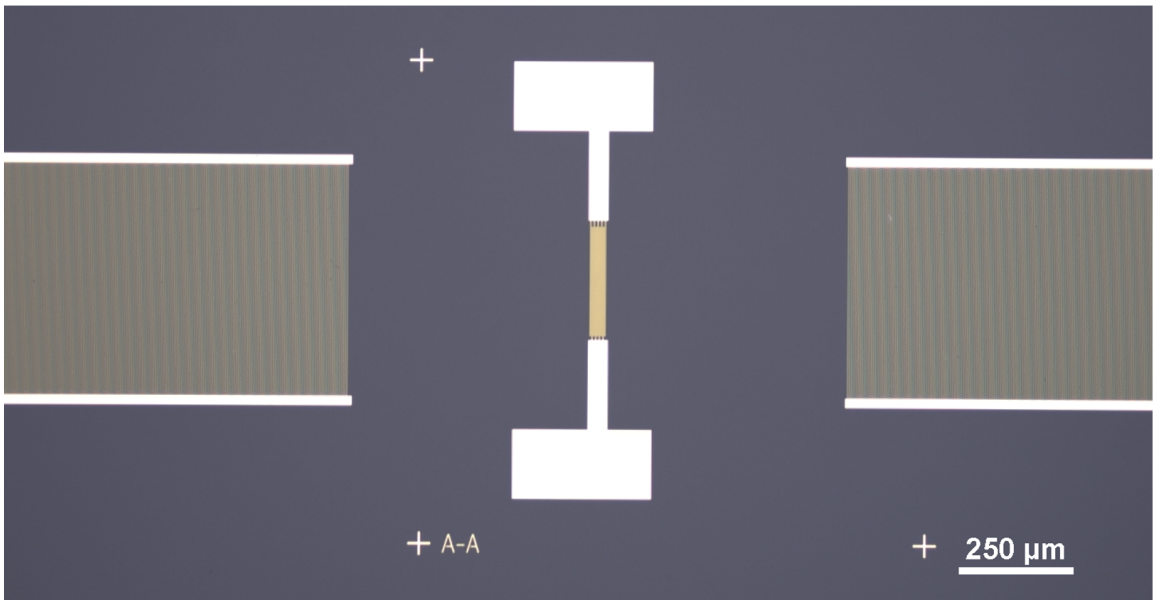

Figure 4.4: An optical image of a fabricated SAW resonator.

for the additional phase the SAW will pick up when it changes direction upon hitting the reflectors. The distance between the two reflector arrays d (measured from center-to-center of the first fingers of the reflector arrays, as shown in Fig. 1.11) is 1090 μm, corresponding to $(136 + \frac{1}{4})\lambda_0$. Each reflector array has $N = 200$ fingers, with width $\lambda_0/8 = 1$ μm. This design is patterned on the $LiNbO_3$ with electron-beam lithography, and then 7 nm/70 nm of Cr/Au is deposited using an electron-beam evaporator. An optical image of one of these devices is shown in Fig. 4.4.

4.3.2 SAW resonator characterization

The SAW resonators can be characterized by measuring the S11 (Fig. 4.5a). From this, we can see several strong resonances, corresponding to different cavity modes of the resonator. In particular, there are three very strong resonances that emerge clustered around 480 MHz. The quality factors can be extracted by fitting the S11 to Eq. A.51 and co-optimizing the fit to the real and imaginary components. From

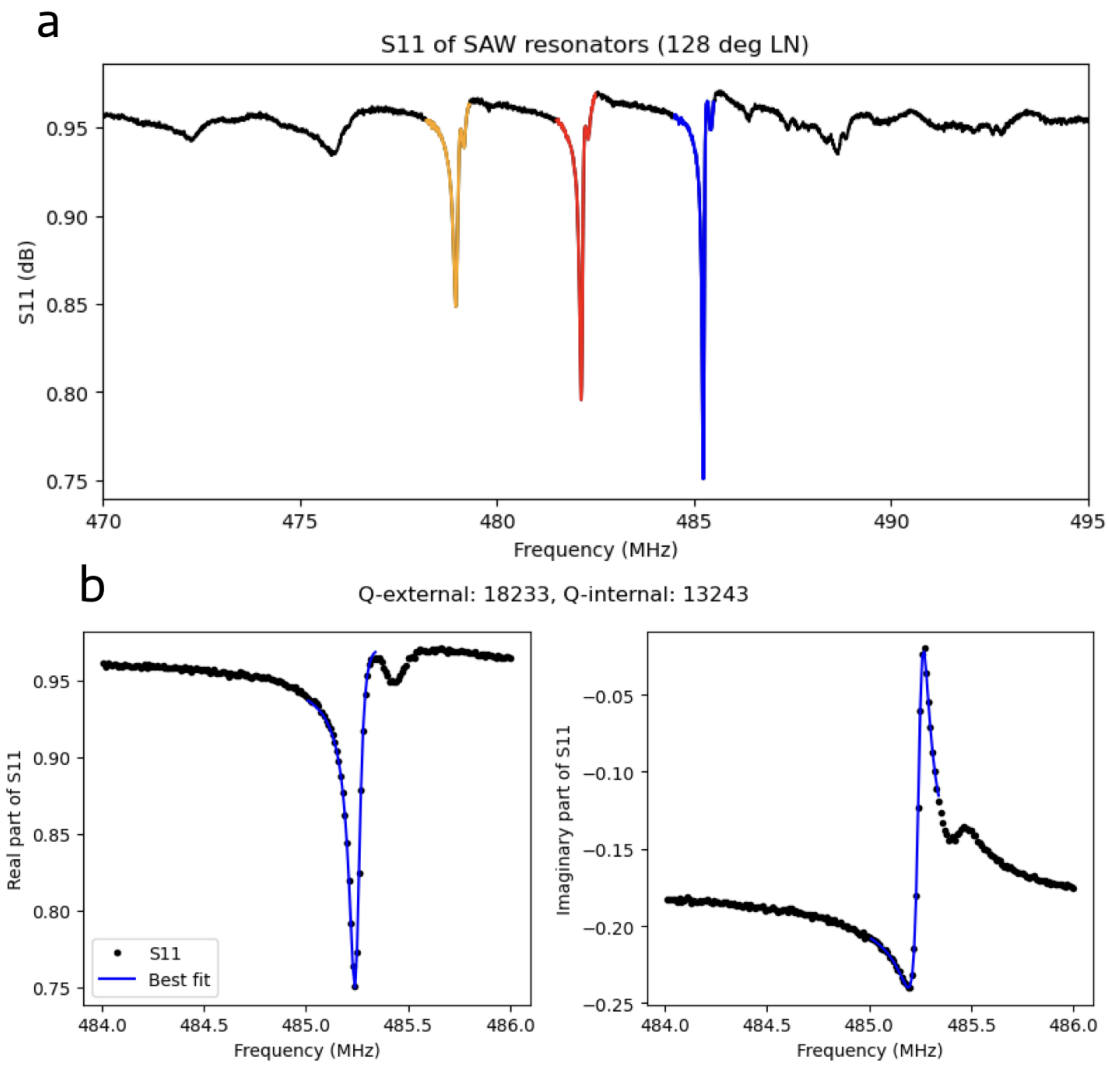

Figure 4.5: Characterization of a SAW resonator. a) S11 of the SAW resonator at room temperature, with three strong resonance peaks appearing. b) The fit of the real (left) and imaginary (right) components of the S11 to extract the loaded and unloaded quality factors.

this, we extract an unloaded (internal) quality factor of $Q_u \approx 13,000$ and loaded (external) quality factor of $Q_L \approx 18,000$, as shown in Fig. 4.5. The theoretical limit

for the quality factor of a SAW resonator at ∼500 MHz is $Q = 10^5$ without accounting for various losses such as material propagation and fabrication imperfections, so our measured Q_u is approaching this limit.

Furthermore, from the measured S11, we can extract information about our cavity. Specifically, because the spacing between the S11 peaks is $\sim$ 3.2 MHz, this gives a cavity length of $L_c = 1250$ μm, and a penetration depth $L_p = 80$ μm into the reflector array, or about $10\lambda_0$. With the velocity for SAWs in 128°C Y-cut $LiNbO_3$ $v_{SAW} = 3996$ m/s, this gives us a round trip time of $\tau_{RT} = .31$ μs. With the expression that $Q = 2\pi\tau_d f_0$ where τ_d is the exponential decay time of the stored energy, we can extract $\tau_d \approx 5.7$ μs. Then, for a given time t, we can calculate the amplitude of the SAW wave in the cavity relative to the initial amplitude with the function:

$$A(t) = e^{-t/\tau_d}. \tag{4.5}$$

4.3.3 2D device fabrication

The 2D material heterostructure consists of bilayer WSe_2 encapsulated by hBN around 30 nm thick. The heterostructure is stacked and transferred onto the nanopillar array by a conventional dry transfer method using polycarbonate/polydimethylsiloxane (Sylgard 184) stamps. PC residue was removed using chloroform for 1 h and followed by a 5 min rinse in IPA. After the device has been transferred, an aligned EBL write was done and 80 nm of indium-tin-oxide (ITO) was deposited using a sputtering system (Evactec LLS EVO) with O_2 conditioning. The ITO was then lifted off overnight in acetone.

The purpose of the ITO layer is twofold: the first is that it screens the in-plane electric field. As in the case of our work with long-range exciton transport via SAWs, suppressing this in-plane field is critical to prevent interlayer exciton dissociation, enabling us to study the effects of the SAWs on these exciton species. The second purpose of the ITO is to closely pin the 2D heterostructure to the substrate, thereby

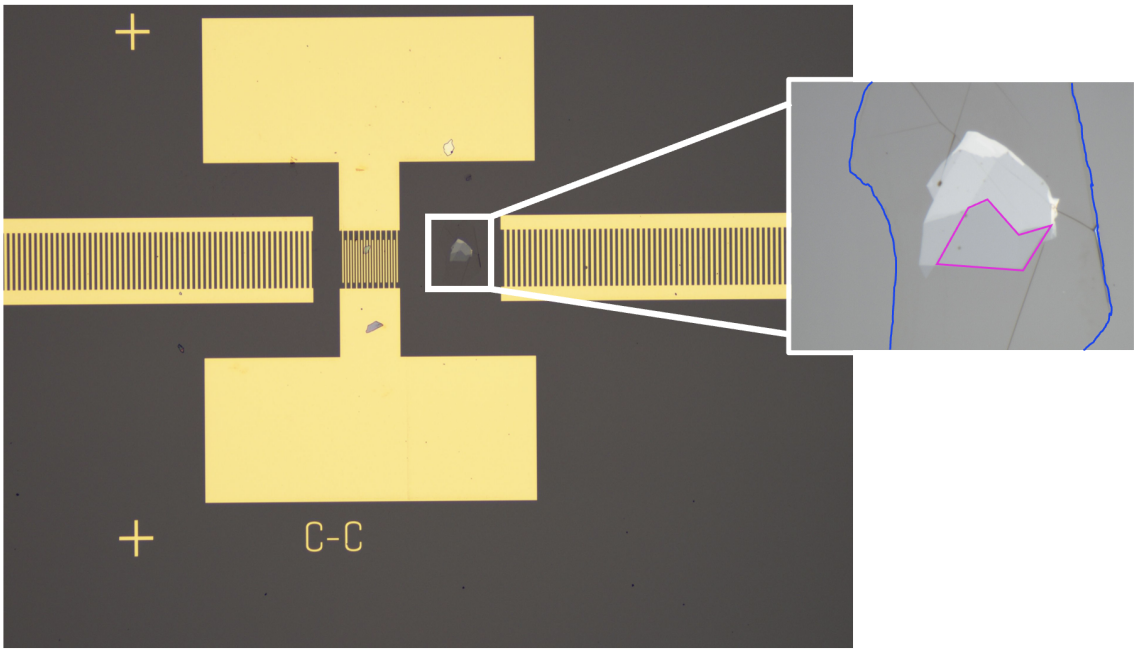

Figure 4.6: An optical image of 2D heterostructure inside a SAW resonator. The 2D heterostructure is transferred inside the resonator, shown in more detail in the inset. The hBN is outlined in blue, and the WSe_2 bilayer is outlined in pink.

maximizing the strain effects. One reason these 2D heterostructures exhibit such high deformability is that the atomic layers can slide against each other, thereby alleviating stress. This interlayer slipping is due to the 2D material's ultra-low sliding friction, which is known as "super-lubricity" [141]. While this property is advantageous for preventing the 2D materials from tearing, it poses a problem when trying to efficiently couple the SAW-induced strain in the substrate to the 2D heterostructure. The layer of ITO is meant to pin down the 2D heterostructure to the substrate to maximize the strain transferred directly to the excitons, and to minimize interlayer slipping between the 2D layers as well as slipping between the 2D layers and the substrate.

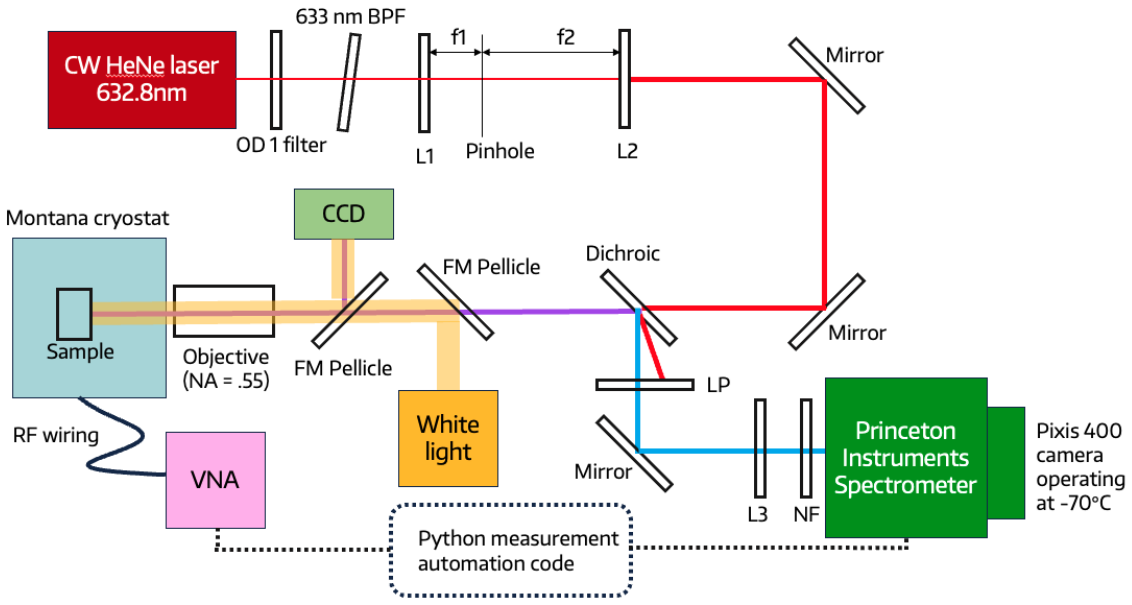

Figure 4.7: PL measurement scheme for observing effects of SAW resonator on 2D heterostructures.

4.3.4 Optical measurements

The devices are characterized optically with the measurement scheme shown in Fig. 4.7. As in Fig. 2.7 and Fig. 3.16, the photoluminescence is measured using a CW HeNe laser (632.8 nm). The laser spot is expanded and then directed down to the sample inside the Montana cryostat. The signal from the sample is then reflected back up out of the cryostat and directed towards the spectrometer (Princeton Instruments) and camera (Pixis 400). Along this path, the laser light is filtered out with a notch filter. The SAW resonator in the cryostat is wirebonded and connected via RF cables to the VNA (CMT C1209). Because we are interested in seeing how the PL changes as we fine-tune the frequency at which the SAW resonator operates, we introduced code to automate and sync the spectrometer and VNA triggers.

Because these measurements can take several hours, we monitored the PL over a

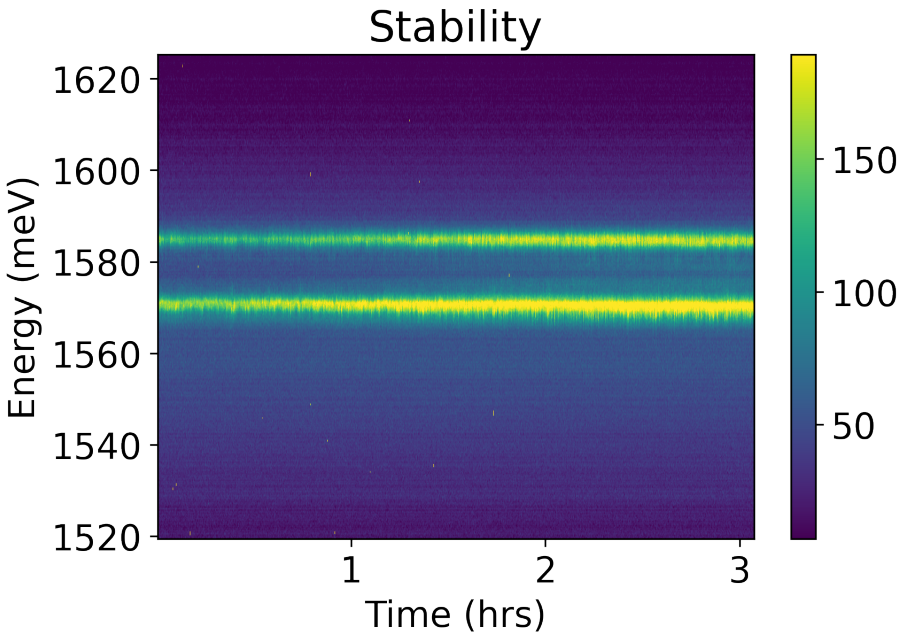

Figure 4.8: PL stability over several hours.

prolonged period to ensure that our system remained stable. Although there was a small amount of random drift in the system, as well as typical time jitter appearing in the PL, the system stayed relatively stable over the course of several hours.

4.4 Free exciton modulation

4.4.1 Exciton modulation with SAW frequency

We can first examine the PL) at 20 K, where excitons are more delocalized and not tightly bound to local defects. The PL was measured as the SAW drive frequency was swept, first with the SAW off and then with the SAW on. Each spectrum was fit with a Lorentzian profile, and the differences in integrated intensity, linewidth, and peak position between the SAW-on and SAW-off conditions are plotted in Fig.4.9. It is worth noting that these measurements were performed on an earlier SAW resonator design, which operates at somewhat different frequencies and has a lower quality

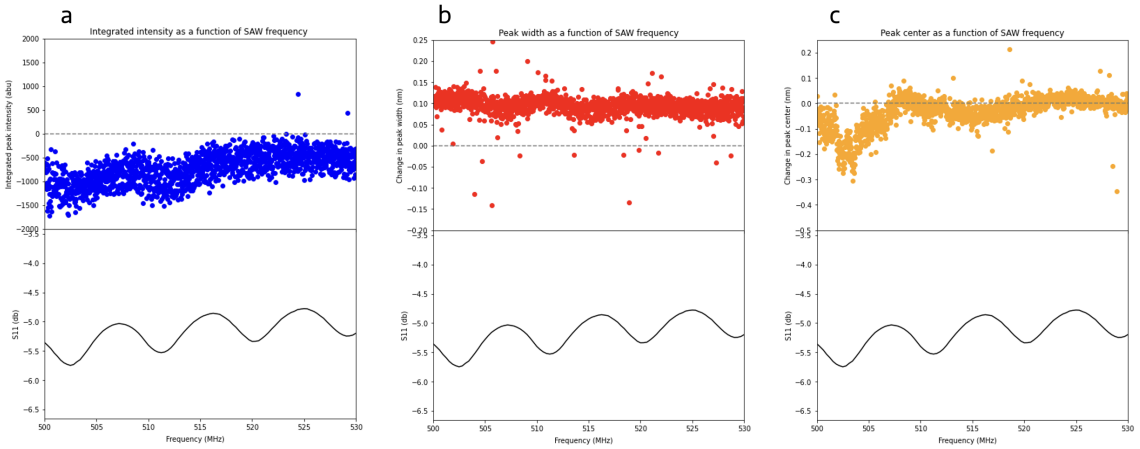

Figure 4.9: PL modulation with SAW power at 20K. A Lorentz function is fit to the QE PL peak at each frequency with and without SAW. The difference in the Lorentz fit is shown for intensity (a), width (b), and center (c).

factor (Q $\sim$ 2000) than the devices characterized in Fig.4.5 and Fig. 4.12. Despite this reduced Q, there is still clear evidence of modulation in both the integrated exciton intensity and linewidth at the SAW resonances, indicating that even modest acoustic confinement can influence the optical response of the heterostructure.

While these initial observations represent a small step, they illustrate the potential of SAW resonators to dynamically tailor excitonic properties in 2D systems. With improved cavity designs—featuring higher quality factors or operation deeper into the GHz regime—it should be possible to achieve more pronounced modulation, potentially accessing regimes of coherent exciton–phonon interactions. Such control could be extended toward dynamically tuning emission linewidths for indistinguishable photon sources, or creating moving exciton potentials to facilitate acoustic transport and programmable spatial exciton distributions. In this way, these early results lay the groundwork for using SAW resonators as versatile, non-invasive tools to actively engineer the optical landscape of 2D heterostructures.

4.4.2 SAW power dependence

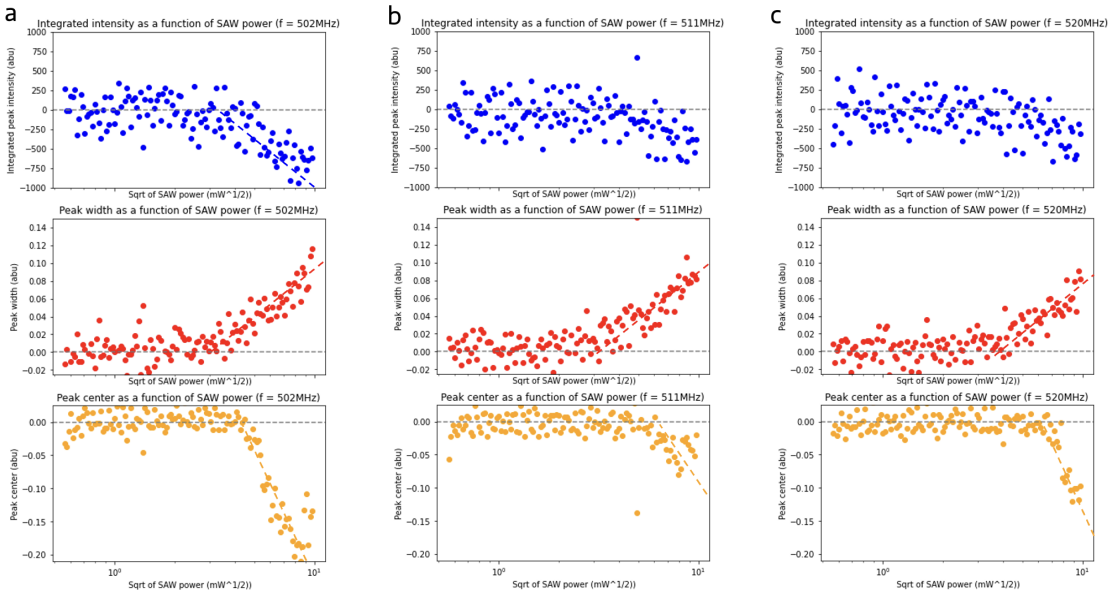

Figure 4.10: PL modulation with SAW power at (a) $f = 502$ MHz, (b) $f = 511$ MHz, and (c) $f = 520$ MHz. The top panels show the modulation of the PL intensity as a function of the square root of the SAW power. The center panels show the modulation of the PL width as a function of the square root of the SAW power. The bottom panels show the modulation of the PL center as a function of the square root of the SAW power.

We can look at the dependence of the PL modulation as a function of the SAW power in Fig. 4.10. There are a few interesting things we can see. First, in each of the plots, we can see that there appear to be two regimes. At low SAW power, there is very minimal modulation, and then at a critical SAW power, the SAW begins to modulate the PL. Second, the different SAW resonances modulate the PL differently; $f = 502$ MHz modulates the PL quite strongly, while $f = 511$ MHz has a much weaker effect on the PL modulation. We attribute this to the QE's position within

the cavity. Depending on the resonance being pumped, the QE might sit closer or further away from an anti-node, meaning the SAW will have a larger or smaller effect on PL modulation. Finally, we can also see that when we enter the regime in which the SAW power is modulating the PL, the modulation of the Lorentz peaks behaves linearly with the square root of the SAW power. This tells us that the modulation is coming primarily from the strain field of the SAW, which behaves linearly with the square root of the SAW power, as opposed to the electric field of the SAW, which behaves linearly with SAW power.

4.5 Quantum emitter modulation

4.5.1 Modulation of QEs with SAW frequency

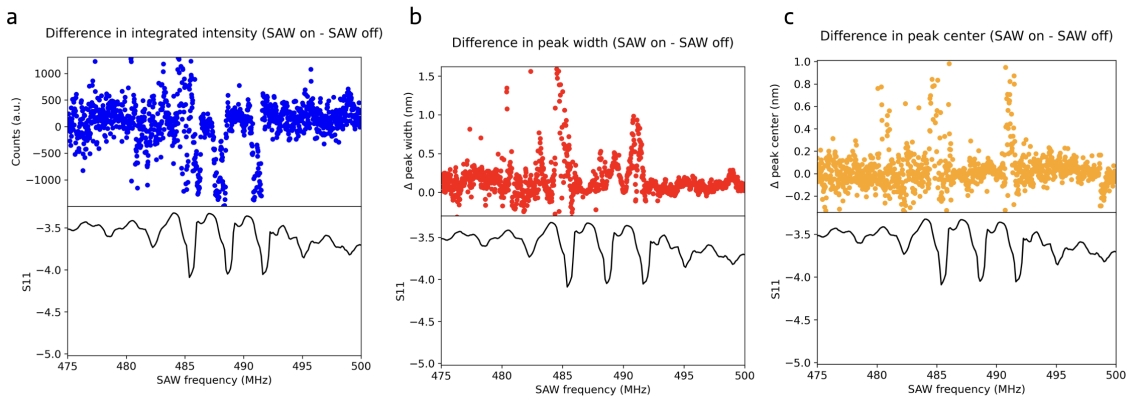

Figure 4.11: QE modulation with frequency in a SAW resonator. A Lorentz function is fit to the QE PL peak at each frequency with and without SAW. The difference in the Lorentz fit is shown for intensity (a), width (b), and center (c).

We can then look at a quantum emitter inside of a SAW resonator at different SAW frequencies, as shown in Fig. 4.11. For each frequency, the PL was measured with and without SAW. Each PL spectrum was then fit with a Lorentz peak, and then the difference between the Lorentz parameters SAW on - SAW off is plotted. In Fig. 4.11a,

we look at the difference in the integrated intensity of a QE peak with SAW on - SAW off. The integrated intensity is calculated based on the area under the Lorentz curve within the FWHM. It is important to consider the integrated intensity rather than just the peak intensity because the standing wave produces an oscillating effect within the local strain and electric field, which can lead to peak broadening. To understand how the SAW resonator modulation affects the overall exciton population, examining the integrated peak intensity allows us to separate this effect from the influence of SAW modulation on the peak width. We can see a clear decrease in the integrated intensity with SAW on at the SAW resonances, with minimal effect off resonance. This decrease in intensity could be due to the SAW pushing the excitons away from the local defect, or due to exciton dissociation. Either of these indicate that this QE is not located at an anti-node or that the SAW cavity confinement is not optimal. As expected, we also observe peak broadening with SAW on at the cavity resonances, as shown in Fig. 4.11b. We also observed some minimal peak broadening in Fig. 4.11c, likely due to the peak broadening enhancing existing asymmetries in the QE.

For a closer look at what is happening in Fig. 4.11, we can plot the PL with SAW on and SAW off for a frequency off resonance (Fig. 4.12a) and a frequency on resonance (Fig. 4.12b). For frequencies off the SAW resonance, like $f = 487$ MHz in Fig. 4.12a, there is almost no difference in the PL when the SAW is on compared to when the SAW is off. However, for frequencies on resonance, like $f = 485$ MHz in Fig. 4.12b, when the SAW is off, we see a sharp, defined peak. When we turn on the SAW, the peak broadens and significantly decreases in intensity. This essentially allows us to turn the QE off based on the SAW frequency we pump and based on the location of the QE in the cavity.

4.5.2 Long-lasting effects of SAW pump

We can also look at the longer-lasting effects of applying a SAW pulse. In Fig. 4.13, as in Fig. 4.11, we can look at the modulation of a QE in a cavity. For the first (second)

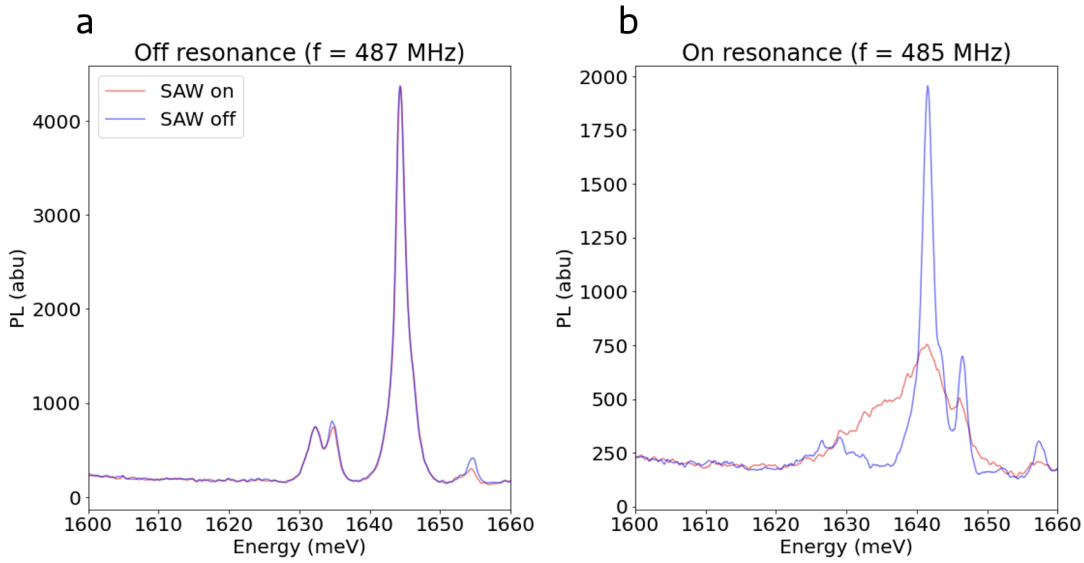

Figure 4.12: An example of the PL of the QE shown in Fig. 4.11. The PL is shown with the SAW on (red) and SAW off (blue) for (a) f = 487 MHz off a SAW resonance and for (b) f = 485 MHz on a SAW resonance.

peak, the modulation of the Lorentz integrated peak intensity, width, and center wavelength are shown in Fig. 4.13a, b, and c (Fig. 4.13d, e, and f). The first peak at around 1584 meV (782 nm) is narrow (¡ 1 meV) and stable enough to be considered a quantum emitter, based on our observations of the correlation of $g^{(2)}(0)$ measurements and peak width, while the second peak is more broad. For the first peak, we observe very distinct broadening of the QE linewidth and corresponding shift in peak center, with the modulation proportional to the strength of the resonance (Fig. 4.13b, c). Unlike in Fig. 4.11a, in Fig. 4.13a, the integrated intensity exhibits enhancement at the SAW resonances, indicating that this emitter is more favorably positioned in the cavity, preventing the SAW from pushing excitons away from the emitter and potentially even funneling excitons to the emitter via its dynamic potential well. Additionally, for the second peak, we observe no modulation in the PL at the SAW

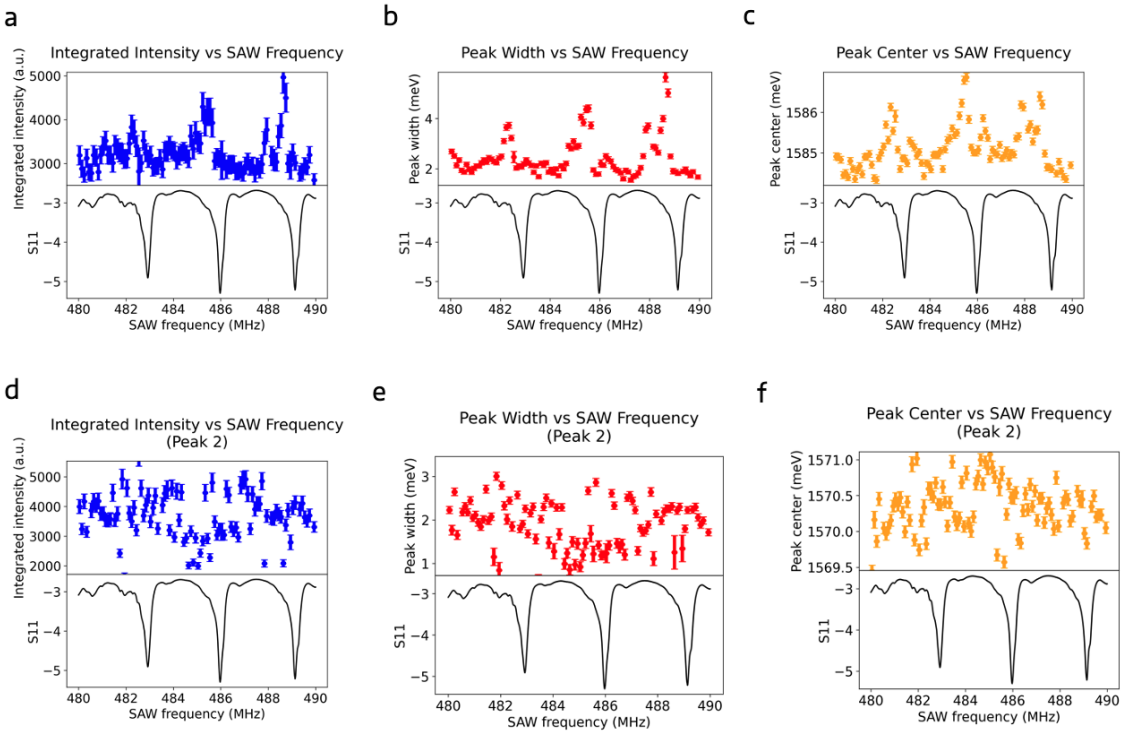

Figure 4.13: Two peaks modulated with frequency in a SAW resonator. A Lorentz function is fit to the QE PL peak at each frequency with SAW. For the first peak, the Lorentz fit is shown for intensity (a), width (b), and center (c). For the second peak, the Lorentz fit is shown for intensity (d), width (e), and center (f).

resonances (Fig. 4.13d, e, and f), indicating either that the second peak corresponds to a less favorable position inside the cavity, or that QEs like the first peak are more easily modulated by the SAW resonances due to the very tight confinement and extreme sensitivity to strain.

In Fig. 4.14, we can look at the colormaps of the PL acquired and fit in Fig. 4.13. The sweep was collected by parking the laser spot at a specific location on the sample, turning the SAW on, acquiring the PL with SAW for 1 s, turning the SAW off and waiting 1 s, acquiring the PL without SAW for 1 s, then repeating for each frequency.

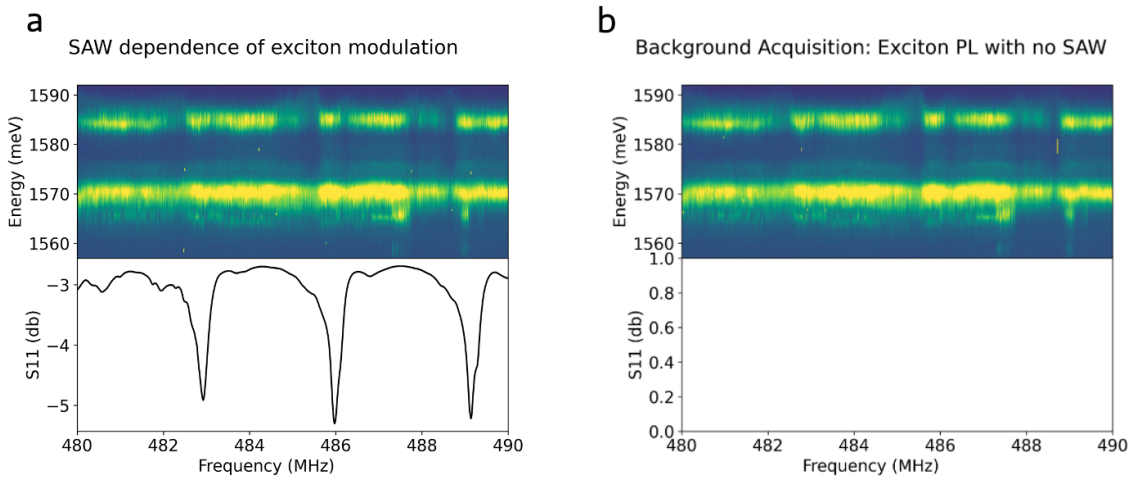

Figure 4.14: Colormaps of the PL as the SAW frequency is swept. The top panels are the PL colormap, with the PL intensity as the color, the energy on the y-axis and the SAW frequency on the x-axis. The lower panels are the SAW resonator S11, so that the SAW resonances can be matched up with the PL. a) The PL acquired with SAW on. b) The PL acquired with SAW off.

The goal with doing the sweep via this method was that acquiring the data with and without SAW at each frequency point would allow us to account for small sample drift and jitter when looking at the differences in the Lorentz fit as in Fig. 4.11. However, when we look at the colormaps for this data in Fig. 4.14, we see something interesting. In Fig. 4.14a, we plot the colormap just for the data in which the SAW was turned on, and this behaves as we expect. Around the SAW resonances, we see a clear broadening of the first peak in particular, corresponding with what we saw in Fig. 4.13. However, in Fig. 4.14b, we plot only the PL acquired with the SAW off, and this looks very similar to Fig. 4.14a, in which the SAW is on, with just some minor fluctuations in intensity, particularly around the two peaks, but these changes are very minor. For Fig. 4.14b, we would expect the PL to remain unchanged across

all SAW frequencies, and resemble just a stability test, as in Fig. 4.8. However, the fact that Fig. 4.14b so closely follows Fig. 4.14a tells us that there are potential long lasting effects at play when we turn on the SAW at the cavity's resonance.

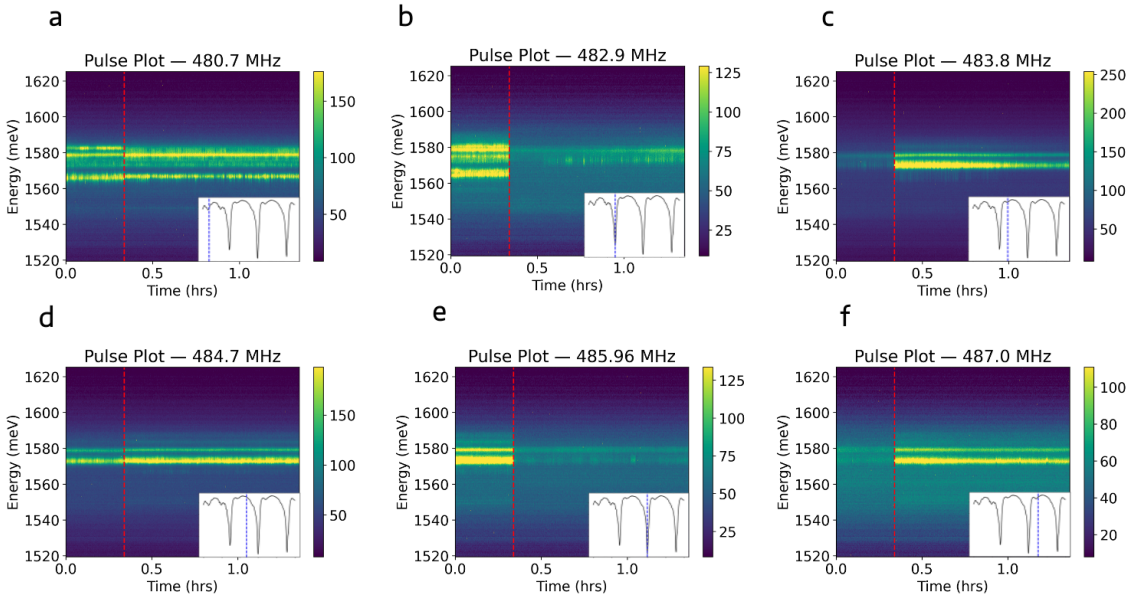

Figure 4.15: PL before and after applying a SAW pulse at different frequencies. The PL is collected before the SAW turns on, then a single SAW pulse is sent at the time indicated by the red dashed line, and the PL is monitored after. The inset shows the frequency of the SAW pulse with respect to the SAW resonances. The SAW pulse sent is at a) $f = 480.7$ MHz, b) $f = 482.9$ MHz, c) $f = 483.8$ MHz, d) $f = 484.7$ MHz, e) $f = 485.96$ MHz, and f) $f = 487$ MHz.

We investigate this effect in Fig. 4.15. We parked our laser spot and then began collecting the PL for a period of time to monitor the stability. We then sent a 1 s SAW pulse at 15 dB (red dashed line in Fig. 4.15), then observed the PL for a period of time afterwards. We repeated this for frequencies on and off the SAW resonances sequentially. What we observed is very interesting– we began with a pulse off resonance at $f = 480.7$ MHz in Fig. 4.15a, and observe very minimal changes.

When we move on resonance to $f = 482.9$ MHz Fig. 4.15b, we send a pulse and immediately observe very strong suppression of the excitons that lasts over an hour. As we move back off resonance to $f = 483.8$ MHz in Fig. 4.15c, the exciton signal is still very suppressed for the first part of the measurement, but after sending in an off-resonance pulse, the PL once again becomes bright, but we note that the energy of the peaks that appear are in fact different than those that were bright in Fig. 4.15b. We then shift frequency a bit more but stay off resonance at $f = 484.7$ MHz in Fig. 4.15d, and just like in Fig. 4.15a, we observe very minimal change, although there is a slight enhancement of the exciton signal at 1587 meV. In Fig. 4.15e, we then move back on resonance to $f = 485.96$ MHz, and once again this strong on-resonance pulse strongly suppresses the exciton signal. In Fig. 4.15f, as in Fig. 4.15c, we start with the excitonic signal still very suppressed, and as we send in the pulse off-resonance at $f = 487.0$ MHz, this once again allows us to recover the bright exciton signal. Another example of this type of pulse sequencing is shown in Fig. E.1.

This effect we observe is really novel; because the effects are so long-lasting, it appears as if the on-resonance SAW pulse is nudging the heterostructure slightly, changing the PL, and the off-resonance SAW pulse is able to dislodge the shift and allow the heterostructure to return back to its original configuration. While we deposited the ITO layer on top of the heterostructure in an effort to pin it in place (Section 4.3.3), the layers of the 2D heterostructure are free to slide against each other, and this is what we suspect is happening. If the layers of the bilayer WSe_2 are shifting with respect to each other, or if the bilayer WSe_2 is shifting in-between the hBN encapsulation, then this could easily result in the pulse causing an enhancement or suppression of the exciton intensity, or even the appearance of a new peak. These results are still very preliminary, and require careful and extensive further study to more carefully understand the dynamics at play. Seeing if the effects of the pulse ever reverse on their own with a much longer measurement will give us a better sense of the timescales at play. Sending the pulses in different sequences (i.e. several pulses

on resonance, several pulses off resonance, etc.) will allow us to better understand the individual effects of the on-resonance pulses and the off-resonance pulses. Studying the PL dependence on the pulse power and length will also allow us insight into the mechanisms at play. By using Raman spectroscopy, we could also look at localized phonon modes to see if there is long-lasting lattice distortion, which would confirm our current theory of the interlayer sliding.

Despite all of these unknowns, this apparent long-lived and frequency-dependent response to SAW pulses suggests a new avenue of exciton and material control in 2D heterostructures. The apparent ability of on- and off-resonance acoustic pulses to "lock" and "unlock" the excitonic configuration points to a mechanical rearrangement at the atomic scale, possibly involving interlayer sliding or local strain redistribution, that persist well beyond the duration of the SAW itself. This opens up intriguing possibilities for nonvolatile, acoustically controlled excitonic states and new modes of information storage or logic based on mechanical reconfiguration of the 2D ordering. With further study, this effect could lead to a deeper understanding of the mechanical dynamics of van der Waals heterostructures and introduce new ways to pattern or switch optical properties in reconfigurable optoelectronic platforms.

4.6 Future and ongoing work

4.6.1 Exciton modulation

Building on the initial observations of exciton linewidth and intensity modulation, a key direction for ongoing work is to achieve more pronounced and controlled exciton modulation. This will involve pushing the SAW cavity designs toward even higher quality factors and operation at higher frequencies in the GHz regime. With improved acoustic confinement and shorter periods relative to exciton lifetimes, we can aim to reach a regime where exciton–phonon interactions are not just dynamically tunable, but potentially coherent [142]. This could enable time-resolved control of exciton pop-

ulations, such as modulating emission linewidths for indistinguishable photon sources, or precisely tuning recombination rates in the quantum regime, as well as storing information in stable room temperature excitons. Additionally, by carefully varying the SAW power, we can explore the crossover from small perturbative modulation to large-amplitude regimes where the exciton band structure is periodically driven, opening possibilities for dynamic Floquet engineering in 2D materials [143].

4.6.2 Spatial effects

Another exciting direction is to directly probe the spatial modulation of exciton density within the SAW cavity, particularly the possibility of exciton trapping at the anti-nodes of the standing wave. As suggested by our simulations and preliminary observations of power-dependent intensity changes, the periodic strain landscape could create effective dynamic traps that accumulate excitons at the anti-nodes. Future experiments will include spatially resolved PL mapping under SAW excitation to directly visualize this redistribution. By adjusting the SAW wavelength and cavity mode, we could engineer programmable exciton patterns across the heterostructure, effectively creating a reconfigurable exciton lattice. Adding a second SAW resonator perpendicular to the first would provide even more spatial control, allowing us to create a grid with independent x and y spacings. Such a platform could be invaluable for studying exciton transport, interactions, and potentially exciton condensation in a precisely tunable potential landscape.

4.6.3 Long-lasting effects and persistent modulation

The unexpectedly long-lived effects we observe after applying SAW pulses which we observed as persistent changes in PL intensity, linewidth, or even the appearance of new peaks, suggest intriguing avenues for further study. While we suspect these phenomena may arise from slight nanoscale rearrangements within the heterostructure, such as interlayer sliding of the WSe_2 bilayer relative to itself or to the hBN encap-

sulation similar to [139], systematic investigations are needed to uncover the exact mechanisms. Future experiments could involve temperature-dependent measurements to probe the energy barriers for such layer shifts, as well as atomic force microscopy (AFM) or nano-Raman mapping before and after SAW pulsing to detect any subtle structural changes.

Understanding these effects is not only of fundamental interest, revealing how dynamic strain can permanently or quasi-permanently reshape 2D heterostructures, but could also lead to new applications. For example, SAW pulses could potentially serve as a local "strain writing" tool, reconfiguring excitonic landscapes on demand without the need for static patterning or external gates. Additionally, if such layer rearrangements can be controlled reproducibly, they may enable new types of non-volatile excitonic or optical memory, where information is encoded into the structural configuration of the heterostructure itself. Overall, systematically exploring these persistent modulation effects will shed light on the interplay between dynamic mechanical driving and the intrinsic flexibility of van der Waals materials, opening up possibilities for both novel device functionalities and deeper insights into the mechanics of layered quantum systems.

4.6.4 Remote pumping

Finally, we are highly interested in using this platform to integrate the work we demonstrated in Chapter 2 and Chapter 3 by using SAWs to remotely pump quantum emitters. This enables us to turn our QEs on and off without directly shining our laser spot on them, greatly reducing the thermal energy at the QE point. We hypothesize that this will improve the quality of our single photon emitters and give us a much cleaner signal with less background noise. While we were able to demonstrate long-range exciton transport in [29] and highly tunable quantum emitters in [30], these two platforms have fundamentally different requirements. For exciton transport, it is essential samples be as clean and defect-free as possible, while QEs require

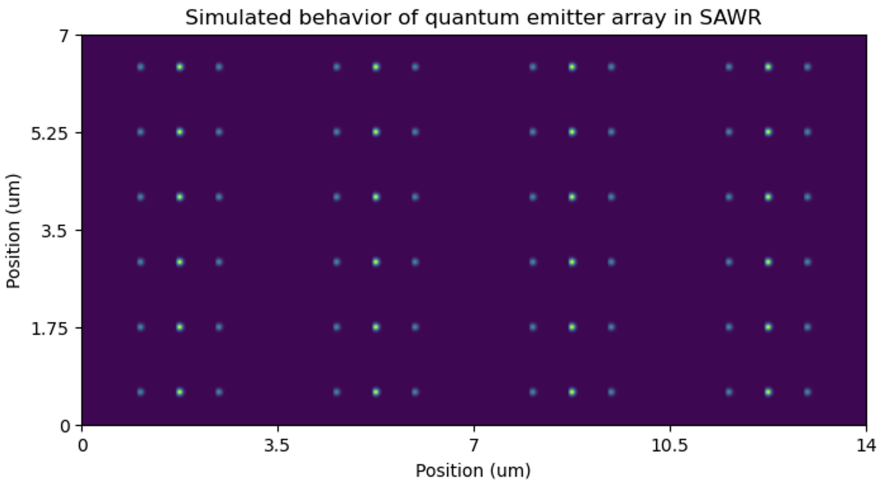

Figure 4.16: Simulated array of quantum emitters being spatially turned on and excited by a remote pump inside of a SAW resonator.

both defects and local strain. Additionally, exciton transport is optimal at elevated temperatures (100 K) to prevent excitons from becoming trapped at local defects and keep them mobile, while QEs require very low temperatures (< 10 K) for optimal quantum confinement. Surface acoustic wave resonators with very high quality factors enable enhanced light-matter interactions, making it feasible to overcome these fundamental challenges. Because SAWs can propagate or create standing patterns over hundreds of microns, they provide a means to transport or modulate excitons far from where they are generated, as shown in Fig. 4.16. This could enable optical readout at one location while dynamically tuning exciton properties at another, laying the groundwork for integrated on-chip excitonic circuits or networks of coupled quantum emitters. Combining remote pumping with cavity-enhanced SAW designs could unlock new schemes for spatially multiplexed quantum or optoelectronic functionalities in 2D heterostructures.

Chapter 5

CONCLUSIONS AND OUTLOOKS

5.1 Summary of thesis

2D materials are an active area of research because their reduced dimensionality leads to new physical properties that could enable different kinds of devices and applications. Recently, advances in AI and the growing demand for computing power have highlighted some of the fundamental limits of scaling silicon transistors. In this context, 2D semiconductors have come up as a possible way to keep pushing device sizes smaller and address these challenges [144]. Beyond classical computing, these 2D materials also have rich quantum properties and degrees of freedom, such as valley and spin, and can host single-photon emitters, making them promising platforms for quantum information science. They are particularly attractive for these applications because they can be easily integrated onto chips, often support long-lived excitonic states even at room temperature, and offer a high degree of tunability through external fields or stacking. Recent advances, such as the observation of the fractional quantum anomalous Hall effect [8], have made 2D materials even more compelling as potential platforms for topological quantum computing.

In Chapter 1, we present the motivation and background that set the context for this work. Chapter 2 then describes our experiments on transporting 2D excitons using surface acoustic waves (SAWs). By launching SAWs on a piezoelectric substrate, we created dynamic electric and strain fields that trapped interlayer excitons in bilayer WSe_2 at the lowest points of the electric potential and carried them toward a recombination site at the edge of the heterostructure. Unlike much of the previous work that focused on enhancing exciton diffusion, our approach enables long-range,

directional exciton transport. This method is also non-invasive and fully on-chip, avoiding direct patterning of the 2D heterostructure while maintaining a compact, integrable design. Together, these results mark a significant step toward realizing excitonic transistors and circuits, and could ultimately enable all-optical readout of quantum information from on-chip sources.

In Chapter 3, we focus on our work with highly tunable quantum emitters in bilayer WSe_2. We create these emitters by strain-engineering the material with SiO_2 nanopillars, onto which we transfer our 2D heterostructure. By incorporating graphite gates, we apply an out-of-plane electric field that allows us to tune the energy of these quantum emitters. Beyond demonstrating this tunability, we also observe signatures of single exciton-phonon mode coupling, where the emitters interact with local breathing mode phonons in the WSe_2. This coupling is itself tunable with the electric field, opening up the possibility of using a THz source to generate phonon Fock states or to store and read out information directly from the phonon modes of the 2D material.

Finally, in Chapter 4, we explore our ongoing work with bilayer WSe_2 inside a SAW resonator cavity. By placing the 2D heterostructure within a high-quality acoustic cavity, we aim to achieve standing surface acoustic waves that periodically modulate the exciton energy landscape. This approach could enable enhanced light-matter interactions by synchronizing exciton recombination with the SAW field, potentially allowing for stimulated emission or phonon-assisted control of quantum states. Such SAW resonators also provide a route to coupling distant quantum emitters via shared mechanical modes, paving the way for scalable phononic quantum networks based on 2D materials.

5.2 Future directions

Looking ahead, each of these projects offers clear paths for further exploration. For the work on SAW-driven exciton transport, a natural next step is to engineer more complex SAW circuits, such as transistors or multi-path acoustic waveguides, to realize

exciton-based logic elements. Further investigation of the temperature dependence, combined with improved material quality, could push this long-range transport toward higher temperatures and even room temperature operation.

For the quantum emitters, future studies could involve coupling these highly tunable 2D QEs to photonic crystal cavities or waveguides to achieve Purcell enhancement, superradiance, or deterministic on-chip single-photon routing. Leveraging twisted bilayer or heterobilayer TMDs may also enable moiré-confined emitters with even larger electric dipole moments, providing greater tunability and the possibility of realizing dipole-coupled emitter arrays. Additionally, further exploration of the exciton–phonon coupling could open the door to manipulating or coherently driving single phonon modes, laying the groundwork for hybrid exciton–phonon quantum systems or for generating phonon Fock states directly in a solid-state platform.

In the SAW resonator work, future directions could include achieving stronger acoustic confinement to potentially enter the regime of coherent exciton–phonon coupling, where phonons could store or mediate quantum information. The standing SAW field could be harnessed to pattern exciton populations across the device or to create long-lived spatial modulations that persist beyond the pulse duration. Moreover, by mediating interactions between multiple, spatially separated quantum emitters, the standing wave could act as a first step toward realizing a phonon-based quantum bus that connects distinct quantum nodes on a chip, paving the way for scalable quantum networks in solid-state platforms.

More broadly, combining these approaches offers exciting opportunities. For example, integrating strain-engineered quantum emitters within a SAW cavity could enable dynamic control of phonon-coupled emission, while propagating SAWs might be used to coherently shuttle excitons between quantum emitters at different sites on a chip. Remote pumping of these emitters via SAWs provides a spatially selective, switchable means to turn them on and off, and could also enhance emitter quality by eliminating local heating and background noise from direct optical excitation. Such

hybrid systems bring us closer to fully on-chip quantum networks that harness excitons, photons, and phonons together to process and transmit quantum information in a single, versatile platform.

Taken together, these directions point toward a broader vision where strain engineering 2D transition metal dichalcogenides, with their exceptional tunability and ease of integration, forms the building blocks of versatile quantum and optoelectronic circuits. By advancing our ability to control their excitonic, photonic, and phononic degrees of freedom, we move closer to realizing fully integrated quantum systems for computing, communication, and sensing.

Appendix A

SURFACE ACOUSTIC WAVES FROM FUNDAMENTAL PRINCIPLES

A.1 Solid mechanics

First, let us understand the dynamics of stress and strain in a solid. The elasticity of a material is dependent on internal forces and the displacement of a point from its equilibrium. Stress T refers to the force applied to a material per unit area, while strain S is the resulting displacement of particles in the material. We follow the definition of "particle" from [25]. A particle refers to a region of a material that is much smaller than the wavelength of any deformation but much larger than the interatomic distance, allowing atomic impurities to be neglected. A particle is at equilibrium in a material at point $\mathbf{x} = (x_1, x_2, x_3)$. With a stress applied to the material, the particle is displaced $\mathbf{u} = (u_1, u_2, u_3)$ to be at position $\mathbf{x} + \mathbf{u}$. We can then define the strain at each point with

$$S_{ij}(x_1, x_2, x_3) = \frac{1}{2}\Big(\frac{\partial u_i}{\partial x_j} + \frac{\partial u_j}{\partial x_i}\Big), \qquad i, j = 1, 2, 3. \tag{A.1}$$

This definition tells us that there will be no internal forces if $\mathbf{u}$ is independent of $\mathbf{x}$, since this would correspond to a displacement of the bulk material. Rotations also do not result in a strain. The strain is a second-rank tensor and symmetrical, so $S_{ij} = S_{ji}$ [25].

Likewise, we can describe the internal forces with stress tensor $T_{ij} = \frac{F_i}{A_j}$ where F_i is the i component of force $\mathbf{F}$ and A_j is the j component of area $\mathbf{A}$. A positive force corresponds to the material stretching, while a negative force corresponds to the material compressing. The area $\mathbf{A}$ is a vector as well, with a positive value

corresponding to the normal vector moving outward from the material, and a negative value corresponding to the normal vector moving inward from the material [26].

Assuming the materials are linear, which is a safe assumption for the relatively small forces from acoustic waves, we can relate stress and strain using Hooke's law of elasticity with

$$T_{ij} = \sum_k \sum_l c_{ijkl} S_{kl}, \qquad i,j,k,l = 1,2,3 \tag{A.2}$$

where the coefficient c_{ijkl} is the stiffness tensor and a property intrinsic to the material. This is a fourth-rank tensor, but can be reduced by noting that the symmetry of $S_{ij} = S_{ji}$ requires that the stiffness is the same if i and j or if k and l are interchanged.

When both stress and strain are dependent on time, we can obtain an equation of motion from Eqs. A.1 & A.2.

We can define the velocity and acceleration of the particle with

$$v_i = \frac{\partial u_i}{\partial t}, \qquad\qquad a_i = \frac{\partial^2 u_i}{\partial t^2}. \tag{A.3}$$

For a fractional cube of material with each side length δ and total volume δ^3, the force from a displacement in the i direction is given by

$$F_i = \delta^3 \Big[\sum_j \frac{\partial T_{ij}}{\partial x_j} \Big]. \tag{A.4}$$

From Newton's second law, we can equate this to the acceleration from Eq. A.3 multiplied by the mass of the cube $\rho\delta^3$ where ρ is the material density. This finally gives us our equation of motion,

$$\sum_j \frac{\partial T_{ij}}{\partial x_j} = \rho \frac{\partial^2 u_i}{\partial t^2}, \qquad i,j = 1,2,3. \tag{A.5}$$

A.2 Piezoelectricity

For piezoelectric materials, Eq. A.5 is still valid, but the stress components depend on the electric field $\mathbf{E}$ or the equivalent electric displacement $\mathbf{D}$, where $\mathbf{D} = \epsilon\mathbf{E}$. The constitutive relations are given by

$$\mathbf{D} = \mathbf{eS} + \epsilon\mathbf{E} \tag{A.6}$$

and

$$\mathbf{T} = \mathbf{cS} - \mathbf{e^T E} \tag{A.7}$$

where ϵ_{ij} is the permittivity tensor and e_{ijk} is the piezoelectric tensor that relates the elastic and electric fields.

To simplify the notation, we can look specifically at a case in which a force is applied along the z-axis, resulting in a displacement along the z-axis, giving us $T_{zz} = \frac{F_z}{A_z}$, $S = \frac{\partial u_z}{\partial z}$, and $T_{zz} = c_{zzzz}S_{zz}$. Eqs. A.6 and A.7 become

$$D_3 = e_{33}S_3 + \epsilon E_3 \tag{A.8}$$

and

$$T_3 = c_{33}S_3 + e_{33}E_3. \tag{A.9}$$

Like in Eq. A.5, we can use Newton's second law to get

$$\frac{\partial T}{\partial z} = \rho\frac{\partial v}{\partial t}. \tag{A.10}$$

Using the relation $\partial S/\partial t = \partial v/\partial z$ obtained from taking the partial time derivative of Eq. A.1, we can take the partial time derivative of Eq. A.9 to give us

$$\frac{\partial v}{\partial z} = \frac{1}{c}\frac{\partial T}{\partial t} + \frac{e}{c}\frac{\partial E}{\partial t} = \frac{1}{c'}\frac{\partial T}{\partial t} + \frac{e}{\epsilon c'}\frac{\partial D}{\partial t} \tag{A.11}$$

where

$$c' = c + \frac{e^2}{\epsilon} = c(1 + K^2). \tag{A.12}$$

Here, $K^2 = \frac{e^2}{\epsilon c}$ is the piezoelectric efficiency. From Gauss's law,

$$\frac{\partial D_3}{\partial z} = \rho' \qquad (D_1, D_2 = 0) \tag{A.13}$$

where ρ' is the charge density and is a constant. Therefore, when we take the second partial derivative of Eq. A.11, we get our final relation

$$\frac{\partial^2 v}{\partial z^2} = \frac{1}{c'}\frac{\partial}{\partial z}\Big(\frac{\partial T}{\partial t}\Big) + \frac{e}{\epsilon c'}\frac{\partial^2 D}{\partial t \partial z} \qquad \Longrightarrow \qquad \frac{\partial^2 v}{\partial z^2} = \frac{\rho}{c'}\frac{\partial^2 v}{\partial t^2}. \tag{A.14}$$

which is the wave equation.

A.3 Interdigital transducer

Waves on a transmission line are characterized by their characteristic inductance L and capacitance C. These LC circuits are described by two differential equations from fundamental circuit theory shown in Eqs. A.15 and A.16, where V is voltage and I is current.

$$\frac{\partial V}{\partial z} = -L\frac{\partial I}{\partial t} \tag{A.15}$$

$$\frac{\partial I}{\partial z} = -C\frac{\partial V}{\partial t} \tag{A.16}$$

By taking the second derivative of Eq. A.15 with respect to z, we can obtain

$$\frac{\partial^2 V}{\partial z^2} = LC\frac{\partial^2 V}{\partial t^2} \tag{A.17}$$

which is equivalent to the wave equation. Assuming that the wave takes the form of $e^{[i(\omega t - kz)]}$, then the wave equation gives us the relation

$$k^2 = \omega^2 LC \tag{A.18}$$

where $k = 2\pi/\lambda$ is the wavenumber and $\omega = 2\pi f$ is the radian frequency. The phase velocity v_0 can be given by

$$v_0 = f\lambda = \frac{\omega}{k} = \frac{1}{\sqrt{LC}}. \tag{A.19}$$

The characteristic impedance can be given by

$$Z_0 = \frac{V}{I} = \sqrt{\frac{L}{C}}. \tag{A.20}$$

Finally, we can obtain expressions for the power flow with

$$P = \frac{1}{2} V I^* = \frac{|V|^2}{2Z_0} \tag{A.21}$$

and the time-averaged potential energy with

$$U = \frac{1}{2} C|V^2| = \frac{1}{2} L|I|^2. \tag{A.22}$$

We can see that Eqs. A.15 and A.16 are in the same form as Eqs. A.10 and A.11, and Eq. A.17 is equivalent to Eq. A.14. From these parallels, we can equate some of our IDT parameters to their circuit equivalents. Now, we can try to equate some values. The surface potential ϕ is equivalent to the voltage V. The current I does not have a physical direct equivalent for SAWs, so instead we can define it so that we obtain the correct power relation using Eq. A.21.

$$P = \frac{1}{2} V I^* = \frac{1}{2} \phi I^* = \frac{|\phi|^2}{2Z_0} \tag{A.23}$$

This gives us $I^* = 1/2Z_0$ and $Z_0 = |\phi|^2/2P$, allowing us to obtain some equivalence equations using the surface wave velocity v_0.

$$C = \frac{1}{Z_0 v_0} \tag{A.24a}$$

$$L = \frac{Z_0}{v_0} \tag{A.24b}$$

$$U = \frac{1}{2} C |\phi|^2 \tag{A.24c}$$

By defining Z_0 using the total power P, we can include the power from both the acoustic and electric field components of the SAW. The power will be determined by the acoustic aperture W. For a given ϕ, a larger W will result in a larger power and a smaller impedance. We can define a quantity z_0 that is independent of the acoustic aperture and the wavelength with

$$Z_0 = \frac{z_0}{W/\lambda}. \tag{A.25}$$

Likewise, we can define the characteristic admittance Y_0 as well as a quantity independent of the acoustic aperture and wavelength y_0.

$$Y_0 = \frac{1}{Z_0} = y_0 \frac{W}{\lambda} \tag{A.26}$$

We recall our definition of the piezoelectric coupling coefficient K^2 from Eq. 1.1 and v_0 from Eq. A.19, letting us write for small changes in velocity

$$K^2 = 2\frac{\Delta v_0}{v_0} \approx \frac{\Delta C}{C} \tag{A.27}$$

where ΔC is the capacitance per unit length. We can define this capacitance as

$$\Delta C = -\frac{\rho_s W}{\phi} \tag{A.28}$$

where ρ_s is the charge per unit area.

We now want to write ρ_s in terms of ϕ. We can assume the fields from charge ρ_s are described by a potential $\psi = \psi_s e^{-\alpha y} e^{-ikz}$ where α is a constant and ψ_s is the peak value. Let's assume the substrate is isotropic with permittivity ϵ_p. Then,

$$D_y = -\epsilon_p \frac{\partial \psi}{\partial y} = \epsilon_p \alpha \psi \tag{A.29a}$$

$$D_z = -\epsilon_p \frac{\partial \psi}{\partial z} = ik\epsilon_p \psi \tag{A.29b}$$

Maxwell's first law gives us

$$\frac{\partial D_y}{\partial y} + \frac{\partial D_z}{\partial z} = 0 \quad \Longrightarrow \quad (\alpha^2 - k^2)\epsilon_p \psi = 0 \quad \Longrightarrow \quad \alpha = |k|. \tag{A.30}$$

Then, we can substitue this in Eq. A.29a and get

$$D_y = \epsilon_p |k| \psi \tag{A.31}$$

for the field in the substrate. We can see that D_y will be discontinuous, and above the surface, we can do the same manipulations but substitute in ϵ_0 and get

$$D_y = -\epsilon_0 |k| \psi \tag{A.32}$$

where the negative sign comes from the field decaying in the $-y$ direction rather than the $+y$ direction. From Maxwell's first law, we also know that the field discontinuity is equal to the surface charge density, giving us

$$\rho_s = (\epsilon_p + \epsilon_0)|k|\psi_s = \frac{2\pi}{\lambda}(\epsilon_p + \epsilon_0)\psi_s. \tag{A.33}$$

Substituting this in to Eq. A.28, we get

$$\Delta C = 2\pi(\epsilon_p + \epsilon_0)\frac{W}{\lambda}\Big(- \frac{\psi_s}{\phi}\Big) \tag{A.34}$$

where ψ_s is the potential produced by the charge at the surface and ϕ is the potential created by the SAW at the surface. But because there is no longitudinal electric field, and we have

$$E_z = ik(\phi + \psi) = 0, \tag{A.35}$$

meaning that $\psi_s = -\phi$. This allows us to reduce Eq. A.34 to

$$\Delta C = 2\pi(\epsilon_p + \epsilon_0)\frac{W}{\lambda}. \tag{A.36}$$

Then, substituting Eq. A.27 and A.24a into A.36, we can get

$$K^2 y_0 = 2\pi\epsilon v_0 \tag{A.37}$$

where $\epsilon = \epsilon_0 + \epsilon_p$. Rearranging, we can get

$$Z_0 = \frac{W\epsilon\omega}{K^2}. \tag{A.38}$$

Plugging this into Eq. A.23, we get

$$P_{SAW} = W|\phi|^2\frac{\epsilon\omega}{2K^2}, \tag{A.39}$$

which is Eq. 1.3 in the main text [25].

A.4 Equivalent circuit

To evaluate the efficiency of our IDT, we are interested in how the power is distributed across its components. Understanding these power ratios as a function of frequency enables us to characterize the efficiency of the IDT and fit the scattering matrix (S-matrix) data measured using a vector network analyzer (VNA). For a two-port network, the S-matrix is $2x2$, where $S11$ ($S22$) represents the first (second) port reflection coefficient, and $S21$ ($S12$) represents the transmission from port one (two) to port two (one).

Based on the relations we proved in the previous section, the IDT can be modeled using the equivalent circuit shown in Fig. A.1, generalized from the Butterworth

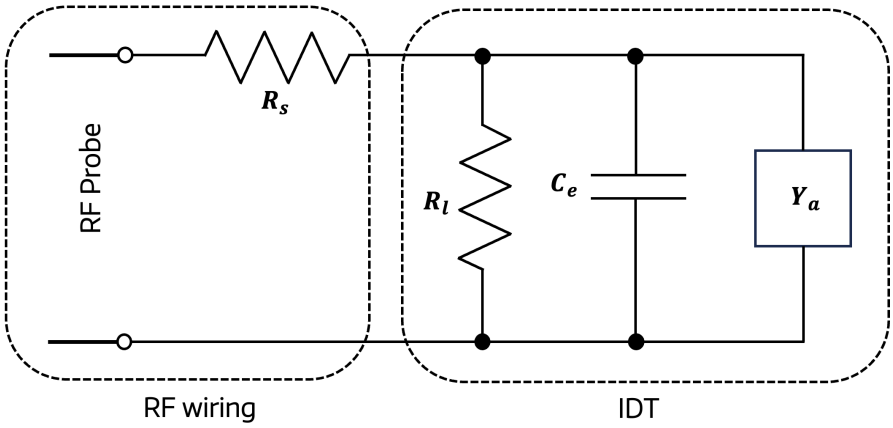

Figure A.1: The equivalent circuit of an IDT.

Van Dyke (BVD) model [145]. The electromechanical response of the transducer is given by the acoustic admittance Y_a, which has real and complex components and is frequency dependent. The capacitance between electrodes is given by C_e, and the effective leakage resistance between the electrodes is given by R_l. Finally, we account for the resistance between the total series resistance of the IDT and the RF probe with R_s.

We can simplify this circuit further to R_s and Z_l connected in series, where Z_L is the complex impedance of the effective IDT circuit (R_l, C_e, Y_a), as shown in Eq. A.44.

$$Z_L(\omega) = \frac{1}{R_l^{-1} + i\omega C_e + Y_a(\omega)} \tag{A.40}$$

The power of these respective lumped components can be given by

$$P_{R_s} = P_{in}\frac{R_s}{R_s + \mathbb{R}(Z_L(\omega))} \tag{A.41a}$$

$$P_{Z_L} = P_{in}\frac{\mathbb{R}(Z_L(\omega))}{R_s + \mathbb{R}(Z_L(\omega))}, \tag{A.41b}$$

where P_{in} is the input power. Looking more closely at the power consumption of the different IDT components, we see

$$P_{R_l} = P_{Z_L} \frac{R_l^{-1}}{R_l^{-1} + \mathbb{R}(Y_a(\omega))} \tag{A.42a}$$

$$P_{Y_a} = P_{Z_L} \frac{\mathbb{R}(Y_a(\omega))}{R_l^{-1} + \mathbb{R}(Y_a(\omega))} \tag{A.42b}$$

$$P_{C_e} = 0. \tag{A.42c}$$

Substituting Eq. A.41 in to Eq. A.42, we get

$$P_{R_l} = P_{in} \frac{\mathbb{R}(Z_L(\omega))}{R_s + \mathbb{R}(Z_L(\omega))} \frac{R_l^{-1}}{R_l^{-1} + \mathbb{R}(Y_a(\omega))} \tag{A.43a}$$

$$P_{Y_a} = P_{in} \frac{\mathbb{R}(Z_L(\omega))}{R_s + \mathbb{R}(Z_L(\omega))} \frac{\mathbb{R}(Y_a(\omega))}{R_l^{-1} + \mathbb{R}(Y_a(\omega))}. \tag{A.43b}$$

A.5 IDT fitting

Once we obtain the complex $S11$ data from the VNA, we can fit it using the lumped element equivalent circuit. We first want to start near the resonance dip ω_0, where we approximate $Y_a = 0$ because the power reflected near this dip is almost solely due to the acoustic effects from Y_a, which is a function of ω. We can then look at the load impedance Z_0' that excludes Y_a:

$$Z_0' = R_s + \frac{1}{R_l^{-1} + i\omega C_e}. \tag{A.44}$$

We can fit this to the S11 with the relation

$$Z_0' = R_{char} \frac{1 + \mathbb{C}(S11(\omega))}{1 - \mathbb{C}(S11(\omega))} \tag{A.45}$$

where $R_{char} = 50\Omega$ is determined by the VNA [146]. Then, we can extract R_s, R_l, and C_e from the $S11$ data. Once we have obtained these fixed values, we can then look at a wider frequency range to find $Y_a(\omega)$ by looking at the total impedance:

$$Z_0 = R_s + \frac{1}{R_l^{-1} + i\omega C_e + Y_a(\omega)} = R_{char}\frac{1 + \mathbb{C}(S11(\omega))}{1 - \mathbb{C}(S11(\omega))}. \tag{A.46}$$

Because the only unknown is $Y_a(\omega)$, we can fit this to our data. Using our power relations, we could determine the power distribution on each lumped circuit component using Eq. A.21 by plugging in the appropriate Z_0 and fitting the expression with the $S11$ data. The power ratio of $Y_a(\omega_0)$, where ω_0 is the IDT resonance, gives the on-resonance conversion efficiency.

A.6 SAW resonators

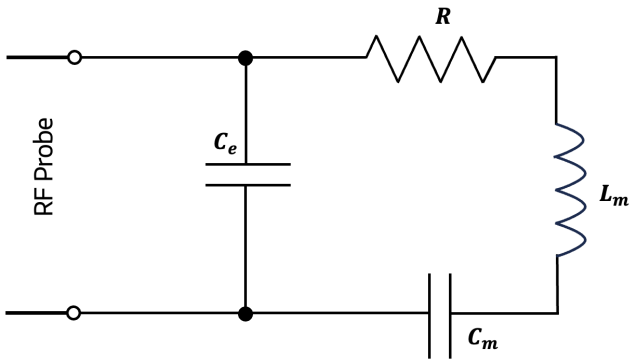

Figure A.2: The equivalent circuit of a one-port SAW resonator.

In this work, we focus on one-port SAW resonators. These are a single IDT with a set of reflectors on either side, as seen in Fig. 1.11. Most of the equations derived in the first few sections regarding SAWs remain applicable. The new equivalent circuit for these SAW resonators is the modified BVD circuit, shown in Fig. A.2 [25].

C_e is the transducer capacitance, to which the resonator RLC circuit is connected in parallel. The inductance L_m and capacitance C_m account for the 'motional' components of the SAW resonance, and are present for most forms of electromechanical resonators that are designed for a single resonance. The resistance R accounts for the resistance between the various circuit elements. C_e is fixed and due to the input from the IDT, so we can consider just the admittance from the RLC branch when looking at the cavity properties. The admittance will be large at the resonant frequency $\omega_r = 1/\sqrt{L_m C_m}$.

The cavity will form standing waves when constructive interference forms between the forward propagating SAW from the IDT and the reflected signal from the reflectors, and must satisfy $L_c = n\lambda/2$, where the factor of 2 comes from the wave traveling the cavity in both directions before a standing wave can form. Therefore, we can specify that the distance between the two gratings must be

$$d = \left(2n \pm \frac{1}{2}\right)\frac{\lambda_0}{2}. \tag{A.47}$$

We can write the fundamental cavity frequency as $f_n = nv_f/2L_c$, allowing us to see that the spacing between our resonances is given by

$$\frac{\Delta f_n}{f_0} = \frac{f_{n+1} - f_n}{f_0} = \frac{\lambda_0}{2L_c}. \tag{A.48}$$

A.7 Quality factor fitting

The unloaded quality factor of the resonator is given by $Q_u = \omega_0 L_c/R_c$ where R_c is the total resistance of the circuit. This considers the quality factor just of the cavity. Just looking at the two reflector arrays, this gives us a total reflectivity of $R \simeq \tan(Nr)$ as defined in Chapter 1.4.4.

The quality factor of the resonator including the IDT is known as the loaded quality factor and is given by $Q_L = \omega_0 L_c/Z$, where the resistance R_c in the internal quality factor is replaced with the characteristic impedance Z of the whole effective

circuit. For a one-port resonator connected to a feed line, the S11 is given by

$$S11 = \frac{Z - Z_f}{Z + Z_f} \tag{A.49}$$

where Z_f is the impedance of the feed line of the VNA, which is 50 [147]. Our one-port SAW resonator has a characteristic impedance of

$$Z(\omega) = R + i\omega L\Big(1 - \frac{1}{\omega^2 LC}\Big) \approx R + i\frac{2RQ_i\Delta\omega}{\omega_0} \tag{A.50}$$

from the equivalent circuit. With the approximations and substituting in $\omega_0 = 1/\sqrt{LC}$, this gives us

$$S11(f) = \frac{(Q_e - Q_i)/Q_e + i2Q_i\delta f}{(Q_e + Q_i)/Q_e + i2Q_i\delta f} \tag{A.51}$$

where $\delta f = (f - f_0)/f$ [148]. This allows us to fit our measured $S11$ resonances to extract the internal and external quality factors.

Appendix B

FABRICATION

B.1 Electron beam lithography

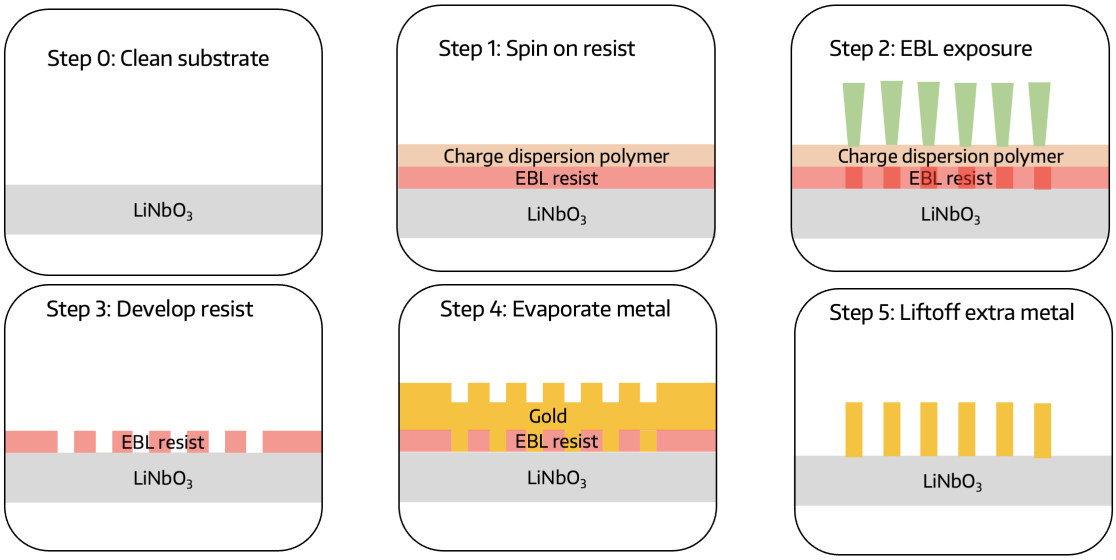

Figure B.1: Diagram of the steps for performing an EBL write.

The steps for performing an electron-beam lithography (EBL) write are shown in Fig. B.1. The example is on a LiNbO**3** substrate, but the steps will be, for the most part, the same on any substrate. Before beginning an EBL write, the substrate must be thoroughly cleaned. Typically, a 10 min sonication in acetone followed by a 1 min rinse in IPA is sufficient, but if the chip is still dirty after this, longer sonication or even a Piranha etch may be required to completely clean the chip. After cleaning the chip and before spinning on the resist, it is advisable to do a pre-bake to evaporate

any trapped moisture in the chip, which can impact how well the resist will adhere to the chip.

The next step will be spinning on the resist. The choice of resist as well as resist thickness will be dependent on several factors, including the resolution required by the pattern, the substrate, and the post-development plan (i.e., if a metal will be evaporated on top, if so how thick, etc.). For the devices we made in Chapter 2 and Chapter 4, we first used ZEP520A to pattern the SAW resonators, and then after transferring the 2D heterostructures, we used PMMA to pattern the ITO layer on top. For the devices in Chapter 3, we first used ZEP520A to pattern the nanopillars, and then did an aligned photolithography step to pattern the electrodes connecting to the graphene gates. Additionally, for insulating substrates such as $LiNbO_3$, an additional layer of a charge dispersion polymer needs to be spun on top of the resist after it has been baked. This charge dispersion layer (Dischem DisCharge +) prevents charge buildup on the insulator and allows for much higher resolution patterning. Both ZEP and PMMA are positive resists, meaning that the area of the desired pattern is directly exposed.

The next step is the actual EBL exposure. The electron current of the write will be determined by pattern size and resolution, while the dose of the write will be dependent on the substrate and resist. This often will need to be determined experimentally by doing a dose test, where a pattern is written in a repeated array, with each element at a different dose. All EBL writes in Chapters 2, 3, and 4 were done at the Washington Nanofabrication Facility (WNF) on the University of Washington's campus with the JEOL JBX-6300FS electron beam lithography system. Smaller features (< 1 μm) were written with a 1 nA current, while larger features (> 1 μm) were written with an 8 nA current. The patterns written via EBL were generated via Python (GDS Factory) or, for aligned writes, were drawn via KLayout.

After the EBL exposure, the resist can be developed. For insulating substrates that have the charge dispersion polymer spun on them, the first step is a 1 min

rinse in DI water. The development recipe will depend on the resist and substrate– ZEP is developed with amyl acetate, and PMMA is developed with acetone. This is then followed by a rinse in IPA and a gentle O_2 plasma cleaning step to remove any remaining resist residue on the pattern area. After developing the resist, the desired material can be evaporated on top of the substrate, and the remaining material and resist can be removed via liftoff– for ZEP, liftoff is done overnight in N-Methyl-2-pyrrolidone (NMP) at 80°C, and for PMMA, liftoff is done for 4+ hours in acetone.

B.2 Polymer recipes

B.2.1 Polycarbonate

In a glass bottle, 10% polycarbonate (PC) is mixed with 90% chloroform by weight. This is then stirred and baked at 60°C for 2+ days or until uniform. The elasticity of the PC is determined by the ratio of PC to chloroform, and can be adjusted to desired consistency. Because chloroform evaporates rapidly and the properties of the PC are determined by the ratio of the PC to chloroform, it is important to keep the bottle tightly air-sealed to prevent it from degrading over time.

To make thin layers of PC on microscope slides as required for transfers, we take two pre-cleaned glass microscope slides (it is very important these slides are very clean) and put them face up in a wet bench. We use a glass pipette to deposit PC onto one slide, then use the face-up side of the second slide to sandwich on top of the slide with the PC. Firmly and smoothly, we wiggle the top slide around to evenly coat the first slide and release any bubbles that may be in the PC, then quickly and smoothly slide the top slide off the bottom slide and PC. If the PC looks streaky or uneven, adjust the time at which the second slide is removed. The bottom slide with the PC on top of it can then air dry in a covered petri dish for at least 20 minutes and at most 24 hours. The longer the PC slide dries, the more brittle and less sticky it becomes, which can make picking up the 2D materials more difficult.

B.2.2 Polydimethylsiloxane

We mix polydimethylsiloxane (PDMS) from Sylgard 184 in a petri dish, and let set for several days in a vacuum chamber to release the bubbles. To create the domed pillars we use for transfers, after the PDMS has set, we punch out small cylinders (5 mm). We mix fresh PDMS so that it is still viscous, and then using a glass stirrer or something similar, use surface tension to deposit a drop of the viscous PDMS onto the cured PDMS cylinder. We then bake these at 80°C for 2+ days to help them set.

B.3 2D device fabrication

B.3.1 Exfoliations

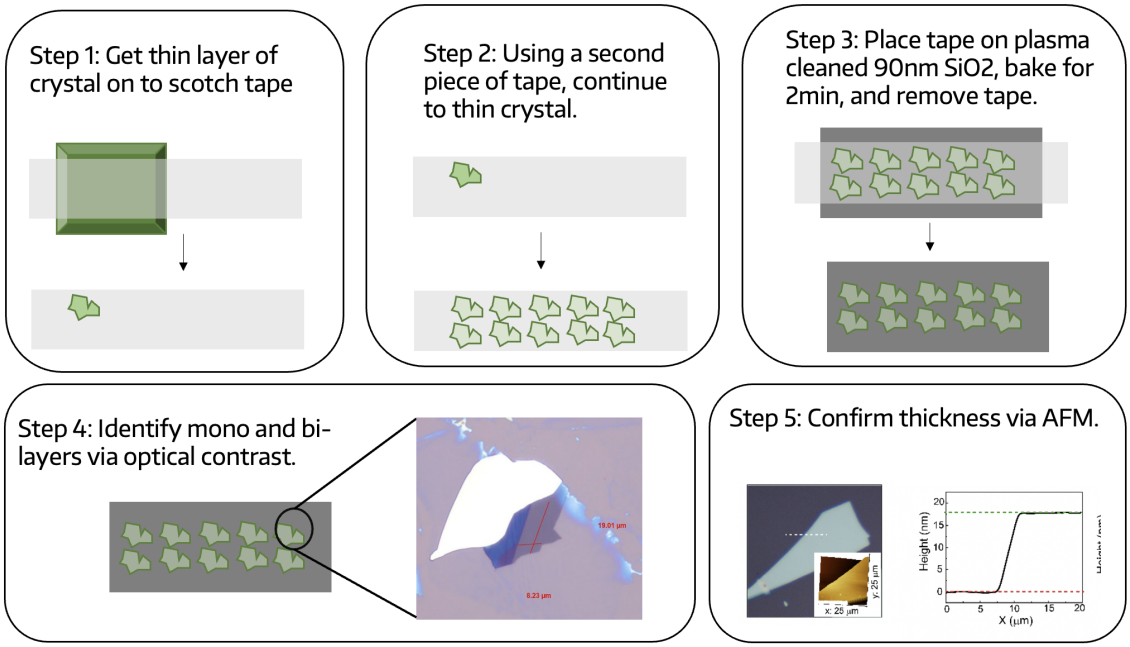

Figure B.2: Diagram of the steps for exfoliating a bulk crystal.

When making 2D heterostructures, the first step is to exfoliate the bulk crystal to the 2D limit. These bulk crystals can be bought commercially or grown by academic

collaborators. Fig. B.2 shows the steps for the exfoliation process. The first step is to get a small piece of the bulk crystal onto a piece of scotch tape. This can be done either by place the tape directly onto the crystal and carefully lifting it off, or by peeling off a small piece of the bulk crystal with tweezers and placing that on the tape (recommended). Using a second piece of tape, place them together sticky sides together, and lift up, avoiding overlap with the crystal on both pieces of tape. Using this method, we can continue to thin the crystal. The optimal number of times to do this will depend on the desired thickness, the material, and the initial crystal thickness. By the end, the tape should ideally be full of an array of the initial crystal piece, as shown at the bottom of the panel for Step 2 in Fig. B.2.

Once the tapes are made, they are ready to be used to transfer the crystal onto a substrate. We use 90 nm SiO_2, as this gives optimal contrast for thin and monolayer 2D flakes. We dice these into long rectangles about the same size as the length of tape we are using in Step 2 and plasma clean these in O_2 thoroughly to increase the adhesion of the 2D flakes to the substrate. Once the chips have been plasma cleaned, we can place the tape onto the chips, pressing firmly to make sure they are in good contact. The length of time the tapes stay on the chips as well as if a bake is necessary will depend on the crystal as well as environmental factors. For hBN, we found leaving the tapes on for at least an hour without a bake gives us optimal results, while for WSe_2, we bake the chips tape side down for 2 min at 120°C and let cool for about 10 minutes before removing the tapes. When removing the tapes, it is key to do this gently and smoothly, with the angle between the tape and the chip as small as possible.

After the tapes have been removed, the 2D flakes can be identified in a microscope via optical contrast. As an example, in the inset of Step 4 in Fig. B.2 an optical image of a WSe_2 is shown, with the dimensions of the monolayer portion shown in red. The thickness and atomic smoothness of these exfoliated flakes can be confirmed via atomic force microscopy (AFM).

B.3.2 Making a stamp

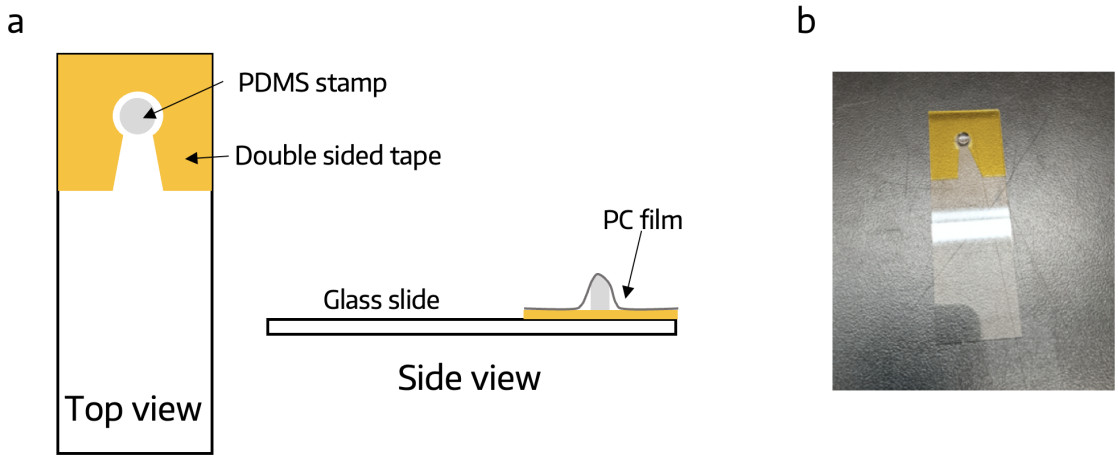

Figure B.3: Diagram of the stamp used for 2D transfers. a) A diagram of the stamp from the top view (left) and a side view (right). b) An optical image of a stamp.

A key part of a 2D transfer is the stamp that picks up and deposits the 2D flakes onto a substrate, as shown in Fig. B.3. The stamp is a PDMS domed pillar that is flexible, with a thin layer of sticky PC on top. The PDMS allows for gently rolling over the 2D flakes, with the domed nature making alignment between layers significantly easier. The PC on top of the PDMS serves as the layer that will actually come into contact with the 2D materials, and can pick up 2D flakes from their original substrate, and then melt the final heterostructure on to the final substrate.

To create the stamp, place a pre-cleaned glass microscope slide on a clean, flat surface. Punch a hole a bit bigger than the PDMS pillar in the center of a piece of double-sided tape, and place one side on the top end of the microscope slide. Place the PDMS pillar in the punched hole. Take a piece of scotch tape and punch a hole in the center. Place this piece of tape over a slide of thin PC, with the punched hole aligned in center of the PC slide. Using a razor or sharp edge, detach the PC that

is not under the scotch tape. Gently place the tape with the PC on it onto the slide with the PDMS stamp, carefully aligning the hole punch in the scotch tape with the PDMS pillar. With this method, at the center of the stamp, the only layers will be the PDMS stamp with the thin layer of PC gently folded over it.

B.3.3 Transfer stage

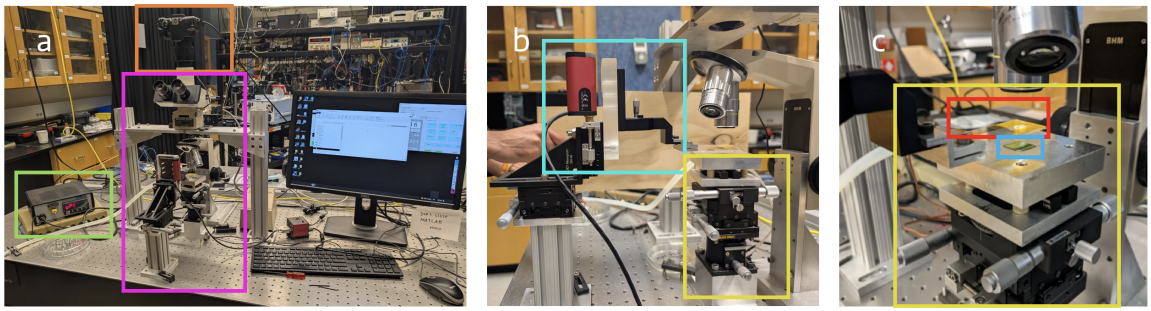

Figure B.4: Images of the transfer stage. a) Entire transfer stage set-up. The main transfer stage set-up is outlined with the magenta box. The orange box outlines the camera that allows us to view the transfer stage through the computer on the right of the picture. The green box outlines the temperature controller for the transfer stage. b) A closer side view of the transfer stage. An objective lens focuses to the stage, which is outlined in the yellow box. The stage has x, y, and rotational stage translators, along with temperature control and a vacuum line. The stamp mount is shown in the teal box, which is attached to a z-axis motorized positioner. c) A closer look at the stamp and the stage. The stage is again shown with the yellow box, with a chip on it in the blue box fastened to the stage with a vacuum line. The stamp is shown in the red box.

The transfer stage is shown in Fig. B.4. A zoomed-out view is shown in Fig. B.4a, with the main components being outlined with a pink box. This consists of a stage, which has temperature control (controller outlined in green) and a vacuum line to

fix the chip in place. The stage also has x, y, and rotational stage translators. An objective lens focuses on the stage, and this can be viewed either through the eyepieces or through the camera shown in the orange box, which is connected to the monitor shown in the right of the picture. Also in the magenta box is the stamp mount, which is shown in more detail with a side view in Fig. B.4b.

The stamp is mounted to the components outlined in teal with the polymer face down. The stamp mount has a z-axis motorized positioner that allows for precise control of the stamp's velocity as it touches down on a chip to pick up or place down a flake on a chip. The stage component is shown outlined in the yellow box, shown more clearly in Fig. B.4c. The stage has a chip on it which is fixed in place with a vacuum line (blue). The chip is positioned via the stage positioners, and then the stamp (red) can be lowered slowly to gently roll over a flake.

B.3.4 Performing transfers

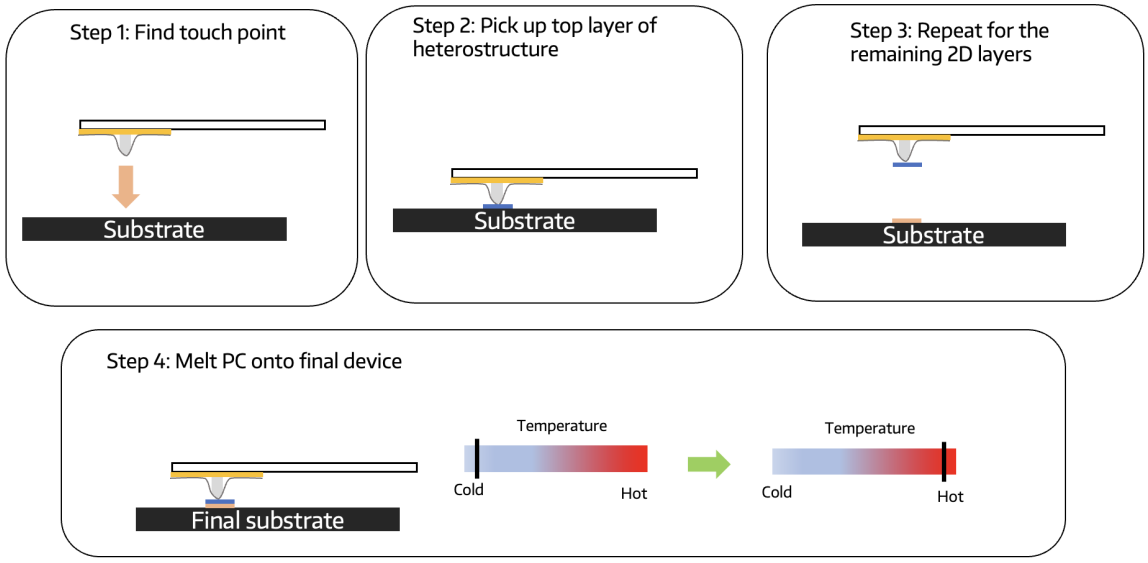

Figure B.5: Diagram showing the principle behind a dry 2D heterostructure transfer.

A diagram showing the principle of a dry transfer is shown in Fig. B.5. The first step is to lower the stamp onto a clean substrate with clear features, to make a note of the height at which the stamp touches the substrate. With this height calibrated, we can then proceed with the transfer, lowering the stamp to the substrate to pick up each 2D layer. When picking up multiple 2D flakes, each can be aligned to the location of the previously picked-up flake on the stamp. Once all of the layers of the 2D heterostructure have been picked up, the stamp can then be lowered onto the final substrate, and the temperature of the stage is increased slowly to the melting point of the PC. Once the PC is fully melted onto the substrate, the stamp can be raised. The melted PC and the heterostructure underneath it will remain on the final substrate. The melted PC can be removed with chloroform, leaving just the heterostructure.

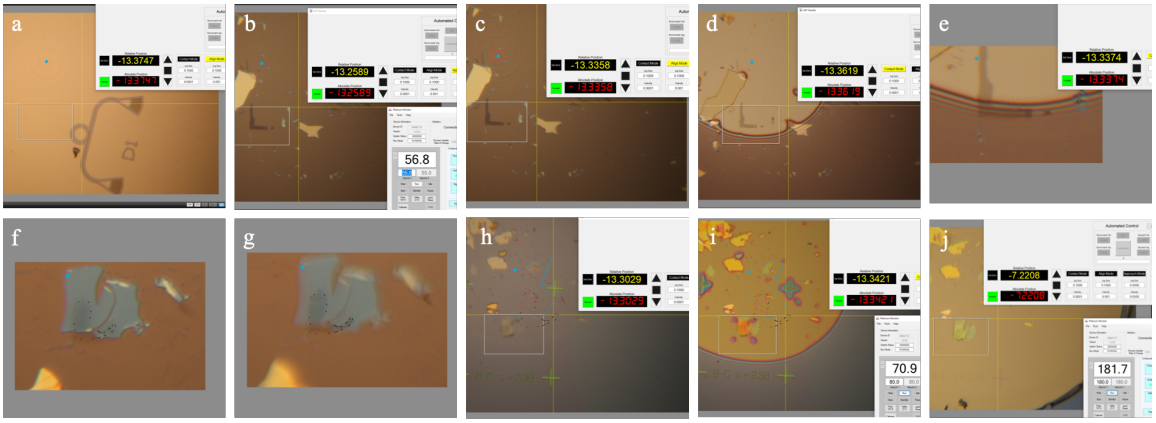

Figure B.6: Images taken at each step of a transfer, outlining the procedure.

Images taken during a real transfer are shown in Fig. B.6. For our transfer stage, the steps are as follows:

a) After making a new stamp, the first step is finding the touch point on a clean chip with some clear features to focus on. Slowly lower the stamp down until ripples appear and make a note of the height at which the stamp touches the chip. Use an annotator tool to make a mark on the computer screen of the touch point (blue dot

in the middle of the ripples), which is the peak of the domed PDMS pillar. Raise the stamp and place the chip that contains the first flake that will be picked up on the vacuum stage.

b) Increase the stage temperature to between 55-60°C. Lower the stamp until it is slightly higher than the touch point, and align the first flake relative to the touch point. It should be slightly away from the touch point so that it can be smoothly rolled over the entirety of the flake.

c) After completing the alignment, lower the stamp down until it fully touches down on the chip.

d) As slowly and smoothly as possible, continue lowering the stamp until you are fully covering the desired flake. Let the stamp sit covering the flake at the raised temperature for at least 10 minutes.

e) (Zoomed in mode) As slowly and smoothly as possible, begin raising the stamp. If the contrast of the flake changes as the stamp is lifted up, this is a good sign that the flake has been picked up. When the flake is fully picked up, raise the stamp fully.

f) Place the chip with the next flake on the vacuum line and repeat step b), aligning the next desired flake with the flakes that have already been picked up by your stamp.

g) Check the alignment by adjusting the focus between the chip (as in (f)) and the stamp pillar (as in (g)). Once the alignment is good, repeat steps (c)-(e). Repeat this process until all desired flakes have been picked up and the heterostructure is ready to be transferred to its final substrate.

IF SAMPLE IS NOT SENSITIVE TO BUBBLES:

h) Align the substrate with the position of the heterostructure on the stamp. Push the stamp through the heterostructure fully, as in (c) and (d).

i) Begin increasing the temperature of the stage in 10°C intervals. Wait for the stage to reach the set temperature, then increase the temperature by another 10°C. Continue this until the stage reaches 160°C, let the stage sit at that temperature for

5 minutes, increase to 170°C, let sit for another 5 minutes, then increase to 180°C.

IF SAMPLE IS SENSITIVE TO BUBBLES:

h) Align the substrate with the heterostructure's position on the stamp. Push the stamp down until it reaches just the touch point, as seen in (c), being careful to not allow the stamp to move through the heterostructure.

i) Begin increasing the temperature of the stage in 10°C intervals. Wait for the stage to reach the set temperature, then increase the temperature by another 10°C. Continue this until the stage reaches 110°C, then slowly push the stamp down so that the heterostructure is smoothly pressed down onto the substrate, as in (d). Pushing through the heterostructure at this higher temperature enables bubbles to be pushed out from the heterostructure, so make sure this goes as slowly and smoothly as possible.

Continue increasing the temperature until the stage reaches 160°C, let the stage sit at that temperature for 5 minutes, increase to 170°C, let sit for another 5 minutes, then increase to 180°C.

FOR BOTH CASES:

j) Once the stage reaches 180°C, very slightly wiggle the X movement. If the edges of the PC on the substrate move but the heterostructure remains unmoved, this means the PC has fully melted. Lift up the stamp rapidly, and when it is fully raised, turn off the temperature control. Let the stage come to room temperature before removing the flake. The melted PC can be removed by placing the chip in chloroform for 20 minutes to an hour at least 12 hours after the melting process.

Appendix C

ADDITIONAL DATA: EXCITON TRANSPORT

Table C.1: The simulated piezoelectric field at 10 nm above the LiNbO3 substrate with the top ITO electrode with SAW power of 1 mW/μm. The ITO layer can provide an efficient screening of the in-plane field component for the SAW with different wavelengths.

λ (μm)	0.6	1.2	1.8	2.4	3	3.6
f (GHz)	5.8568	2.9242	1.9497	1.4626	1.1703	0.97539
E_z (V/nm)	0.082	0.076	0.059	0.048	0.040	0.035
E_r (V/nm)	8.6×10^{-3}	4×10^{-3}	2.1×10^{-3}	1.3×10^{-3}	8.5×10^{-4}	6.1×10^{-4}

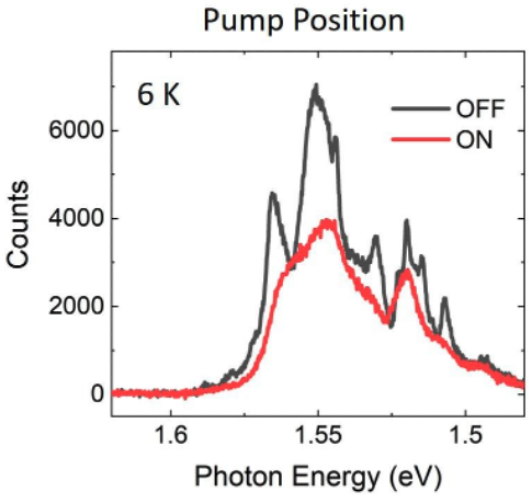

Figure C.1: Emission spectrum at the pump position when T = 6 K. When the SAW is on, all the sharp emission resonances disappear due to delocalization of the excitons and reduced coupling with localized phonon modes.

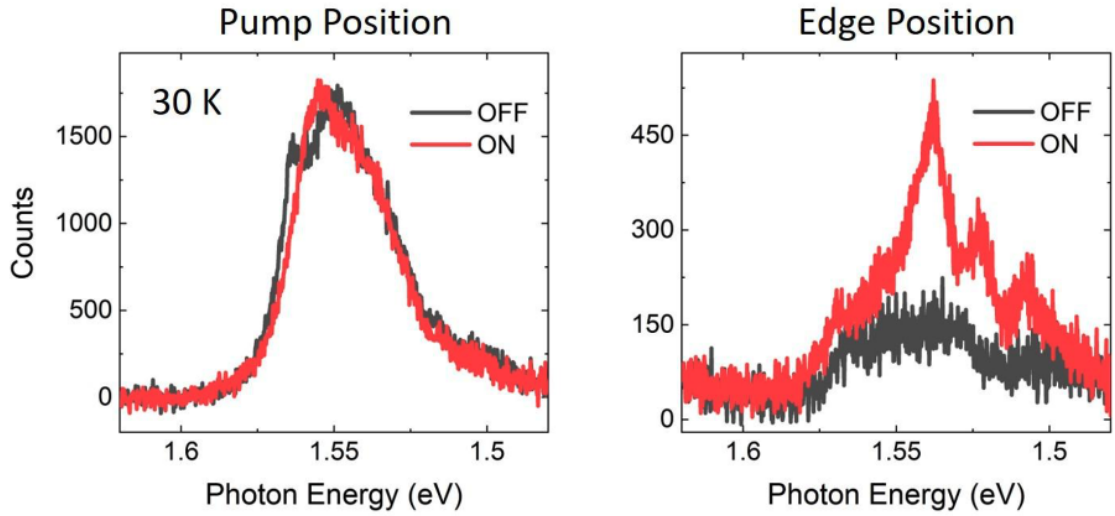

Figure C.2: The emission spectrum at the pump (a) and edge (b) position when T=30 K.

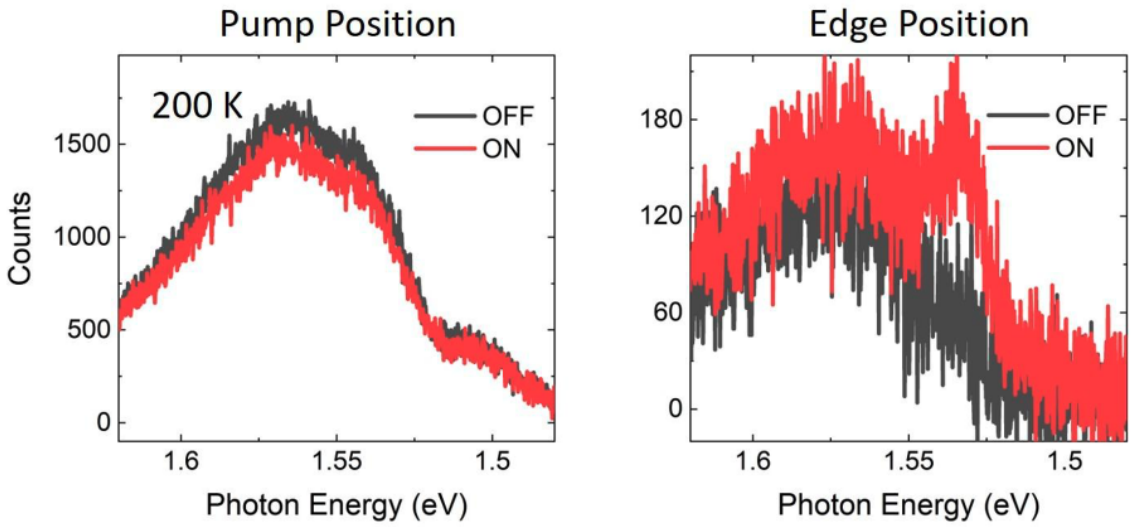

Figure C.3: The emission spectrum at the pump (a) and edge (b) position when T=200 K.

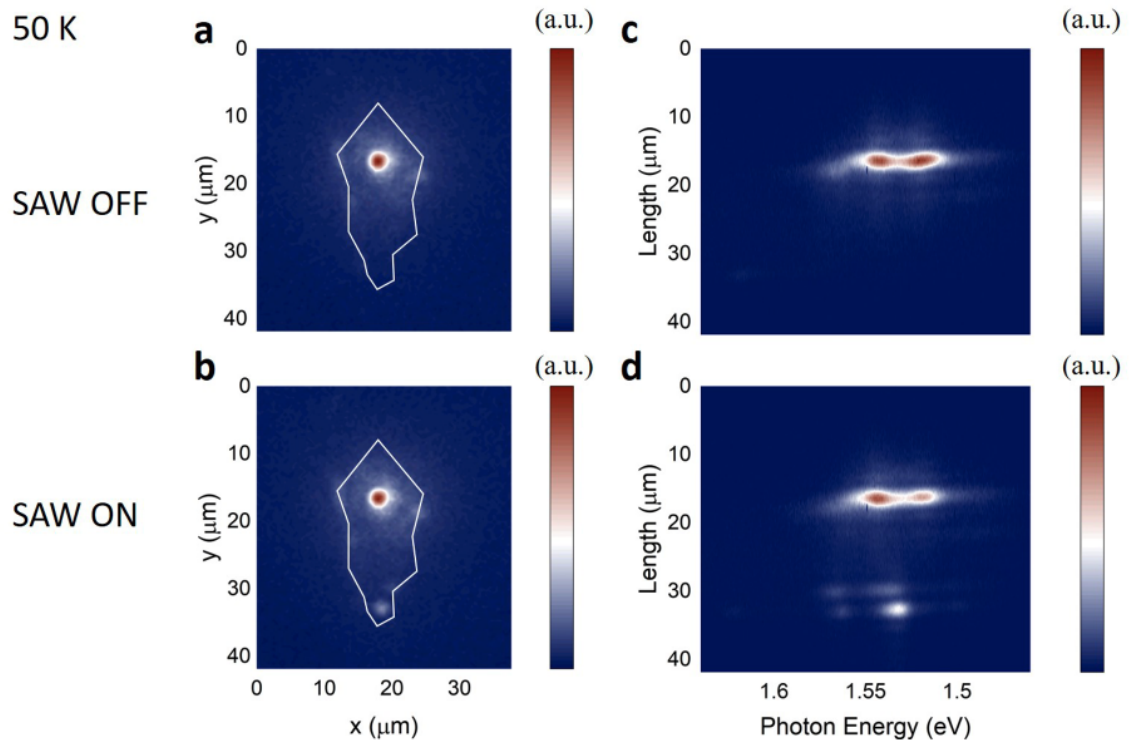

Figure C.4: Exciton transport at 50 K with (a) SAW off and (b) SAW on. The left panels show the spatial PL, while the right panels show the spectral PL.

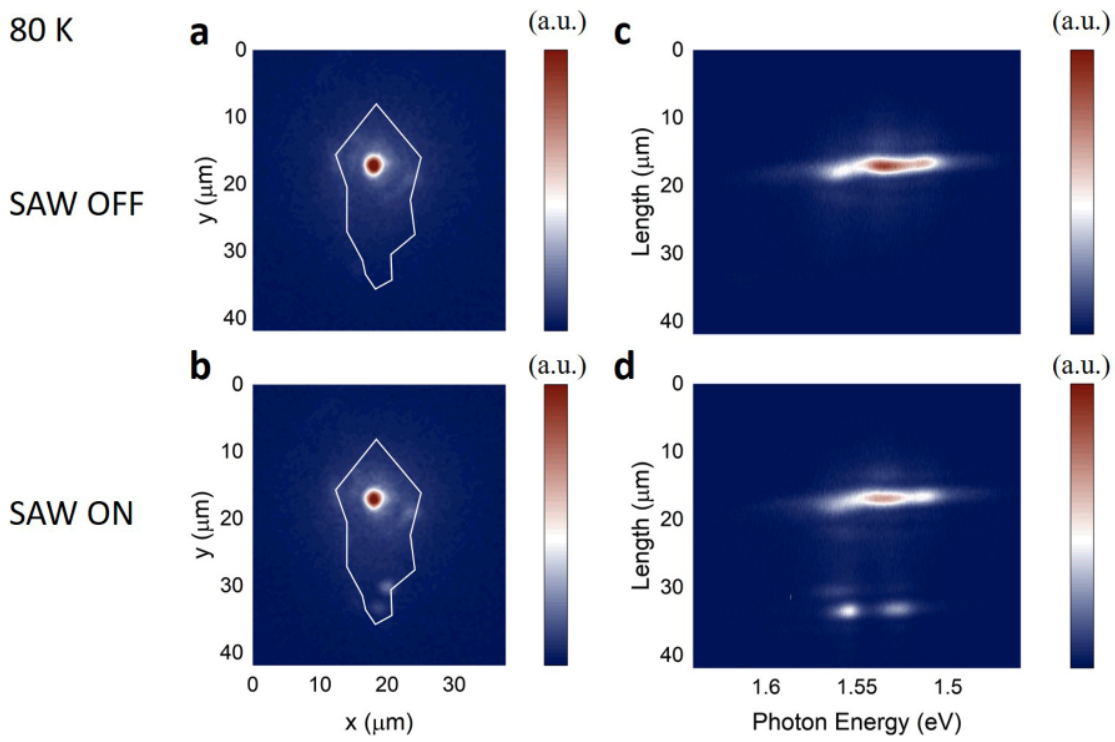

Figure C.5: Exciton transport at 80 K with (a) SAW off and (b) SAW on. The left panels show the spatial PL, while the right panels show the spectral PL.

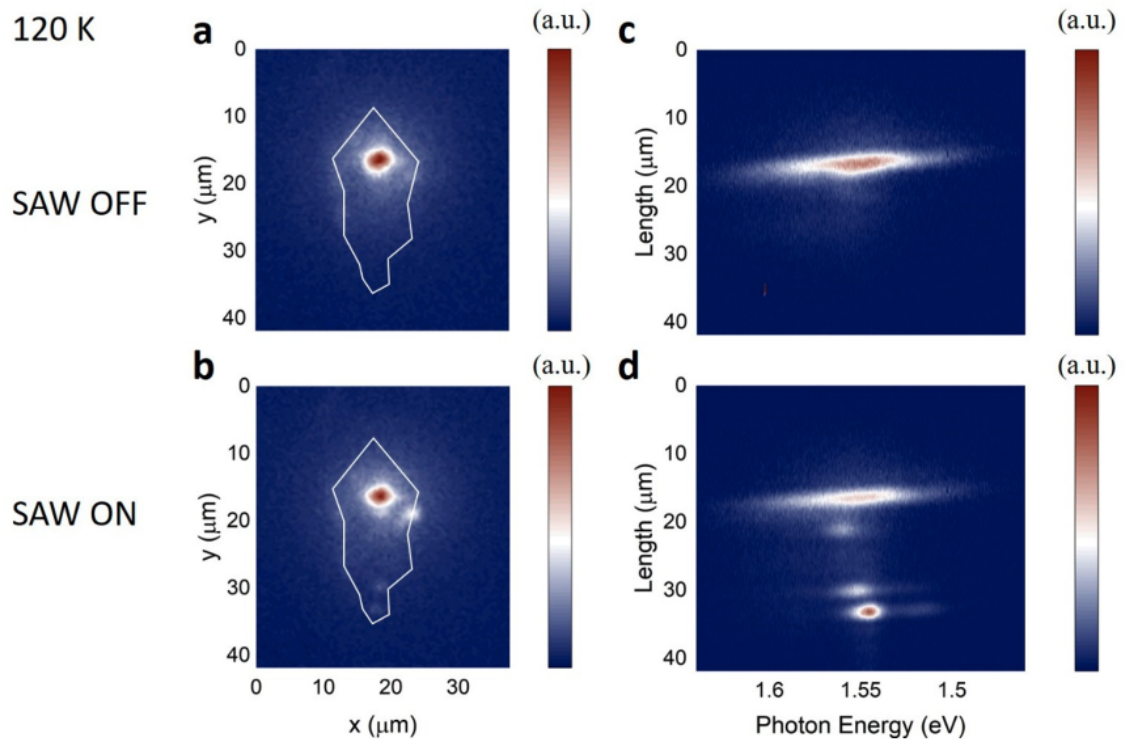

Figure C.6: Exciton transport at 120 K with (a) SAW off and (b) SAW on. The left panels show the spatial PL, while the right panels show the spectral PL.

Appendix D

ADDITIONAL DATA: QUANTUM EMITTERS

Table D.1: Quantum Emitter Characteristics

Emitter	Device	Energy tuning (meV)	Min Energy (meV)	Max Energy (meV)	Dipole moment (e·nm)	Transition	Phonon Lines
QE1	A	6.35	1547.0	1553.4	0.341	KΓ	yes
QE3	A	11.5	1520.0	1531.5	0.649	KK	yes
QE4	A	6.26	1549.9	1556.2	0.377	KΓ	yes
QE5	A	9.75	1490.6	1500.4	0.668	KK	no
QE6	A	6.96	1522.2	1529.2	0.622	KK	yes
QE7	B	11.6	1543.8	1555.4	0.599	KK	yes
QE8	B	12.8	1494.2	1507.0	0.321	KΓ	no
QE9	B	11.6	1555.1	1566.7	0.331	KΓ	yes
QE10	B	6.20	1538.3	1544.5	0.586	KK	no
QE11	B	8.94	1595.8	1604.8	0.357	KΓ	no
QE12	B	5.20	1540.2	1545.4	0.315	KΓ	yes
QE13	E	7.90	1544.6	1552.5	0.459	QK	yes
QE14	E	8.67	1535.8	1544.5	0.480	QK	no
QE15	E	5.46	1525.4	1530.8	0.493	QK	yes
QE16	E	8.26	1545.8	1554.1	0.455	QK	yes
QE17	E	8.65	1520.6	1529.2	0.609	KK	yes
QE18	C	8.61	1494.1	1502.7	0.370	KΓ	no
QE19	C	20.2	1534.2	1554.5	0.657	KK	yes
QE20	D	8.43	1502.8	1511.3	0.471	QK	no

Table D.2: Linewidth tuning of select intralayer quantum emitters.

Emitter	**Device**	**Type**	**Linewidth Tuning Range (meV)**	**Min Linewidth (meV)**	**Max Linewidth (meV)**
QE2	C	intralayer	0.53	0.94	1.45
QE21	D	intralayer	0.73	1.62	2.37
QE22	D	intralayer	0.39	1.95	2.34

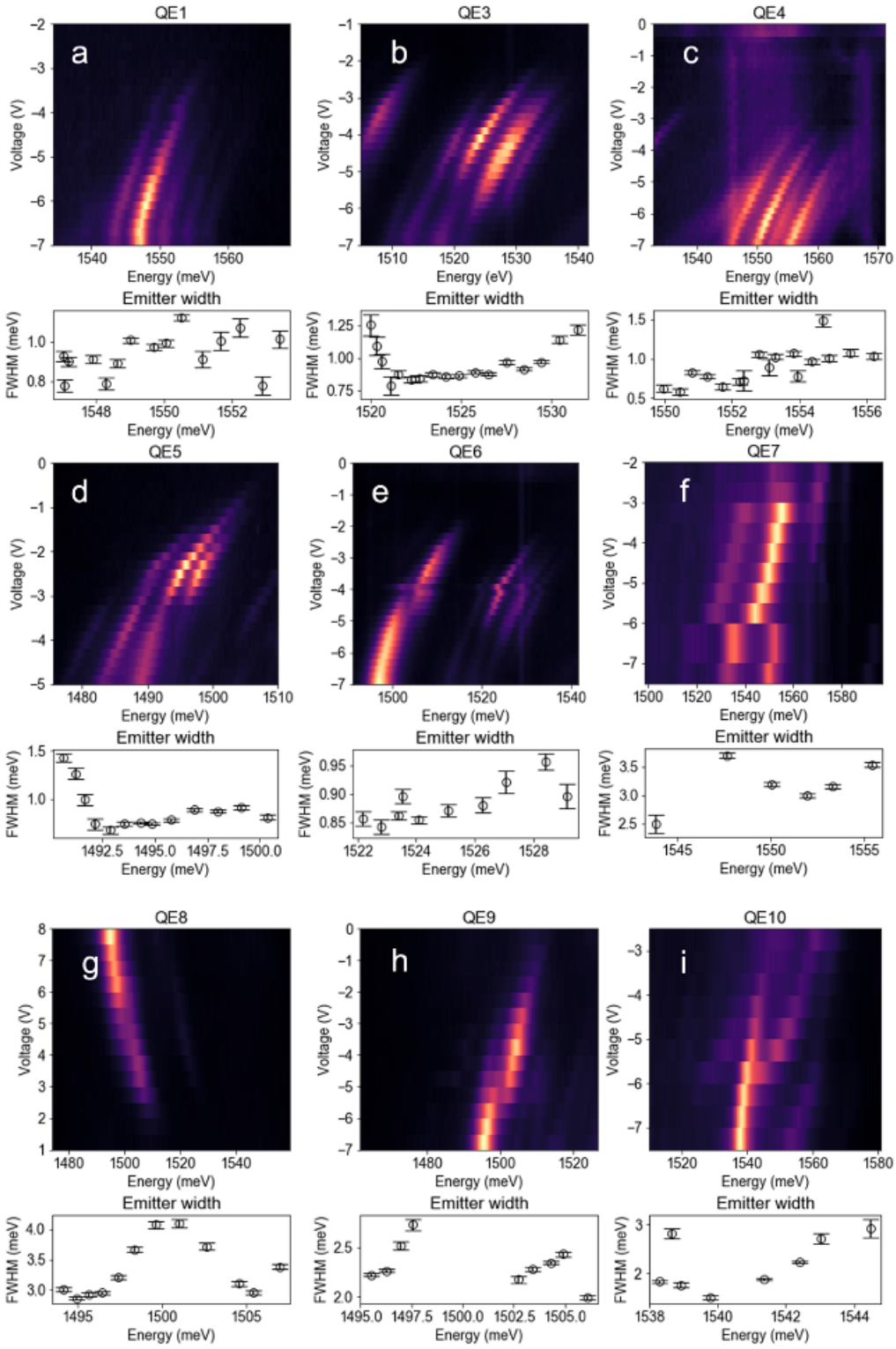

Figure D.1: PL spectra, voltage tuning, and linewidth (FMCW) of nineteen IX QEs that have been measured, (1/3)

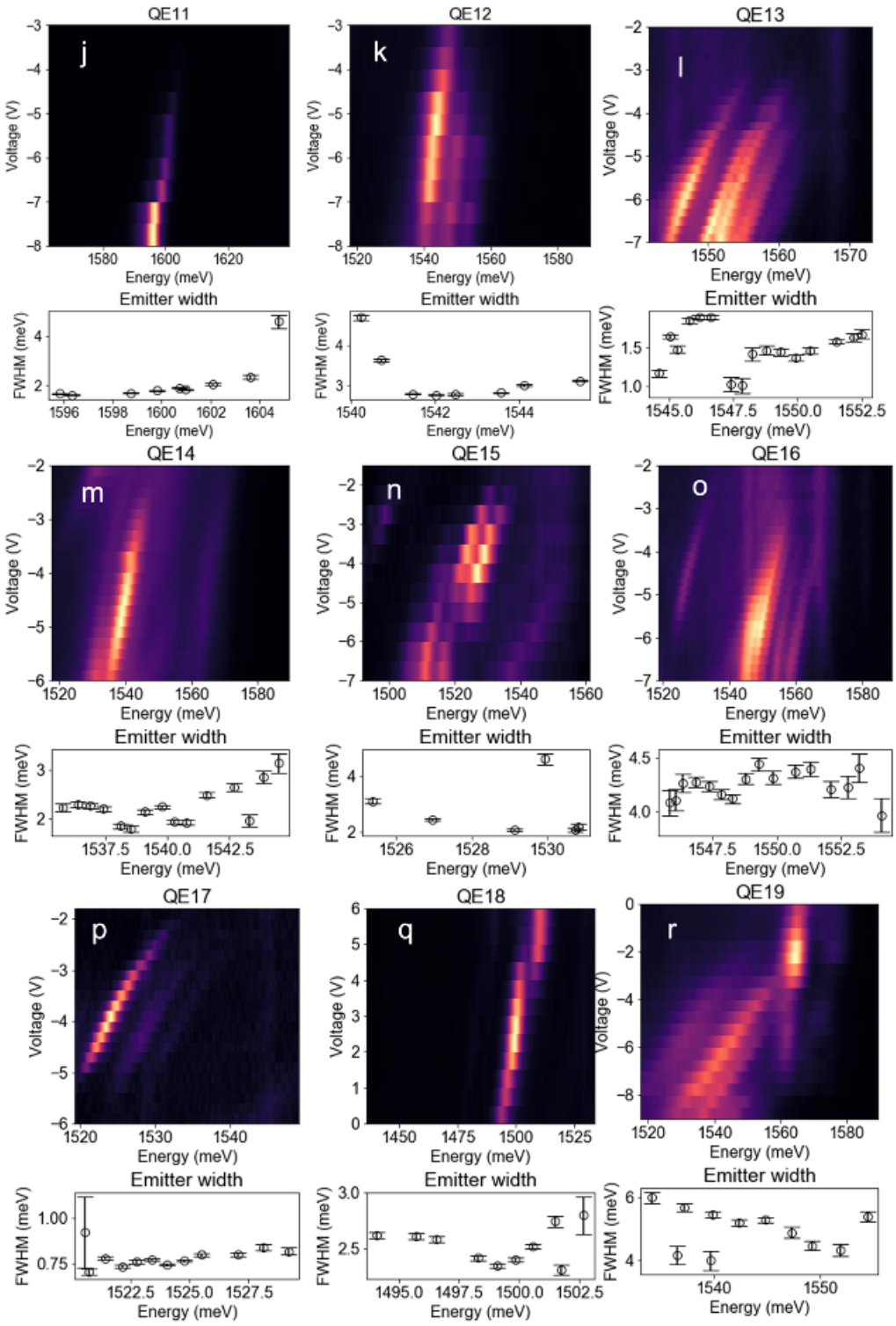

Figure D.2: PL spectra, voltage tuning, and linewidth (FMCW) of nineteen IX QEs that have been measured, (2/3)

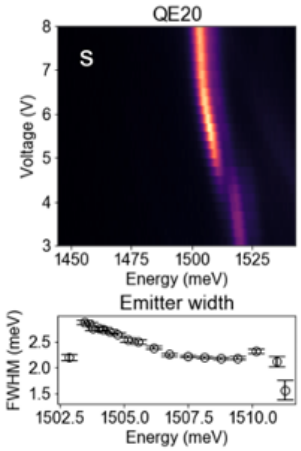

Figure D.3: PL spectra, voltage tuning, and linewidth (FMCW) of nineteen IX QEs that have been measured, (3/3)

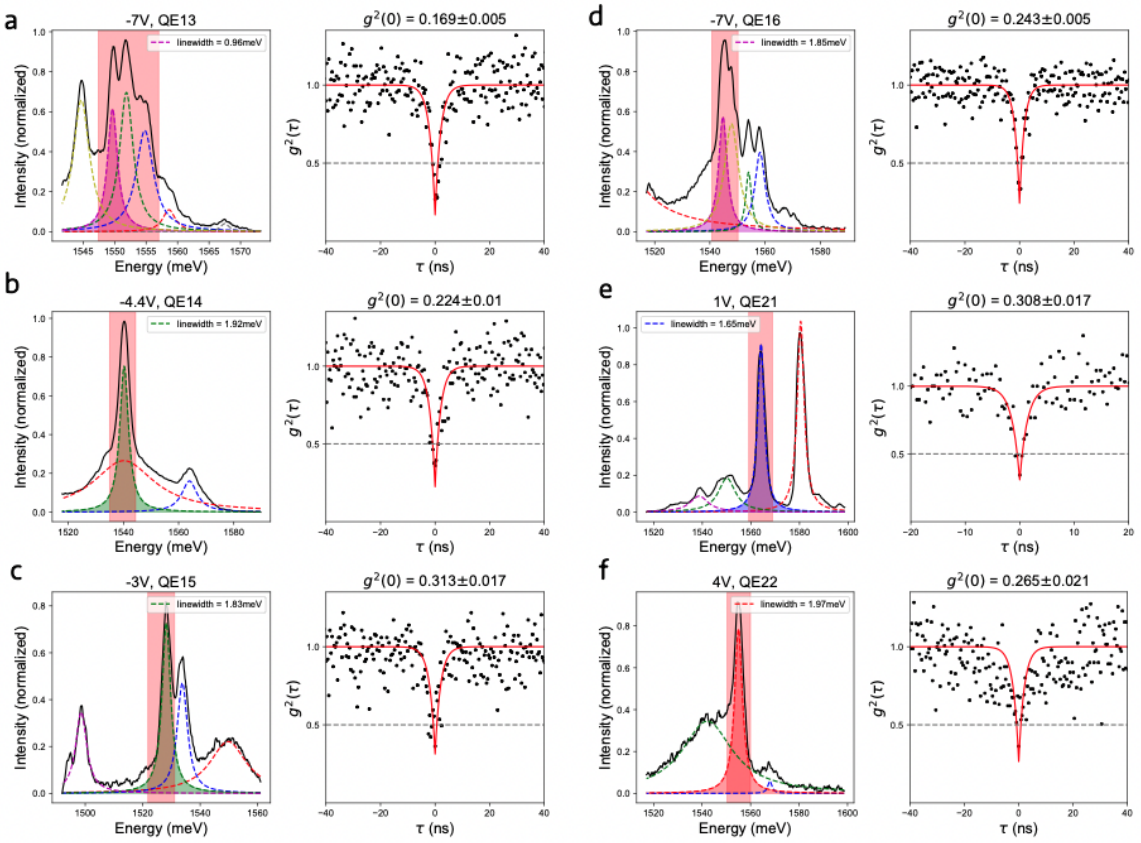

Figure D.4: Photoluminescence spectra and second-order correlation $g(^{2})$ measurements of six 2D emitters. QE13 to 16 are IX emitters, while QE21 and 22 are intralayer exciton emitters. They all show anti-bunching with $g^{(2)}(0) < 0.5$ and a linewidth less than 2.0 meV. Left: PL spectra (black) of emitters. The dashed lines are Lorentzian fittings. The passband of the tunable filter used in the $g^{(2)}$ measurements is indicated with the red shaded area. Right: $g^{(2)}$ measurements of the emitters. The low $g^{(2)}(0)$ values show their single-photon characteristics with high purity.

Table D.3: The Huang-Rhys parameter and phonon line spacings extracted from the PL spectra of eleven IX QEs.

Emitter	**Huang-Rhys Parameter**	**Phonon line spacing in energy**
QE1	$S = 6.15 \pm 0.47$	$n = 1 \rightarrow 2$: 3.00 meV
		$n = 2 \rightarrow 3$: 3.32 meV
		$n = 3 \rightarrow 4$: 3.71 meV
		$n = 4 \rightarrow 5$: 3.70 meV
QE3	$S = 1.32 \pm 0.39$	$n = 0 \rightarrow 1$: 4.19 meV
		$n = 1 \rightarrow 2$: 5.10 meV
		$n = 2 \rightarrow 3$: 3.70 meV
		$n = 3 \rightarrow 4$: 3.76 meV
QE4	$S = 1.64 \pm 0.54$	$n = 1 \rightarrow 2$: 3.10 meV
		$n = 2 \rightarrow 3$: 2.63 meV
		$n = 3 \rightarrow 4$: 4.43 meV
QE6	$S = 2.64 \pm 0.15$	$n = 0 \rightarrow 1$: 4.14 meV
		$n = 1 \rightarrow 2$: 5.15 meV
		$n = 2 \rightarrow 3$: 4.07 meV
QE9	$S = 3.55 \pm 0.61$	$n = 2 \rightarrow 3$: 8.31 meV
		$n = 3 \rightarrow 4$: 6.24 meV
		$n = 4 \rightarrow 5$: 7.25 meV
QE12	$S = 5.93 \pm 0.37$	$n = 1 \rightarrow 2$: 3.04 meV
		$n = 2 \rightarrow 3$: 2.81 meV
QE13	$S = 5.22 \pm 0.64$	$n = 1 \rightarrow 2$: 3.89 meV
		$n = 2 \rightarrow 3$: 2.90 meV
		$n = 3 \rightarrow 4$: 2.30 meV
QE15	$S = 1.83 \pm 0.09$	$n = 1 \rightarrow 2$: 5.31 meV
		$n = 2 \rightarrow 3$: 6.33 meV
QE16	$S = 9.91 \pm 0.76$	$n = 4 \rightarrow 5$: 4.16 meV
		$n = 5 \rightarrow 6$: 6.14 meV
		$n = 6 \rightarrow 7$: 3.15 meV
QE17	$S = 4.81 \pm 0.38$	$n = 0 \rightarrow 1$: 5.46 meV
		$n = 1 \rightarrow 2$: 8.31 meV
QE19	$S = 5.77 \pm 0.39$	$n = 0 \rightarrow 1$: 8.59 meV
		$n = 1 \rightarrow 2$: 7.50 meV
		$n = 2 \rightarrow 3$: 8.48 meV

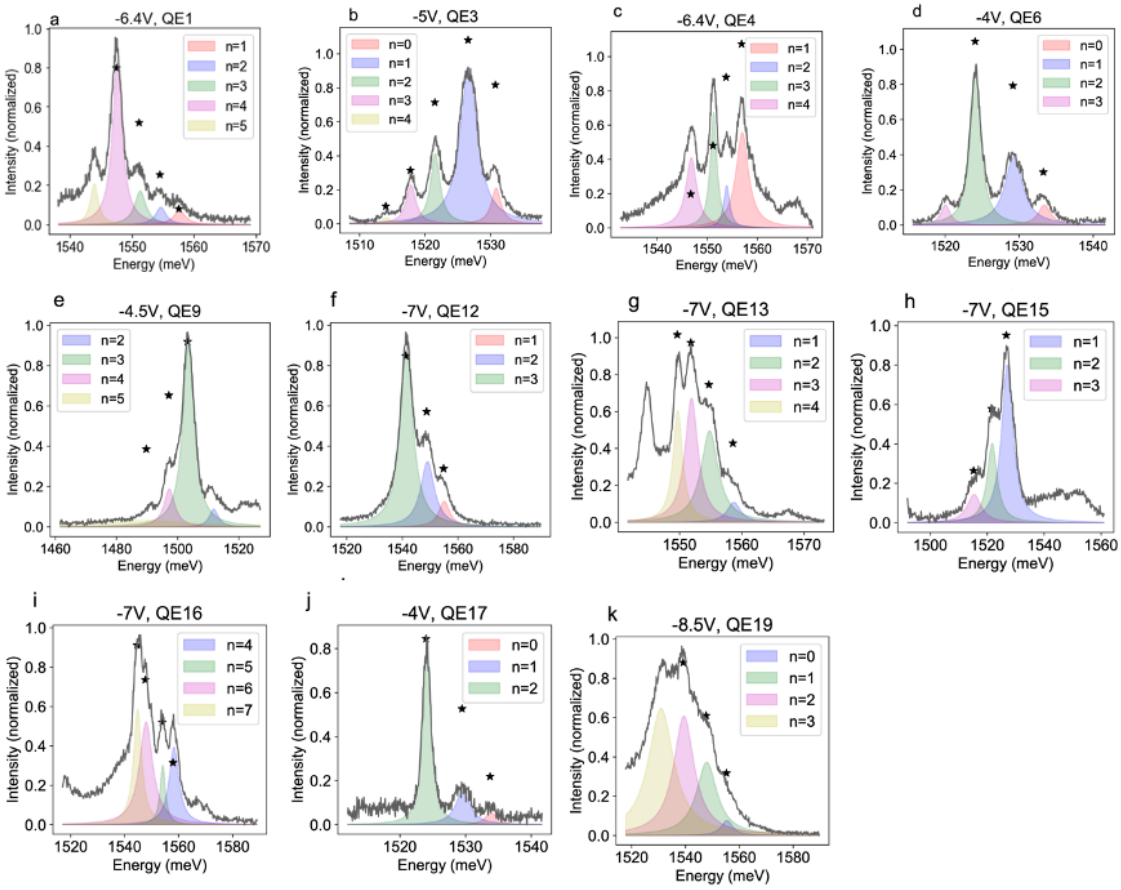

Figure D.5: Additional data of phonon lines in IX QEs coupled to interlayer breathing mode phonons. Each peak is fit with a Lorentzian function shown as shaded areas. The amplitude of each peak was fit with a Poisson function to extract the Huang-Rhys parameter, shown as black stars.

Table D.4: The phonon lines in IX QEs coupled to the higher-energy phonon mode.

Emitter	**Huang-Rhys Parameter**	**Phonon line spacing in energy**
QE7	$S = 5.92 \pm 0.34$	$n = 1 \rightarrow 2$: 15.58 meV
		$n = 2 \rightarrow 3$: 14.73 meV
		$n = 3 \rightarrow 4$: 10.77 meV
		$n = 4 \rightarrow 5$: 16.14 meV

Table D.5: The energy spacing between phonon lines of intralayer exciton in QEs.

Emitter	**Huang-Rhys Parameter**	**Peak-to-peak energy spacing**
QE2	$S = 5.24 \pm 0.60$	$n = 1 \rightarrow 2$: 5.53 meV
		$n = 2 \rightarrow 3$: 5.15 meV
		$n = 3 \rightarrow 4$: 6.61 meV
QE21	$S = 1.59 \pm 0.26$	$n = 1 \rightarrow 2$: 16.36 meV
		$n = 2 \rightarrow 3$: 13.31 meV
		$n = 3 \rightarrow 4$: 11.87 meV
		$n = 4 \rightarrow 5$: 7.53 meV

Appendix E

ADDITIONAL DATA: EXCITON CONTROL WITH SAW RESONATORS

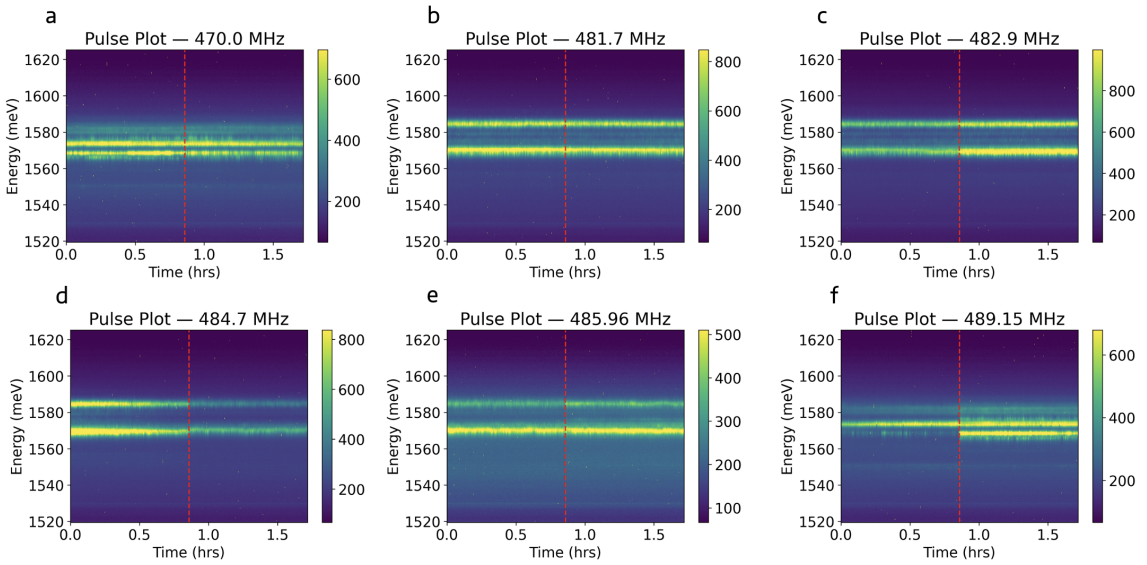

Figure E.1: PL before and after applying a SAW pulse at different frequencies. The PL is collected before the SAW turns on, then a single SAW pulse is sent (red dashed line), and the PL is monitored after. The SAW pulse sent is at a) $f = 470$ MHz, b) $f = 481.7$ MHz, c) $f = 482.9$ MHz, d) $f = 484.7$ MHz, e) $f = 485.96$ MHz, and f) $f = 489.15$ MHz.

BIBLIOGRAPHY

[1] In: *AAAS Articles DO Group* (Oct. 2021). DOI: 10.1126/article.29824.

[2] Nathan P. Wilson et al. "Excitons and emergent quantum phenomena in stacked 2D semiconductors". In: *Nature* 599.7885 (Nov. 2021), pp. 383–392. DOI: 10.1038/s41586-021-03979-1.

[3] Neil W. Ashcroft and N. David Mermin. *Solid state physics*. Saunders College, 1988.

[4] Valeri N. Kotov et al. "Electron-electron interactions in graphene: Current status and Perspectives". In: *Reviews of Modern Physics* 84.3 (July 2012), pp. 1067–1125. DOI: 10.1103/revmodphys.84.1067.

[5] Aleksandr Rodin et al. "Collective excitations in 2D materials". In: *Nature Reviews Physics* 2.10 (Sept. 2020), pp. 524–537. DOI: 10.1038/s42254-020-0214-4.

[6] Xiaolong Liu and Mark C. Hersam. "2D materials for Quantum Information Science". In: *Nature Reviews Materials* 4.10 (Aug. 2019), pp. 669–684. DOI: 10.1038/s41578-019-0136-x.

[7] Artur Branny et al. "Deterministic strain-induced arrays of quantum emitters in a two-dimensional semiconductor". In: *Nature Communications* 8.1 (May 2017). DOI: 10.1038/ncomms15053.

[8] Heonjoon Park et al. "Observation of fractionally quantized anomalous Hall effect". In: *Nature* 622.7981 (Aug. 2023), pp. 74–79. DOI: 10.1038/s41586-023-06536-0.

[9] Sajedeh Manzeli et al. “2D transition metal dichalcogenides”. In: *Nature Reviews Materials* 2.8 (June 2017). DOI: 10.1038/natrevmats.2017.33.

[10] John R. Schaibley et al. “Valleytronics in 2D materials”. In: *Nature Reviews Materials* 1.11 (Aug. 2016). DOI: 10.1038/natrevmats.2016.55.

[11] Xiao-Xiao Zhang et al. “Experimental evidence for dark excitons in Monolayer WSe2”. In: *Physical Review Letters* 115.25 (Dec. 2015). DOI: 10.1103/physrevlett.115.257403.

[12] Zhipeng Li et al. “Emerging photoluminescence from the dark-exciton phonon replica in Monolayer WSe2”. In: *Nature Communications* 10.1 (June 2019). DOI: 10.1038/s41467-019-10477-6.

[13] Alberto Ciarrocchi et al. “Excitonic devices with van der waals heterostructures: Valleytronics meets Twistronics”. In: *Nature Reviews Materials* 7.6 (Jan. 2022), pp. 449–464. DOI: 10.1038/s41578-021-00408-7.

[14] Alberto Ciarrocchi et al. “Polarization switching and electrical control of interlayer excitons in two-dimensional van der waals heterostructures”. In: *Nature Photonics* 13.2 (Dec. 2018), pp. 131–136. DOI: 10.1038/s41566-018-0325-y.

[15] Fedele Tagarelli et al. “Electrical control of hybrid exciton transport in a van der waals heterostructure”. In: *Nature Photonics* 17.7 (Apr. 2023), pp. 615–621. DOI: 10.1038/s41566-023-01198-w.

[16] Burak Aslan, Minda Deng, and Tony F. Heinz. “Strain tuning of excitons in Monolayer WSe2”. In: *Physical Review B* 98.11 (Sept. 2018). DOI: 10.1103/physrevb.98.115308.

[17] Sheng Yu et al. “Phase transition, effective mass and carrier mobility of mos2 monolayer under tensile strain”. In: *Applied Surface Science* 325 (Jan. 2015), pp. 27–32. DOI: 10.1016/j.apsusc.2014.11.079.

[18] A. M. Dadgar et al. “Strain engineering and Raman spectroscopy of monolayer transition metal dichalcogenides”. In: *Chemistry of Materials* 30.15 (July 2018), pp. 5148–5155. DOI: 10.1021/acs.chemmater.8b01672.

[19] Julien Chaste et al. “Intrinsic properties of suspended MoS2 on SiO2/Si pillar arrays for nanomechanics and optics”. In: *ACS Nano* 12.4 (Mar. 2018), pp. 3235–3242. DOI: 10.1021/acsnano.7b07689.

[20] John Cenker et al. “Reversible strain-induced magnetic phase transition in a van der waals magnet”. In: *Nature Nanotechnology* 17.3 (Jan. 2022), pp. 256–261. DOI: 10.1038/s41565-021-01052-6.

[21] Xin Zhang et al. “Dynamically-enhanced strain in atomically thin resonators”. In: *Nature Communications* 11.1 (Nov. 2020). DOI: 10.1038/s41467-020-19261-3.

[22] Lord Rayleigh. “On waves propagated along the surface of an elastic solid”. In: *Proceedings of the London Mathematical Society* 17.4 (1885).

[23] D.P. Morgan. “History of SAW devices”. In: *Proceedings of the 1998 IEEE International Frequency Control Symposium (Cat. No.98CH36165)* (1998), pp. 439–460. DOI: 10.1109/freq.1998.717937.

[24] R. M. White and F. W. Voltmer. “Direct piezoelectric coupling to surface elastic waves”. In: *Applied Physics Letters* 7.12 (Dec. 1965), pp. 314–316. DOI: 10.1063/1.1754276.

[25] David Morgan. *Surface acoustic wave filters*. 2nd ed. Academic Press, 2010.

[26] Supriyo Datta. *Surface acoustic wave devices*. Prentice-Hall, 1986.

[27] Shunsuke Ota et al. “Suppression of electromagnetic crosstalk by differential excitation for saw generation”. In: *Applied Physics Express* 17.2 (Feb. 2024), p. 022002. DOI: 10.35848/1882-0786/ad253f.

[28] D.L.T. Bell and R.C.M. Li. "Surface-acoustic-wave resonators". In: *Proceedings of the IEEE* 64.5 (1976), pp. 711–721. DOI: 10.1109/proc.1976.10200.

[29] Ruoming Peng et al. "Long-range transport of 2D excitons with acoustic waves". In: *Nature Communications* 13.1 (Mar. 2022). DOI: 10.1038/s41467-022-29042-9.

[30] Adina Ripin et al. "Tunable phononic coupling in excitonic quantum emitters". In: *Nature Nanotechnology* 18.9 (June 2023), pp. 1020–1026. DOI: 10.1038/s41565-023-01410-6.

[31] R. C. Miller et al. "Observation of the excited level of excitons in GaAs quantum wells". In: *Phys. Rev. B* 24 (1981), pp. 1134–1136.

[32] R. C. Miller and D. A. Kleinman. "Excitons in GaAs quantum wells". In: *J. Lumin.* 30 (1985), pp. 520–540.

[33] P. Rivera et al. "Interlayer valley excitons in heterobilayers of transition metal dichalcogenides". In: *Nat. Nanotechnol.* 13 (2018), pp. 1004–1015.

[34] S. Bar-Ad and I. Bar-Joseph. "Exciton spin dynamics in GaAs heterostructures". In: *Phys. Rev. Lett.* 68 (1992), pp. 349–352.

[35] A. A. High et al. "Control of exciton fluxes in an excitonic integrated circuit". In: *Science* 321 (2008), pp. 229–231.

[36] Luis A. Jauregui et al. "Electrical control of interlayer exciton dynamics in atomically thin heterostructures". In: *Science* 366.6467 (Nov. 2019), pp. 870–875. DOI: 10.1126/science.aaw4194.

[37] D. Unuchek et al. "Room-temperature electrical control of exciton flux in a van der Waals heterostructure". In: *Nature* 560 (2018), pp. 340–344.

[38] J. A. Brum and G. Bastard. "Electric-field-induced dissociation of excitons in semiconductor quantum wells". In: *Phys. Rev. B* 31 (1985), pp. 3893–3898.

[39] C. Rocke et al. “Exciton ionization in a quantum well studied by surface acoustic waves”. In: *Phys. Rev. B* 57 (1998), R6850–R6853.

[40] J. Hegarty, L. Goldner, and M. D. Sturge. “Localized and delocalized two-dimensional excitons in GaAs-AlGaAs multiple-quantum-well structures”. In: *Phys. Rev. B* 30 (1984), pp. 7346–7348.

[41] A. Gärtner et al. “Drift mobility of long-living excitons in coupled GaAs quantum wells”. In: *Appl. Phys. Lett.* 89 (2006), p. 052108.

[42] F. Cadiz et al. “Exciton diffusion in WSe2 monolayers embedded in a van der Waals heterostructure”. In: *Appl. Phys. Lett.* 112 (2018), p. 152106.

[43] M. Kulig et al. “Exciton diffusion and halo effects in monolayer semiconductors”. In: *Phys. Rev. Lett.* 120 (2018), p. 207401.

[44] A. Javey et al. “Neutral exciton diffusion in monolayer MoS2”. In: *ACS Nano* 14 (2020), pp. 13433–13440.

[45] P. Delsing et al. “The 2019 surface acoustic waves roadmap”. In: *J. Phys. D: Appl. Phys.* 52 (2019), p. 353001.

[46] A. Violante et al. “Dynamics of indirect exciton transport by moving acoustic fields”. In: *New J. Phys.* 16 (2014), p. 033035.

[47] J. Rudolph, R. Hey, and P. V. Santos. “Long-range exciton transport by dynamic strain fields in a GaAs quantum well”. In: *Phys. Rev. Lett.* 99 (2007), p. 047602.

[48] C. Rocke et al. “Acoustically driven storage of light in a quantum well”. In: *Phys. Rev. Lett.* 78 (1997), pp. 4099–4102.

[49] E. A. Cerda-Méndez et al. “Polariton condensation in dynamic acoustic lattices”. In: *Phys. Rev. Lett.* 105 (2010), p. 116402.

[50] S. Tarucha et al. “Exciton binding energy in GaAs quantum wells deduced from magneto-optical absorption measurement”. In: *Solid State Commun.* 52 (1984), pp. 815–819.

[51] F. Withers et al. “WSe2 light-emitting tunneling transistors with enhanced brightness at room temperature”. In: *Nano Lett.* 15 (2015), pp. 8223–8228.

[52] B. Zhu, X. Chen, and X. Cui. “Exciton binding energy of monolayer WS2”. In: *Sci. Rep.* 5 (2015), p. 9218.

[53] N. Lundt et al. “Room-temperature Tamm-plasmon exciton-polaritons with a WSe2 monolayer”. In: *Nat. Commun.* 7 (2016), p. 13328.

[54] Y. Liu et al. “Room temperature nanocavity laser with interlayer excitons in 2D heterostructures”. In: *Sci. Adv.* 5 (2019), eaav4506.

[55] F. Xia et al. “Two-dimensional material nanophotonics”. In: *Nat. Photonics* 8 (2014), pp. 899–907.

[56] S. Wu et al. “Monolayer semiconductor nanocavity lasers with ultralow thresholds”. In: *Nature* 520 (2015), pp. 69–72.

[57] L. Zhang et al. “Photonic-crystal exciton-polaritons in monolayer semiconductors”. In: *Nat. Commun.* 9 (2018), p. 713.

[58] Z. Wang et al. “Evidence of high-temperature exciton condensation in two-dimensional atomic double layers”. In: *Nature* 574 (2019), pp. 76–80.

[59] L. Zhang et al. “Van der Waals heterostructure polaritons with moiré-induced nonlinearity”. In: *Nature* 591 (2021), pp. 61–65.

[60] Z. Wang et al. “Electrical tuning of interlayer exciton gases in WSe2 bilayers”. In: *Nano Lett.* 18 (2018), pp. 137–143.

[61] K. L. Seyler et al. “Signatures of moiré-trapped valley excitons in MoSe2/WSe2 heterobilayers”. In: *Nature* 567 (2019), pp. 66–70.

[62] C. Jin et al. “Observation of moiré excitons in WSe2/WS2 heterostructure superlattices”. In: *Nature* 567 (2019), pp. 76–80.

[63] K. Tran et al. “Evidence for moiré excitons in van der Waals heterostructures”. In: *Nature* 567 (2019), pp. 71–75.

[64] P. Rivera et al. “Observation of long-lived interlayer excitons in monolayer MoSe2-WSe2 heterostructures”. In: *Nat. Commun.* 6 (2015), p. 6242.

[65] N. Peimyoo et al. “Electrical tuning of optically active interlayer excitons in bilayer MoS2”. In: *Nat. Nanotechnol.* 16 (2021), pp. 888–893.

[66] D. Unuchek et al. “Valley-polarized exciton currents in a van der Waals heterostructure”. In: *Nat. Nanotechnol.* 14 (2019), pp. 1104–1109.

[67] Y. Liu et al. “Electrically controllable router of interlayer excitons”. In: *Sci. Adv.* 6 (2020), eaba1830.

[68] B. Radisavljevic et al. “Single-layer MoS2 transistors”. In: *Nat. Nanotechnol.* 6 (2011), pp. 147–150.

[69] L. A. Jauregui et al. “Electrical control of interlayer exciton dynamics in atomically thin heterostructures”. In: *Science* 366 (2019), pp. 870–875.

[70] D. Rhodes et al. “Disorder in van der Waals heterostructures of 2D materials”. In: *Nat. Mater.* 18 (2019), pp. 541–549.

[71] A. R. Rezk et al. “Acoustic-excitonic coupling for dynamic photoluminescence manipulation of Quasi-2D MoS2 nanoflakes”. In: *Adv. Opt. Mater.* 3 (2015), pp. 888–894.

[72] A. R. Rezk et al. “Acoustically-driven trion and exciton modulation in piezoelectric two-dimensional MoS2”. In: *Nano Lett.* 16 (2016), pp. 849–855.

[73] K. Datta et al. “Piezoelectric modulation of excitonic properties in monolayer WSe2 under strong dielectric screening”. In: *ACS Nano* 15 (2021), pp. 12334–12341.

[74] A. M. Jones et al. “Spin-layer locking effects in optical orientation of exciton spin in bilayer WSe2”. In: *Nat. Phys.* 10 (2014), pp. 130–134.

[75] J. Lindlau et al. “The role of momentum-dark excitons in the elementary optical response of bilayer WSe2”. In: *Nat. Commun.* 9 (2018), p. 2586.

[76] H. C. Kamban and T. G. Pedersen. “Interlayer excitons in van der Waals heterostructures: Binding energy, Stark shift, and field-induced dissociation”. In: *Sci. Rep.* 10 (2020), p. 5537.

[77] N. R. Wilson et al. “Determination of band offsets, hybridization, and exciton binding in 2D semiconductor heterostructures”. In: *Science Advances* 3 (2017), e1601832.

[78] P. V. Nguyen et al. “Visualizing electrostatic gating effects in two-dimensional heterostructures”. In: *Nature* 572 (2019), pp. 220–223.

[79] O. B. Aslan et al. “Strained bilayer WSe_2 with reduced exciton-phonon coupling”. In: *Physical Review B* 101 (2020), p. 115305.

[80] W. Fu et al. “Phononic integrated circuitry and spin–orbit interaction of phonons”. In: *Nat. Commun.* 10 (2019), p. 2743.

[81] F. M. Mayor et al. “Gigahertz phononic integrated circuits on thin-film lithium niobate on sapphire”. In: *Phys. Rev. Appl.* 15 (2021), p. 014039.

[82] Igor Aharonovich, Dirk Englund, and Milos Toth. “Solid-state single-photon emitters”. In: *Nature Photonics* 10.10 (Sept. 2016), pp. 631–641. DOI: 10.1038/nphoton.2016.186.

[83] F. Peyskens et al. “Integration of single photon emitters in 2D layered materials with a silicon nitride photonic chip”. In: *Nat. Commun.* 10 (2019), p. 4435.

[84] I. Aharonovich and M. Toth. “Quantum emitters in two dimensions”. In: *Science* 358 (2017), pp. 170–171.

[85] K. Parto et al. “Defect and strain engineering of monolayer WSe2 enables site-controlled single-photon emission up to 150 K”. In: *Nat. Commun.* 12 (2021), p. 3585.

[86] Shaimaa I. Azzam, Kamyar Parto, and Galan Moody. “Prospects and challenges of quantum emitters in 2D materials”. In: *Applied Physics Letters* 118.24 (June 2021). DOI: 10.1063/5.0054116.

[87] L. Linhart et al. “Localized intervalley defect excitons as single-photon emitters in WSe2”. In: *Phys. Rev. Lett.* 123 (2019), p. 146401.

[88] M. Aspelmeyer, T. J. Kippenberg, and F. Marquardt. “Cavity optomechanics”. In: *Rev. Mod. Phys.* 86 (2014), pp. 1391–1452.

[89] K. C. Lee et al. “Entangling macroscopic diamonds at room temperature”. In: *Science* 334 (2011), pp. 1253–1256.

[90] V. C. Vivoli et al. “Proposal for an optomechanical Bell test”. In: *Phys. Rev. Lett.* 116 (2016), p. 070405.

[91] S. Tarrago Velez et al. “Bell correlations between light and vibration at ambient conditions”. In: *Sci. Adv.* 6 (2020), eabb0260.

[92] M. Mirhosseini et al. “Superconducting qubit to optical photon transduction”. In: *Nature* 588 (2020), pp. 599–603.

[93] A. Bienfait et al. “Phonon-mediated quantum state transfer and remote qubit entanglement”. In: *Science* 364 (2019), pp. 368–371.

[94] C. Toninelli et al. “Single organic molecules for photonic quantum technologies”. In: *Nat. Mater.* 20 (2021), pp. 1615–1628.

[95] W. Chen et al. “Continuous-wave frequency upconversion with a molecular optomechanical nanocavity”. In: *Science* 374 (2021), pp. 1264–1267.

[96] C. Lee et al. “Anomalous lattice vibrations of single- and few-layer MoS2”. In: *ACS Nano* 4 (2010), pp. 2695–2700.

[97] Y. Zhao et al. “Interlayer breathing and shear modes in few-trilayer MoS2 and WSe2”. In: *Nano Lett.* 13 (2013), pp. 1007–1015.

[98] C. Palacios-Berraquero et al. “Large-scale quantum-emitter arrays in atomically thin semiconductors”. In: *Nat. Commun.* 8 (2017), p. 15093.

[99] L. Sortino et al. “Bright single photon emitters with enhanced quantum efficiency in a two-dimensional semiconductor coupled with dielectric nano-antennas”. In: *Nat. Commun.* 12 (2021), p. 6063.

[100] J. Kundrotas et al. “Impurity-induced Huang–Rhys factor in beryllium -doped GaAs/AlAs multiple quantum wells: fractional-dimensional space approach”. In: *Semicond. Sci. Technol.* 22 (2007), pp. 1070–1076.

[101] G. Grosso et al. “Low-temperature electron–phonon interaction of quantum emitters in hexagonal boron nitride”. In: *ACS Photonics* 7 (2020), pp. 1410–1417.

[102] D. Li et al. “Exciton–phonon coupling strength in single-layer MoSe2 at room temperature”. In: *Nat. Commun.* 12 (2021), p. 954.

[103] E. Ergeçen et al. “Magnetically brightened dark electron–phonon bound states in a van der Waals antiferromagnet”. In: *Nat. Commun.* 13 (2022), p. 98.

[104] T. Y. Jeong et al. “Coherent lattice vibrations in mono- and few-layer WSe2”. In: *ACS Nano* 10 (2016), pp. 5560–5566.

[105] M. M. Altaiary et al. “Electrically switchable intervalley excitons with strong two-phonon scattering in bilayer WSe2”. In: *Nano Lett.* 22 (2022), pp. 1829–1835.

[106] T. P. Darlington et al. “Imaging strain-localized excitons in nanoscale bubbles of monolayer WSe2 at room temperature”. In: *Nat. Nanotechnol.* 15 (2020), pp. 854–860.

[107] Y. Luo et al. “Exciton dipole orientation of strain-induced quantum emitters in WSe2”. In: *Nano Lett.* 20 (2020), pp. 5119–5126.

[108] Z. Huang et al. “Spatially indirect intervalley excitons in bilayer WSe2”. In: *Phys. Rev. B* 105 (2022), p. L041409.

[109] G. Scuri et al. “Electrically tunable valley dynamics in twisted WSe2/WSe2 bilayers”. In: *Phys. Rev. Lett.* 124 (2020), p. 217403.

[110] Y. Tang et al. “Tuning layer-hybridized moiré excitons by the quantum-confined Stark effect”. In: *Nat. Nanotechnol.* 16 (2021), pp. 52–57.

[111] S. B. Desai et al. “Strain-induced indirect to direct bandgap transition in multilayer WSe2”. In: *Nano Lett.* 14 (2014), pp. 4592–4597.

[112] C. Jin et al. “Interlayer electron–phonon coupling in WSe2/hBN heterostructures”. In: *Nat. Phys.* 13 (2017), pp. 127–131.

[113] I. Paradisanos et al. “Efficient phonon cascades in WSe2 monolayers”. In: *Nat. Commun.* 12 (2021), p. 538.

[114] P. Rivera et al. “Intrinsic donor-bound excitons in ultraclean monolayer semiconductors”. In: *Nat. Commun.* 12 (2021), p. 871.

[115] S. Kumar, A. Kaczmarczyk, and B. D. Gerardot. “Strain-induced spatial and spectral isolation of quantum emitters in mono- and bilayer WSe2”. In: *Nano Lett.* 15 (2015), pp. 7567–7573.

[116] H. Baek et al. “Highly energy-tunable quantum light from moiré-trapped excitons”. In: *Sci. Adv.* 6 (2020), eaba8526.

[117] S. Zhang et al. “Defect structure of localized excitons in a WSe2 monolayer”. In: *Phys. Rev. Lett.* 119 (2017), p. 046101.

[118] Y. J. Zheng et al. “Point defects and localized excitons in 2D WSe2”. In: *ACS Nano* 13 (2019), pp. 6050–6059.

[119] J.-Y. Tsai et al. “Antisite defect qubits in monolayer transition metal dichalcogenides”. In: *Nat. Commun.* 13 (2022), p. 492.

[120] M. Koperski et al. “Single photon emitters in exfoliated WSe2 structures”. In: *Nature Nanotechnology* 10 (2015), pp. 503–506.

[121] W. Li et al. “Dipolar interactions between localized interlayer excitons in van der Waals heterostructures”. In: *Nature Materials* 19 (2020), pp. 624–629.

[122] X. Lu et al. “Optical initialization of a single spin-valley in charged WSe2 quantum dots”. In: *Nat. Nanotechnol.* 14 (2019), pp. 426–431.

[123] L. Allen and J. Eberly. *Optical Resonance and Two-Level Atoms*. Dover, 1988.

[124] P. Tonndorf et al. “Single-photon emission from localized excitons in an atomically thin semiconductor”. In: *Optica* 2 (2015), p. 347.

[125] F. Barati et al. “Vibronic exciton–phonon states in stack-engineered van der Waals heterojunction photodiodes”. In: *Nano Lett.* 22 (2022), pp. 5751–5758.

[126] M. Grzeszczyk et al. “Breathing modes in few-layer MoTe2 activated by h-BN encapsulation”. In: *Appl. Phys. Lett.* 116 (2020), p. 191601.

[127] A. M. Kelley. “Exciton-optical phonon coupling in II-VI semiconductor nanocrystals”. In: *The Journal of Chemical Physics* 151 (2019), p. 140901.

[128] I. Yeo et al. “Strain-mediated coupling in a quantum dot–mechanical oscillator hybrid system”. In: *Nat. Nanotechnol.* 9 (2014), pp. 106–110.

[129] T. Devakul et al. “Magic in twisted transition metal dichalcogenide bilayers”. In: *Nat. Commun.* 12 (2021), p. 6730.

[130] C. Galland et al. “Heralded single-phonon preparation, storage, and readout in cavity optomechanics”. In: *Phys. Rev. Lett.* 112 (2014), p. 143602.

[131] M. D. Anderson et al. “Two-color pump–probe measurement of photonic quantum correlations mediated by a single phonon”. In: *Phys. Rev. Lett.* 120 (2018), p. 233601.

[132] S. Barzanjeh et al. “Optomechanics for quantum technologies”. In: *Nat. Phys.* 18 (2021), pp. 15–24.

[133] John Cenker et al. “Direct observation of two-dimensional magnons in atomically thin CRI3”. In: *Nature Physics* 17.1 (Aug. 2020), pp. 20–25. DOI: 10.1038/s41567-020-0999-1.

[134] A. C. Ferrari et al. “Raman spectrum of graphene and graphene layers”. In: *Physical Review Letters* 97.18 (Oct. 2006). DOI: 10.1103/physrevlett.97.187401.

[135] Pavana Siddhartha Kollipara, Jingang Li, and Yuebing Zheng. “Optical patterning of two-dimensional materials”. In: *Research* 2020 (Jan. 2020). DOI: 10.34133/2020/6581250.

[136] Eunpa Kim et al. “Site selective doping of ultrathin metal dichalcogenides by laser-assisted reaction”. In: *Advanced Materials* 28.2 (Nov. 2015), pp. 341–346. DOI: 10.1002/adma.201503945.

[137] Yuchao Chen et al. “Tunable nanowire patterning using standing surface acoustic waves”. In: *ACS Nano* 7.4 (Apr. 2013), pp. 3306–3314. DOI: 10.1021/nn4000034.

[138] Weiyang Li et al. “Writing magnetic patterns with surface acoustic waves”. In: *Journal of Applied Physics* 115.17 (Jan. 2014). DOI: 10.1063/1.4863170.

[139] Kanak Datta et al. “Piezoelectric modulation of Excitonic Properties in monolayer WSE2 under strong dielectric screening”. In: *ACS Nano* 15.7 (June 2021), pp. 12334–12341. DOI: 10.1021/acsnano.1c04269.

[140] Sahil D. Patel et al. "Surface acoustic wave cavity optomechanics with atomically thin WSe2". In: *PRX Quantum* 5.1 (Feb. 2024). DOI: 10.1103/prxquantum.5.010330.

[141] Jin Wang et al. "Sliding and pinning in structurally lubric 2D material interfaces". In: *Reviews of Modern Physics* 96.1 (Feb. 2024). DOI: 10.1103/revmodphys.96.011002.

[142] Enrico Perfetto, Kai Wu, and Gianluca Stefanucci. "Theory of coherent phonons coupled to excitons". In: *npj 2D Materials and Applications* 8.1 (June 2024). DOI: 10.1038/s41699-024-00474-9.

[143] Takashi Oka and Sota Kitamura. "Floquet engineering of Quantum Materials". In: *Annual Review of Condensed Matter Physics* 10.1 (Mar. 2019), pp. 387–408. DOI: 10.1146/annurev-conmatphys-031218-013423.

[144] "Reimagining computing with 2D semiconductors". In: *Nature Nanotechnology* 19.7 (July 2024), pp. 879–879. DOI: 10.1038/s41565-024-01743-w.

[145] Huan Li, Qiyu Liu, and Mo Li. "Electromechanical Brillouin scattering in integrated planar photonics". In: *APL Photonics* 4.8 (Aug. 2019). DOI: 10.1063/1.5108672.

[146] I. S. Camara et al. "Vector network analyzer measurement of the amplitude of an electrically excited surface acoustic wave and validation by X-ray diffraction". In: *Journal of Applied Physics* 121.4 (Jan. 2017). DOI: 10.1063/1.4974947.

[147] David M. Pozar. *Microwave engineering*. Wiley, 1998.

[148] R. Manenti et al. "Surface acoustic wave resonators in the quantum regime". In: *Physical Review B* 93.4 (Jan. 2016). DOI: 10.1103/physrevb.93.041411.